A Design for a High-Density Focused Ultrasound Array Addressing and Driving System

by

R. Erich Caulfield

B.S. in Physics and Mathematics,
Morehouse College, 1998

M.S. in Electrical Engineering and Computer Science
Massachusetts Institute of Technology, 2001

SUBMITTED TO THE DEPARTMENT OF ELECTRICAL ENGINEERING AND COMPUTER SCIENCE IN PARTIAL FULFILLMENT OF THE REQUIREMENTS FOR THE DEGREE OF

DOCTOR OF PHILOSOPHY IN ELECTRICAL ENGINEERING
AND COMPUTER SCIENCE
AT THE
MASSACHUSETTS INSTITUTE OF TECHNOLOGY

September 2005
[February 2006]

Signature of Author: _____
Department of Electrical Engineering and Computer Science
September 28, 2005

Certified by: _____
Kullervo Hynynen
Professor of Radiology, Harvard Medical School
Thesis Supervisor

Certified by: _____
James Roberge
Professor of Electrical Engineering
Thesis Supervisor

Accepted by: _____
Arthur C. Smith
Chairman, Committee on Graduate Students
Department of Electrical Engineering and Computer Science

A Design for a High-Density Focused Ultrasound Array Addressing and Driving System

by

R. Erich Caulfield

Submitted to the Department of Electrical Engineering and Computer Science on September 29, 2005 in partial fulfillment of the requirements for the Degree of Doctor of Philosophy in Electrical Engineering and Computer Science

Abstract

The feasibility of using focused ultrasound as an effective means of destroying malignant and benign tumors has been demonstrated in numerous studies. Research into methods for delivering the energy used in therapeutic applications has primarily used multi-element arrays, with phased array techniques offering the most flexibility. While these methods have proven effective in the ablation of tumors *in vivo*, limitations exist in several areas, which have prevented further advances from being made. In order to achieve tighter control over focal volume and increase beam steering capabilities, the number of elements used in phase array design will have to be increased. However, issues related to cost, matching, interconnects and cable assembly size have prevented high-density arrays from being realized as a practical means for treatment.

The goal of this research was to demonstrate the feasibility of designing and testing a relatively low-cost system that could effectively drive several thousand elements, while minimizing the size of the cable assembly that delivers power to the array. Use was made of flexible circuit technology as well as a novel method for addressing each channel. An investigation of a new technique for phase assignment in phased array configurations was also conducted to determine an optimal balance between the number of input lines and the quality of beam steering and focus control.

Thesis Supervisor: Kullervo Hynynen Ph.D.
Title: Professor of Radiology, Harvard Medical School, Brigham and Women's Hospital

Thesis Supervisor: James Roberge, Sc.D.
Title: Professor of Electrical Engineering, Massachusetts Institute of Technology

Acknowledgements

I would first like to thank my thesis advisor, Kullervo Hynynen, for his guidance, support, patience, and insight during my PhD research. It has been a great honor to have worked and learned under the mentorship of such an insightful, forward thinking, skilled and inspiring scientist. His consistent encouragement to reach beyond the boundaries of traditional thinking, to create new and meaningful knowledge, towards better service to humankind will, no doubt, be one of the defining influences of my time in graduate school. I would also like to thank my thesis co-advisor, James Roberge, who has been an abundant source of technical knowledge, engineering acumen, and scholarly wisdom. It has truly been a privilege to have been guided by such an accomplished teacher, thinker, and pioneer. I would also like to thank, Roger Mark, who has served on my thesis committee. His advice and encouragement has been critical in helping to navigate the doctoral program over the last two years, when careful planning and directed thought were most necessary.

I would like to thank my colleagues at the Focused Ultrasound (FUS) Laboratory at the Brigham and Women's Hospital, both past and present. The wonderfully collaborative ethos, in which everyone is always available to support one another, both professionally and personally, will be the source of many memories. I especially would like to thank Jose Juste and Sai-Chun Tang for their inexhaustible knowledge, time and help in designing and assembling my PCB's. I am also thankful for the insight, humor and kindness of Xiang-Tao (Steve) Yin, whose MATLAB code served as the foundation for much of my simulation work, and whose advice on the doctoral process has been a great help. I am grateful to Greg Clement for our many conversations on physics and his keen insights into the finer points of phased array operations. I am also indebted to Nathan McDannold for his tireless help with MATLAB and in keeping my computer operating and my data safe and accessible. I would also like to thank Danish Khatri, who has been a great source of encouragement, common sense and circuit advice. In addition, I would like to thank Susan Agabian, whose kind humor and assistance in testing and verifying a large part of my hardware has helped to make even the tedious

aspects of research enjoyable. I am also grateful to Randy King and P. Jason White for teaching me most of what I've learned about transducer design and fabrication. I am indebted to Keiko Fujiwara who never failed to acquire whatever parts or equipment I needed, in time to meet the many deadlines I faced near the end of the PhD process. I am also grateful to Sham Sokka, who first invited me to come and visit the FUS lab, and who encouraged me to think about joining. I will forever be grateful for having the chance to work with Vince Collucci, Christopher Conner, Thomas Gauthier, Manabu Kinoshita, Sonali Palchaudhuri, Scott Raymond, Elisabetta Sassaroli, Nickolai Sheikov, Christina Silcox, Karen Tam, Natalia Vykhodtseva, Yong-Zhi Zhang, and Lisa Treat, who have been wonderful colleagues and friends.

Outside of the FUS laboratory, I would like to thank Albert Chow for his advice on amplifier design and help in circuit simulation, M. Mekhail Anwar for his insights in analog circuit design, and Winston Timp for his help in designing the software interface for the HDAADS. I am also grateful to Rashid Kahn and Viki Patel at Imagineering Inc for their insights while fabricating the HDAADS, as well as Granger Scofield at Apex Microtechnology for his guidance in designing the input amplifier for the HDAADS. I am eternally grateful to the MIT Graduate Student Office and Dean Isaac Colbert for his mentorship since my arrival at MIT, and for the funding I have received during a significant part of my tenure in graduate school. I would also like to thank Marilyn Pierce and Peggy Carney in the EECS Graduate Office for their support and guidance over years. I will forever be thankful for having been apart of the MIT Graduate Student Council, Black Graduate Students Association and Tang Hall Residents' Association, which have been the cornerstone of my co-curricular education at MIT. I would also like to thank the MIT Administration and MIT Corporation for sharing with me a spectacular vision for a greater MIT.

Finally, I would like to thank my friends and family, especially my sister, Sharron, brother, Buhl, mother, Audrey, and my grandparents, Douglas and Dorthy who believed in the impossible, and who have made the improbable an inevitability. I also hold in my heart special gratitude to my nephews, Tre' and Marcus, to whom I dedicate this thesis—you have continually inspired me.

Table of Contents

List of Figures

List of Tables

1 Introduction

1.1 Background

One of the primary pillars of the medical profession is to do no harm to the patient who is seeking care. Unfortunately, due to the nature of disease, which is often manifested inside the body, the physician is many times forced to make the difficult decision to cause damage on a small scale in order to achieve a greater good for the patient's overall health. This is the basic principle underlying all surgical procedures and many drugs, as incisions and medications, by their very nature, alter the body's normal functions or structure. In the best cases, the damage caused by surgery is minimal compared with the harm done by the disease. However, in the worst cases, while curing or enabling the patient to live with her or his condition, the related complications can be severely debilitating, and greatly impact the person's quality of life.

Better treatment regimens are those that only combat the disease itself or areas of the body directly affected by the illness. There are a number of non-invasive or minimally invasive methods for destroying unwanted tissue, among them lasers, devices that transmit microwave or radiofrequency EM waves, and focused ultrasound (Adams et al. 1996;Algan et al. 2000;Amichetti et al. 1991;Arefiev et al. 1998;Arustamov, Mukhtarov, & Arustamov 2000;Bagshaw et al. 1991;Burak, Jr. et al. 2003;Cioni et al. 2001;Clement, Connor, & Hynynen 2001;Gelet et al. 2000;Goffinet et al. 1990;Hacker et al. 2004;Hoffman et al. 2002;Hynynen & McDannold 2004;Jolesz et al. 2004;Koehrman et al. 2000;Melliza & Woodall 2000;Phipps et al. 1990;Prior et al. 1991;Sato et al. 1998;Sherar et al. 2001;Viguier et al. 1993;Watanabe et al. 1995). These procedures, which offer an alternative to traditional surgery, primarily work using thermally induced tissue destruction resulting from protein denaturation or coagulation. Since these instruments can deposit energy in a highly localized manner, the effects on surrounding tissue are minimized, thus reducing ancillary damage. However, in most cases, there are limitations that have prevented them from gaining greater use as substitutes for surgical treatment.

Lasers, because they are, in essence, light sources can only be used topically, as energy is absorbed directly at the surface of the skin. Even when attached to a probe, they still require an incision or other opening to be used internally. Thus, their utility in treating areas inside of the body is limited. Microwave or RF devices also offer an option for non-invasive treatment. While they are able to deliver energy into soft tissue, they too are limited to volumes near the skin's surface. One method which offers greater promise for non-invasively treating deeper tissue volumes without damage to surrounding areas is focused ultrasound (FUS).

1.2 Focused Ultrasound (FUS) Surgery

The use of ultrasound (0.5 to 10MHz) for therapeutic applications has been studied extensively over the last several decades, for a number of uses including tumor destruction (Chen et al. 1993;Chen et al. 1999;Prat et al. 1995;Rowland et al. 1997;Sibille et al. 1993;ter Haar et al. 1991;Vaezy et al. 2000;Yang et al. 1992;Yang et al. 1991;Yang et al. 1993), drug delivery (Unger et al. 1998), gene therapy (Greenleaf et al. 1998;Kim et al. 1996;Madio et al. 1998;Miller et al. 1999;Unger, McCreery, & Sweitzer 1997), thrombolysis (Francis & Suchkova 2001;Porter et al. 1996), damage via cavitation (Miller et al. 2000;Prat et al. 1994;Vykhodtseva, Hynynen, & Damianou 1994), blood vessel occlusion (Delon-Martin et al. 1995;Hynynen et al. 1996b;Rivens et al. 1999), and selective opening of the blood brain barrier (Hynynen et al. 2001a;Vykhodtseva, Hynynen, & Damianou 1994). As early as 1927, ultrasound has been investigated as a treatment option for cancer and other diseases (Nakahara & Kabayashi 1934;Szent-Gorgyi 1933;Wood & Loomis 1927). Research has shown that ultrasound can be used to treat a number of different areas of the body including: the eye (Coleman et al. 1985), prostate (Bihrle et al. 1994;Chapelon et al. 1999;Foster et al. 1993;Gelet et al. 1999;Madersbacher et al. 1993;Madersbacher et al. 1995;Mulligan et al. 1998;Nakamura et al. 1997;Saleh & Smith 2005;Sanghvi et al. 1996;Vallancien et al. 1992), liver (ter Haar et al. 1998;Vallancien, Harouni, Veillon, Mombet, Prapotnich, Bisset, & Bougaran 1992), kidney (ter Haar, Rivens, Moskovic, Huddart, & Visioli 1998;Vallancien, Harouni, Veillon, Mombet, Prapotnich, Bisset, & Bougaran 1992), bladder (Vallancien et al. 1996;Watkin et al. 1996), and breast (Hynynen et al. 2001b). FUS as a course of

treatment affords the same benefits as traditional surgery, in that it provides an effective method for neutralizing the effects of unwanted tissue. For some difficult to reach parts of the body, ultrasound can be delivered via interstitial probes (Diederich et al. 1996;Hynynen & Davis 1993;Lafon et al. 1998), intravasular catheters (Hynynen et al. 1997;Zimmer et al. 1995), and intracavitary applicators (Foster, Bihrle, Sanghvi, Fry, & Donohue 1993;Hutchinson & Hynynen 1996;Sokka & Hynynen 2000). However, because FUS can be completely non-invasive technique, it lacks many of the drawbacks associated with common surgical procedures. For example, FUS offers treatment without bleeding or external scarring, and as a result, a decrease in recovery time and risk of infection (Hynynen 1996). Avoiding many of the complications of surgery, FUS has potential as cheaper and safer method for fighting tumors and others illnesses not currently treatable by other techniques.

While ultrasound has shown promise as an effective method for inducing cell death in pathological tissue for more than half century, for a long time its use had been limited by insufficient means for monitoring and evaluating its effects. A number of modalities have been considered for observing bio effects, among them X-rays and other imaging schemes that use ionizing radiation (Fallone, Moran, & Podgorsak 1982;Gelet, Chapelon, Bouvier, Rouviere, Lasne, Lyonnet, & Dubernard 2000;Jenne et al. 1997). However, these systems are constrained by the long-term harm that could be done to the patient. Another method is the use of thermocouples for measuring temperature elevation (Clarke & ter Haar 1997;Duck & Starritt 1994;Fried et al. 2002;Goss, Cobb, & Frizzell 1977;Lele & Parker 1982). However, this process requires implanting the devices inside of the patient, which negates many of the benefits of non-invasive treatment. The use of diagnostic ultrasound for monitoring has also been investigated (Fry 1968;Madersbacher, Pedevilla, Vingers, Susani, & Marberger 1995;Sanghvi et al. 1999;Sheljaskov et al. 1997), but its utility is restricted to soft tissue, as ultrasonic waves are obstructed by air and bone (ultrasound for therapeutic applications also suffers from this limitation, though in a less severe way, since we are only interested in how the waves travel in one direction). The imaging modality enables the effective monitoring of temperature, and has helped facilitate the rapid progress of FUS as a viable treatment option is Magnetic

Resonance Imaging (Chung et al. 1996;Cline et al. 1995;Hazle et al. 2002;Hynynen et al. 1993;Hynynen et al. 1996c;Ishihara et al. 1992;McDannold et al. 1998;Stepanow et al. 1995). Because MRI is a non-ionizing process, it can be used repeatedly without long-term harm to the patient or technician. Moreover, its ability to image a variety of different tissue types has enabled it to be used in numerous areas inside the body. With this repeatability and flexibility, MRI has helped facilitate the evolution of FUS into the most promising non-invasive alternative to traditional surgery.

The basic principles underlying FUS involve concentrating high frequency sound waves inside the body at a designated location, called the focus, while minimizing pressure levels elsewhere. At therapeutic frequencies, waves can be made to constructively interfere at a specific location, thereby delivering a considerable amount of energy to that position. Because there is mostly destructive interference at locations outside of the focus volume, little energy is deposited there. This can be done effectively because sound has a relatively low absorption rate in soft tissue, thus enabling increased delivery only at the desired places. For example, an ultrasound wave at 1.0 MHz has a wavelength of only 1.5mm, but has a penetration depth close to 100mm (Hynynen & Lulu 1990). As a result, the possibility exists for resolution on the order of several millimeters and a treatment depth of tens of millimeters or more inside of the patient. The result is a method that can be used to safely and precisely destroy unwanted tissue without damage to healthy adjacent areas.

Investigations have centered around two major mechanisms for ablating pathological tissue using ultrasound: temperature elevation and cavitation. In the thermal regime, which is the more commonly used of the two methods, sound energy is converted directly into heat as the waves are absorbed by the tissue. This process is well-modeled and lends itself to monitoring using MRI (Damianou, Hynynen, & Xiaobing 1995;Hill et al. 1994;Lizzi & Ostromogilsky 1987) Using this method, temperature elevations of 20-30^{o} C above ambient body temperature can easily be generated (Daum & Hynynen 1999). In the event of sufficiently high acoustic pressures, small gas bubbles can sometimes form. This process is called cavitation, and can lead to local temperature increases of

2000° K or more, as bubbles expand and violently collapse releasing tremendous amounts of energy (Apfel 1982). While cavitation has also been extensively studied, the exact location of bubble formation cannot be predicted as accurately.

1.3 The Current State of the Art

In both the thermal and cavitation regimes, two basic arrangements have been used for sonication: single-element (transducer) configurations and multi-element array designs. Single element systems offer a simple option for exploring ultrasonic effects on tissue, while multi-element arrays provide a more flexible alternative for diagnostic and therapeutic applications. Single-element devices are fashioned from a solid piece of PZT (Lead-Zirconate Titanate) or some other piezoelectric or piezocomposite material, which reversibly deforms when a voltage is applied across it. By applying a periodic voltage to a block or plate of the material while it is submerged in a liquid, sound waves are generated, which can then be used for diagnostic or therapeutic purposes. To achieve the focusing needed for treatment, the transducer itself will often be constructed so that it is curved. Based on the geometry of the element, a point in space is created where most of the waves will constructively interfere once the device is active. In many cases the focus is much smaller than the area being treated.

Because the focus is relatively tiny, in order to provide utility during treatment, it would need to be moved. However, with single phase systems the only way to move the focus is to move the transducer itself, which would require using a positioning system, which may not be possible due to the transducer's location, e.g. inside of an MRI magnet. As such, in order effectively treat larger volumes a method for easily steering the focus needed to be developed.

During the last twenty years, devices called phase array transducers have become more prominent, as they provide electronic beam steering capabilities, as well as enabling compensation for a number of factors which distort the ultrasound field (Benkeser et al. 1987;Buchanan & Hynynen 1994;Cain & Umemura 1986;Clement & Hynynen 2000;Daum & Hynynen 1999b;Diederich & Hynynen 1989;Do-Huu & Hartemann

1981;Ebbini et al. 1988;Fan & Hynynen 1995;Fjield & Hynynen 1997;Frizzell et al. 1985;Hutchinson & Hynynen 1998;Hynynen et al. 1996a;Hynynen & Jolesz 1998;Ibbini, Ebbini, & Cain 1987;Maslak 1975;McGough et al. 1994;Sokka & Hynynen 2000;Sun & Hynynen 1998). Phased array systems are multi-element configurations that vary the phases of each individual element in order to create the focus. These transducer arrays need not be of any particular geometry to be effective, as adjustment to the phase can be made to achieve various focal locations. Phased arrays also provide the ability to create multiple foci at once, whose position(s) can be moved almost instantaneously by simply varying the input signal. This feature is especially important because being able to create multiple foci has the potential of improving heating distribution (Ebbini & Cain 1989). Currently, most FUS phased array systems are 1-dimensional and employ from 5 to 200 elements, with a few 2-dimensional systems using several hundred elements (Daum & Hynynen 1999a).

1.4 Limiting Factors for High Density FUS Arrays

In order to develop systems that exhibit greater focus control, the number of elements will need to be increased. This fact results from the relationship between focal precision, beam steering, and inter-element spacing. Figure 1-1 shows a 2-element array with frequency f and inter-element spacing of ~ 4λ. For this simple case, the waves from the two elements are in phase at the focus. However, there are numerous other places where the waves constructively interfere (called grating lobes), which present a problem for clinical uses, where significant constructive interference is to be minimized outside of the focal volume. In this example, there are only two waves that intersect at the focus. This is the same number that intersect in other places in the field. For arrays with more elements, there would be many more waves merging at the focus than at any other place in field, making it possible to deposit a large amount of energy there while imparting little elsewhere.

If the elements were to be moved farther apart the number of constructive interference points would increase. The number would also increase if the focus were to

be moved away from the center axis. In order to reduce the creation of grating lobes, the two elements would have to be moved closer together. Figure 1-2 shows a similar 2-element array, but with an inter-element spacing of $\lambda/2$. In this configuration, there is a significant reduction in the number of constructive interference points, yielding a more cleanly defined focal region. Because there are only two elements in this illustration, there is a line of interference points along the center axis between the two elements. However, if more elements were added with the same spacing, this region would become less prominent as the pressure at the focus would dramatically increase relative to other locations in the field. It is this relative difference in pressure values that creates a useful focus, since extra-focal regions are heated much less, by the resulting lower pressures.

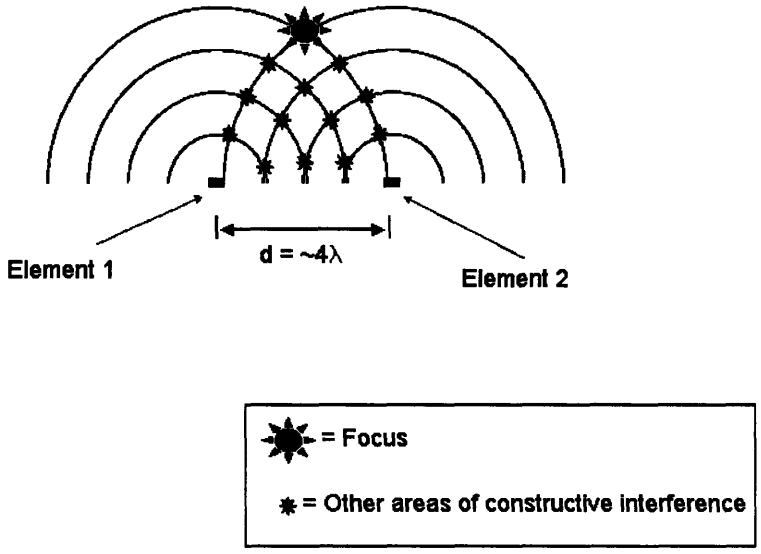

Figure 1.1 A diagram of a 2-element array with frequency f, wavelength λ and inter-element spacing of $d = \sim 4\lambda$.

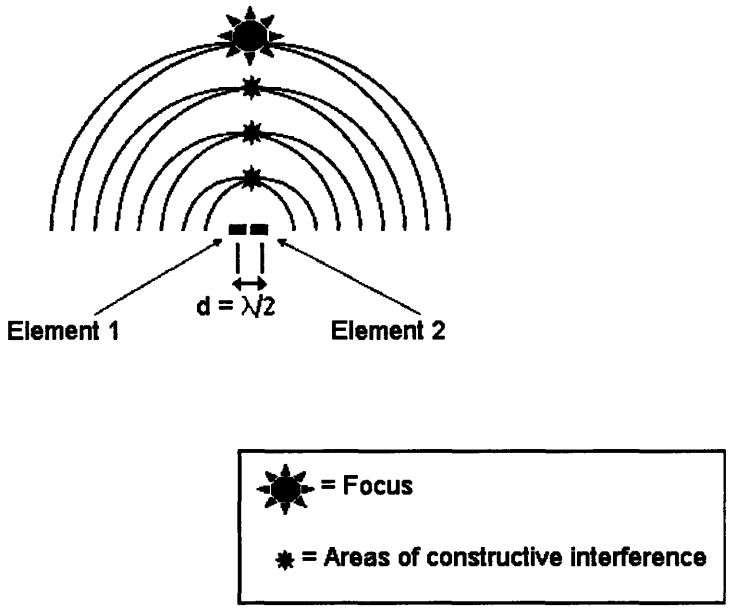

Figure 1.2 A diagram of a 2-element array with frequency f and wavelength λ and inter-element spacing of d = λ/2.

As a result of the reduction in the number of grating lobes, the <λ/2 spaced arrangement provides the optimum spacing for beam steering. From Figure 1-2 it can be seen that moving the focus to other locations using this inter-element distance, the possibility for creating additional constructive interference points is minimized. It might appear at first that moving the elements closer than λ/2 could yield even better results. However, decreasing the spacing further would have no additional benefit as there would be no increase in focal intensity, i.e. all of the waves are already in phase at the focus, and as such, no additional pressure increases could be accomplished. In addition, from Figure 1-2 it can be seen that a further reduction in grating lobes would not result since the minimum number has already been achieved.

Having shown the advantages of moving to λ/2 spacing, now consider a typical therapeutic frequency of 1.1 MHz, λ = v/f = (1500m/s)/(1.1MHz) = 1.36mm and λ/2 = 0.68mm, where v is the speed of sound in water and f is the frequency of the signal. With

this spacing, the individual elements would have to be relatively tiny, and in order to cover a large enough area to deliver an appreciable amount of power, there would have to be a large number of them. As such, one of the key components to increasing the capabilities of FUS systems is the ability to design and drive arrays with a large number of small elements. However, there are a number of issues that have prevented higher density arrays from being implemented in a practical manner.

One constraint is the problem of cost. Currently, many driving systems for FUS arrays rely on high Q transducers and accompanying resonant amplifiers. These high power systems are needed because a smaller number of elements requires that each individual transducer supply a significant amount of power in order for the array as whole to be useful. Because many of these configurations rely on finely tuned resonant circuits, the components needed to construct them tend to be expensive and sometimes difficult to replace. In addition, the driving circuitry has to be manually matched to the transducer load for each channel, which can often be a very time-intensive process. Another issue is that, for a given application, as the number of elements increases, the size of each element tends to decrease. As a result, it becomes increasingly difficult to form connections (interconnects) to each one. The last major limitation is the size constraints of the cabling that delivers power to the array. As the number of elements increases, the bulk of the wires going to the assembly becomes excessively large. This is especially of concern when the device is to be used inside the body.

If more effective means of developing high-density FUS systems are to be developed in the future, the issues of cost, matching, interconnects and cabling/complexity will have to addressed.

1.5 Specific Aims

This research examines a method for effectively driving an array of thousands of elements for use in therapeutic ultrasound. The first section of the study is an examination of the theory behind a novel phase assignment scheme, which allows a large

number of elements to be driven while using relatively few input lines. The second section assesses a small-scale implementation of the phase allocation process, which addresses the cost, matching, and cable assembly issues.

1.5.1 Phase Assignment Protocol

Perhaps the greatest challenge to achieving higher density phase arrays lies in the constraints of the cable assembly that delivers power to the array. Traditional designs have used a one-to-one correspondence between the driving signal wire and its corresponding element in the element in the array. Figure 1-3 illustrates the basic functioning of a phased array with five elements:

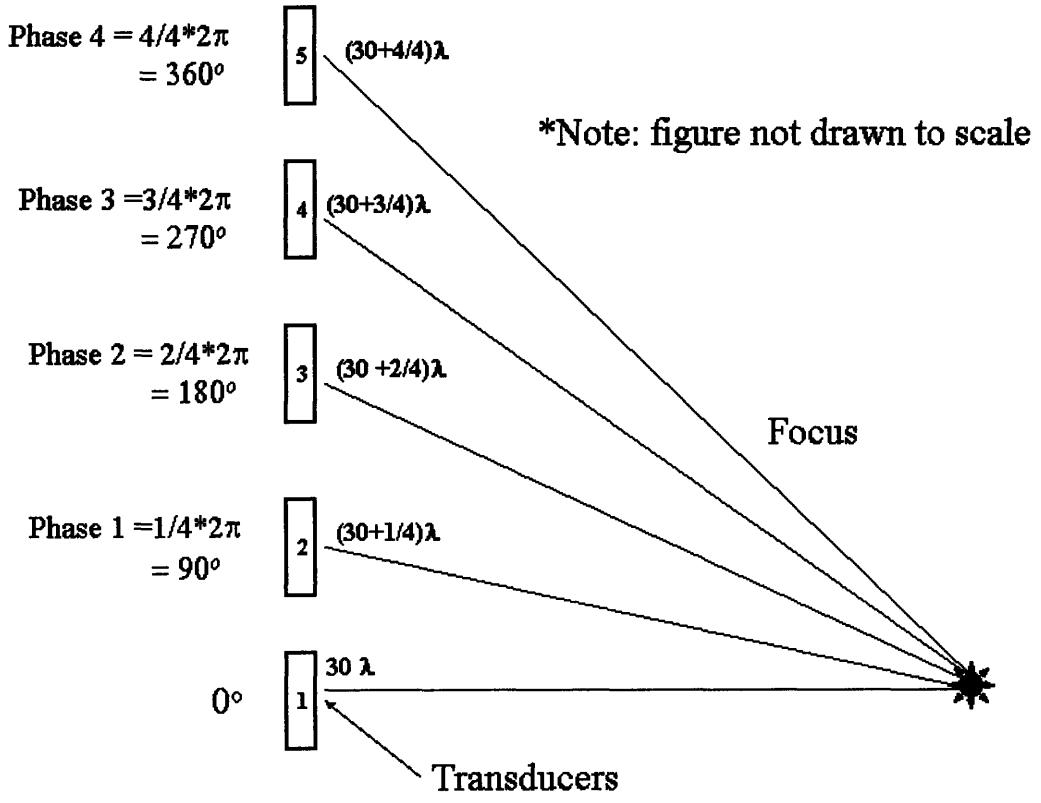

Figure 1.3 A diagram of a phased array with phase assignments

Assuming that all of the transducers use the same frequency, in this case transducer 1 serves as the 0° phase reference for the others, meaning no adjustment is needed for it. Since the distance from transducer 2 is different from transducer 1, its phase has to be

shifted in order for it to constructively interfere with transducer 1's wave at the focus. The adjustment is based on the simple geometry of the triangle formed between the two elements and the focus. Here, the difference is $\lambda/4$, which when converted to a delay for a sinusoid, becomes $(2\pi/\lambda)*\lambda/4 = \pi/2$ radians or 90^{o}. In a similar fashion, the phase of transducer 3 can be adjusted so that it is in phase with the others at the focus. This same process is performed for each of the transducers in the array. To move the focus, one only need follow the same method described, adjusting the phases of each element accordingly. This technique also allows for the creation of multiple foci by using combinations of elements.

It should be noted that as the number of elements grows, so does the number of phase assignments and wires. The problem is further compounded by the need to shield the wires to minimize electrical interference. This is usually done by making use of coaxial wires, whose price has been found to scale inversely with the size of the wire. Because high-density arrays will require very small wires, which may not be obtainable, their cost and availability prohibit use in large numbers. Thus, it would be very difficult, using existing methods, to design practical arrays that could have four or five thousand elements.

The solution which this study examines is to quantize the phases available at the input of array. A variation of this concept was explored by Fjield et al in 1999 in the context of low-profile lens and showed promise for use in other areas (Fjield, Silcox, & Hynynen 1999). The central idea is that instead of allowing practically infinite phase resolution for creating the focus, only a relatively small number of phases will be used. All of the phases that lie within a specified window are assigned to a single phase at the center of the range. For example an element whose required phase falls between 45^{o} to 135^{o} would be assigned a phase of 90^{o}. Done this way, the need for each individual element to have its own phase and unique wire to deliver it is eliminated. By having each element share input lines with others requiring similar phases there is a tremendous reduction in the number of discrete wires coming into the system. For example, an array with 10000 elements, and only 4 different phase increments: 90^{o}, 180^{o}, 270^{o}, and 360^{o},

could be managed by only 34 lines (4 input signal lines and 30 control lines). It should be noted that the number of input wires required does not increase as additional elements are added, thus amplifying the benefit as the number of channels grows.

MATLAB simulations, making use of the Rayleigh-Sommerfeld sum and Huygens Principle (where individual elements are treated as being made of smaller simple sources whose contributions are summed to give the field for that particular element) were developed in our laboratory, which describe focused ultrasound propagation in a homogeneous medium. The program can be varied along one or more parameters, including: the number of elements, their center-to-center spacing, the wavelength of the sound and propagation medium. Beam steering capabilities for arrays ranging in size from 64x64 to 128x128 elements were examined, with foci located from 20 to 60mm from the array surface, and from 0 to 30mm from the center of the plane parallel to the array. The frequency used in the simulations was 1.1MHz and the medium was water. A number of metrics were used to describe the quality of the focus, including: 3dB length and volume, side lobe to main lobe ratio, and peak intensity.

1.5.2 Phase Assignment and Addressing Implementation

The development of large scale, high-density focused ultrasound driving systems has been primarily hampered by cost and a lack of technology capable of rendering them feasible. Traditional driving systems have relied on high Q ceramic transducers and tuned amplifiers to deliver ultrasound. However, these systems are expensive and require a significant investment in time to make them operational. In conjunction with recent advances in transducer technology and in response to the constraints imposed by traditional systems, our laboratory has conducted research into improving how ultrasound is created and controlled.

One area where progress has been made is in developing relatively new broadband piezocomposite materials, which have allowed us to operate over a wide range of frequencies. Our laboratory has developed a system that can deliver 1-2 W of electrical power per channel, is broadband from DC-10MHz and scalable from 50 to

2000+ channels (Sokka 2003). This configuration significantly improves the ability to effectively delivery ultrasound and solves many of the problems associated with resonant transducers and their accompanying amplifiers. However, while this configuration does offer the ability to effectively drive a relatively large number of channels, it remains limited by its one element to one driving wire power delivery scheme. This restriction makes it somewhat difficult to make full use the system's scaling capabilities.

In order to overcome the limitations of current designs and also to verify simulation results, a 128 channel addressing and driving printed circuit board (PCB) was designed, built, and evaluated. The board provides 0.5 to 1.7 W of electrical power per channel, is broadband from DC to 5 MHz and is scalable from 128 to 10000 or more channels. This design requires only 24 input lines for its 128 channels and has a channel per unit area 2.5 times that of the previous broadband system. The board was used to drive a 128-element piezocomposite transducer array that was developed in our laboratory. The PCB was connected to the array via a novel flexible circuited designed to mate with connecting pad on the back of the transducer case. The pressure field was measured in water, while operating at 1.1 MHz. Experimental results were compared to simulations to access functionality. The system offers one implementation of the quantized phase concept, and provides proof that a relatively low-cost high-density array driving circuit could be fabricated using existing technology.

2 Phased Array Model and Simulations

2.1 Introduction

In this chapter we examine the focal quality and beam steering capability of planar phased arrays. There are a number of issues related to phased arrays that require methods for mitigating their effects, among them the appearance of grating lobes (de Jong et al. 1985) and other unwanted areas of constructive interference, which occur near the transducer surface. To assess the benefits and limitations of using this configuration for treatment applications, a computer model was developed, that would provide insight into the impact of various physical parameters on the ultrasonic field. Among the factors considered were array size and power distribution. It was discovered that for larger aperture arrays, when the focus was placed near the transducer surface, apodization of the element power was required to offset undesired pressure increases between the focus and array. The relative effectiveness of this weighing technique for reducing the prominence of these unwanted areas was investigated. The aim of the section is to lay a foundation upon which further work can be done towards practical implementation of high-density array systems.

2.2 Material and Methods

2.2.1. Numerical Simulations

2.2.1.1. Simulation Parameters

The pressure fields were simulated using the Rayleigh-Sommerfeld sum:

$$p(x,y,z) = \sum_{i=1}^{n} \sqrt{\frac{2P\rho}{cA}} \left(\frac{fS}{d_i}\right) \exp\left[j(\phi_i - \frac{2\pi d_i}{\lambda}) - d_i\alpha \right] \qquad (2.1)$$

Here p = pressure (Pa), P = total acoustic output power of the array (W), ρ = density of the medium (kg m^{-3}), c = speed of sound in the medium (m/s), A= total surface area of the array (m^2), f = resonant frequency of the array (frequency at which the array has its largest output for a given input signal), S = area of corresponding element (m^2), α = the attenuation coefficient (Np/m/MHz), d = distance from the field point to the

corresponding element (m), ϕ = the phase of the source, and i = the corresponding element index,. For this study each element was modeled as being composed of 9 simple sources that all used the same phase. The resulting pressure field was found by using Huygen's Principle, which states that the field at a given point is the superposition of the contributions from all of the active elements, in this case, simple sources in an array. Simulations were run for a 128x128, 1.1 MHz, array with 0.44mm x 0.44mm elements having center-to-center diagonal spacings of 0.64mm and x and y spacings of 0.45mm. It should be noted that the $\lambda/2$ is equal to 0.68mm, and that the diagonal distance was constrained by this value, since it is the farthest distance between adjacent elements, and guarantees that elements along all dimensions satisfy the $\lambda/2$ requirement. The medium was assumed to be water, where the speed of sound, c = 1500m/s, the density, ρ = 1000kg/m^3 and the attenuation coefficients, $\alpha = 2.88 \times 10^{-4}$ Np/m/MHz (Duck 1990). The total output power of the array was 1W. The transducer orientation can be seen in Figure 2.1:

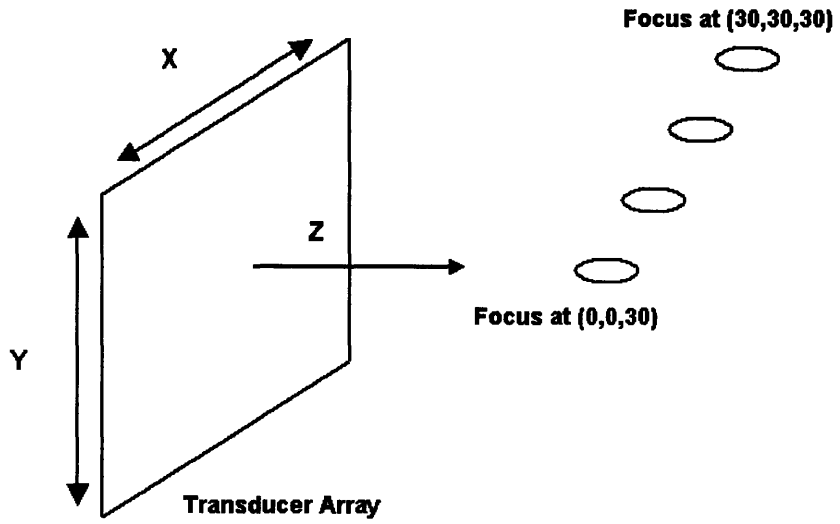

Figure 2.1 Transducer Array Coordinate System

2.2.1.2. Focus metrics

For all simulations the transducer array was located in the plane Z = 0mm, with its center at the origin, and sound propagating the positive Z direction. The resolution in the calculated pressure field in the x, y, and z directions was 0.22 mm, yielding a volume resolution of 1.1×10^{-2} mm^3. This was chosen to give sufficient information about the field structure, while minimizing the simulation time. For each case, the focus was electronically steered to multiple locations to determine the effect on peak focal intensity, the ratio of side lobe to main lobe, the 3dB length, x and y width and volume, and the overall intensity field. The side lobe ratio and 3dB length and widths were measured by visual inspections of the associated graphs and the peak pressure squared and 3dB volume were calculated by the program. The focus location ranged from X = -30mm to +30,Y = -30mm to +30 and Z=0mm to 100mm. Unless otherwise noted, when the focus was steered to a position away from the origin of given Z-plane, it is done so in X=Y increments of 10mm, e.g. for the plane Z=30 the focus would be steered to (0,0,30), (10,10,30), (20,20,30) and (30,30,30). This method was chosen as it reveals the effects of the asymmetry of the square planar array. The upper bound of 30mm for x and y was selected because it is approximately equal to 28.8mm, which is the distance from the center to the side edge of the array, and consequently of the converging region of the field. All simulations were written using MATLAB and were run using a PC with an Athlon XP 2800 processor.

2.2.1.3. Array Size

To investigate the effects of array size on focal control, the dimensions of the 2D array were varied. In each scenario described in section 2.2.1.2, the array size was increased from 32x32 to 128x128 elements with simultaneous x and y steps of 16 elements (an aperture increase of 7.2mm). The impact was measured using the same metrics examined in section 2.2.1.2. In this case the focus was steered in the plane Z=30mm at (0,0,30) and (10,10,30). These locations were chosen as they represent a useful sonication depth, and lie with the array field (edge of the array) of most sizes considered.

2.2.2 *Foci Near the Transducer Array Surface*

One of the features of planar phased arrays is the appearance of a continuous pressure "ridge" leading from the focus to the surface of the transducer, when the focus is brought close to the array. This phenomenon does not occur with spherical transducers and results from the fact that, in terms of area, planar transducers do not map directly to their curved counterparts. Recall that in traditional non phased array transducers the focus is geometrically created by constructing the transducer in such a way that all points on the surface are equidistant from the desired focal location. As such, when the array is excited, all of the resulting waves are all in phase at the focus. Planar phased arrays attempt to mimic this kind of behavior by adjusting the phases of each element so that the waves constructively interfere at the focus. This is a reasonable approximation for foci that are relatively far from the array, since for distant foci the required radius of curvature compels the array to be relatively shallow. However, the approximation breaks down nearer to the surface. Examination of figure 2.2 shows why this is the case.

In figure 2.2A, the focus is located far from the array. As such, the curved transducer and the planar transducer have approximately the same active surface area.. Of more importance is the fact that the region on the outside ring or edge of the spherical array and the elements in the outer portion of the planar array, occupy and area of similar size. However, when the focus is moved closer, as in Figure 2.2B, the difference between then two areas becomes significant. Consequently, the outer elements in the planar array will contribute much more to the focus than the corresponding section of the curved transducer. Since the waves from the elements will be converging such that their normal vectors are almost parallel. What results is large area where constructive interference will occur, thus producing the "ridge".

In order to mitigate the impact of this effect, the contribution of the outer elements has to be reduced. This is done by simply reducing the power to those elements. Since the effect is primarily distance related, the scaling should be proportional to the distance from a given element to the focus. However, recall from the Rayleigh-Sommerfeld sum:

$$p(x,y,z) = \sum_{i=1}^{n} \sqrt{\frac{2P\rho}{cA}} \left(\frac{fS}{d_i}\right) \exp\left[j(\phi_i - \frac{2\pi d_i}{\lambda}) - d_i\alpha \right] \qquad (2.1)$$

that the pressure is also exponentially related to distance via α, the attenuation coefficient. As such the adjustment should also reflect this factor. The resulting scaling coefficient thus becomes

$$K = \left(\frac{1}{d_i}\right) \exp\left[\frac{1}{d_i}\alpha\right] \qquad (2.2)$$

Where d, i and α have the same meaning presented in equation 2.1.

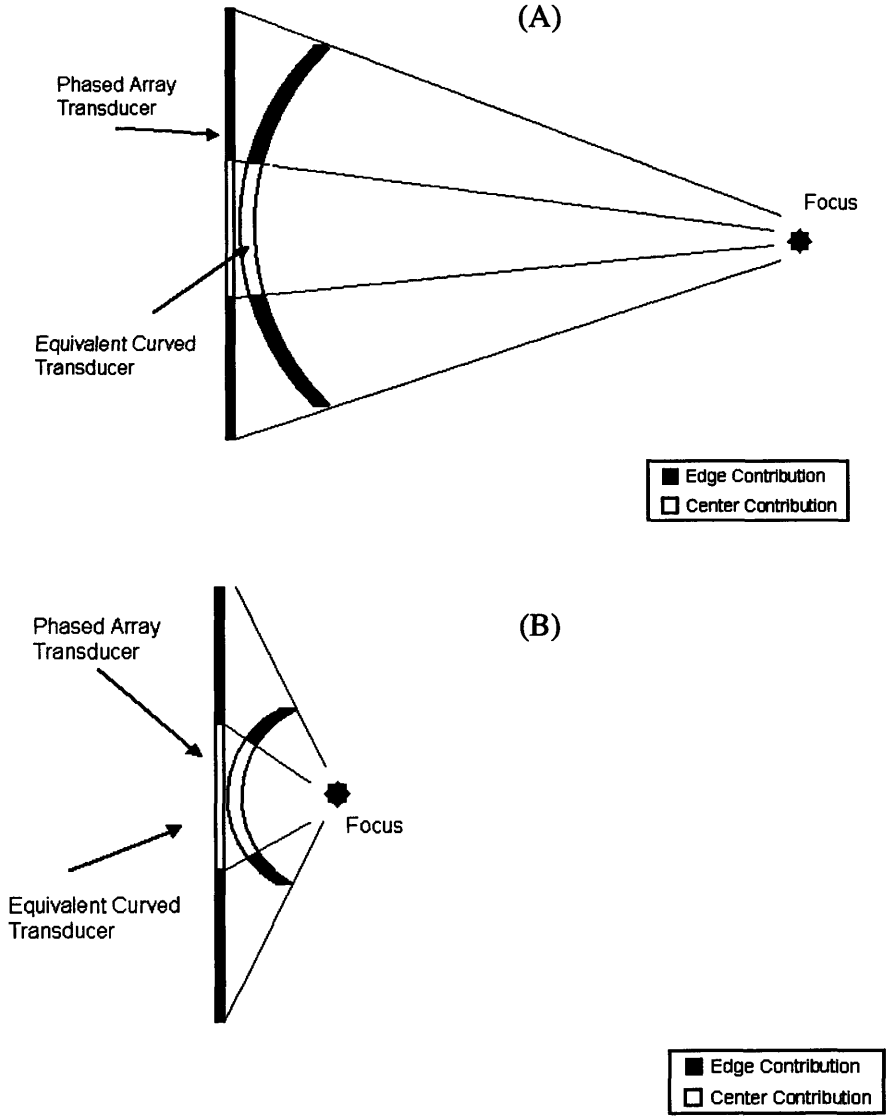

Figure 2.2 A diagram of the element contribution to the focus for a linear 128 element array and a spherical single phase transducer that would create the same focus. (A) Case where the focus is far from the array (B) Case where the focus is near the array

This amplitude adjustment, or apodization, is shown for a linear 128-element array with focus at (0,0,10)mm in Figure 2.3.

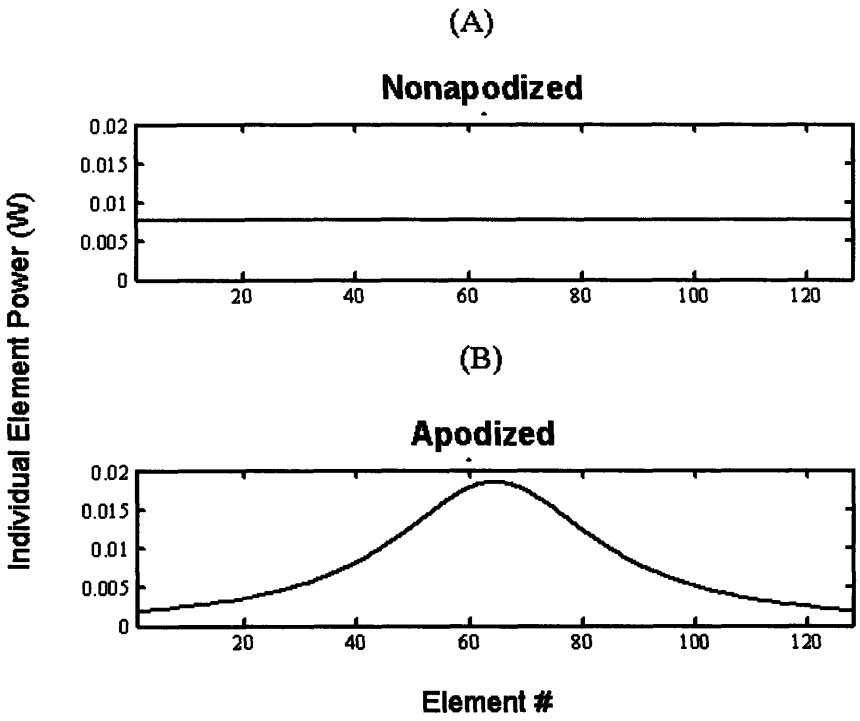

Figure 2.3 Power apodization summary for a linear 128-element array with focus at (0,0,10) (A) Nonapodized, equal power case (B) 1/d exp(αd) apodization case

While this technique has been used in diagnostic applications for increased control over grating lobes (Eaton, Melen, & Meindl 1980;Karrer et al. 1980b), it has not seen use for very near field therapeutic applications. By enabling the focus to be brought closer to the transducer surface, the flexibility of phase array technology is further enhanced.

2.3 Results

2.3.1 Off Axis Distance Results

Figure 2.4 shows the pressure squared field along the central axis (0,0,Z). for a 128x128 element array.

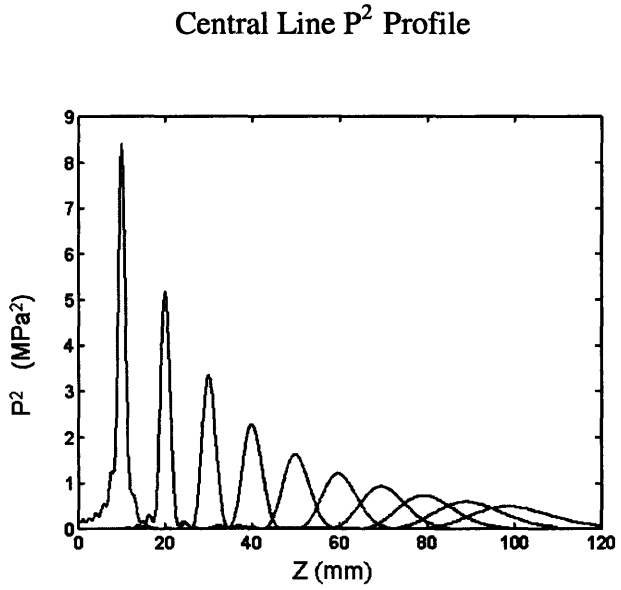

Figure 2.4 A graph of the P^2 distribution along the central axis (0,0,Z) for foci from Z=10mm to 100mm in 10mm increments, for a 128x128 element array.

Note that the peak p^2 for each focus appears to decay exponentially at the focus moves away from the transducer. Also, observe that the beam length increases substantially as the focus is steered Figures 2.5-2.7 show the pressure field squared for foci at locations from Z=30mm to Z=100mm, both at the origin and extremes (30,30,Z) of each plane.

(A)

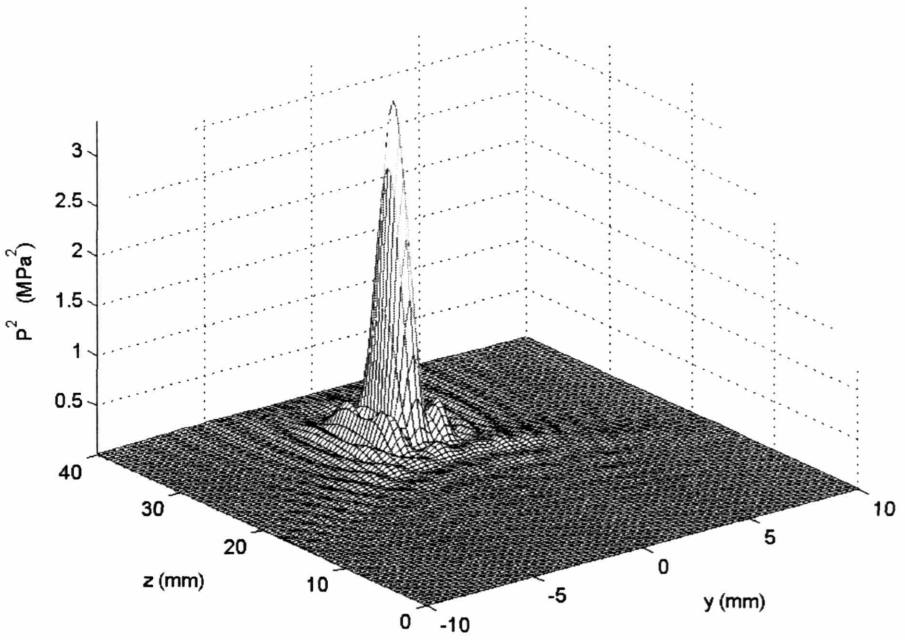

(B)

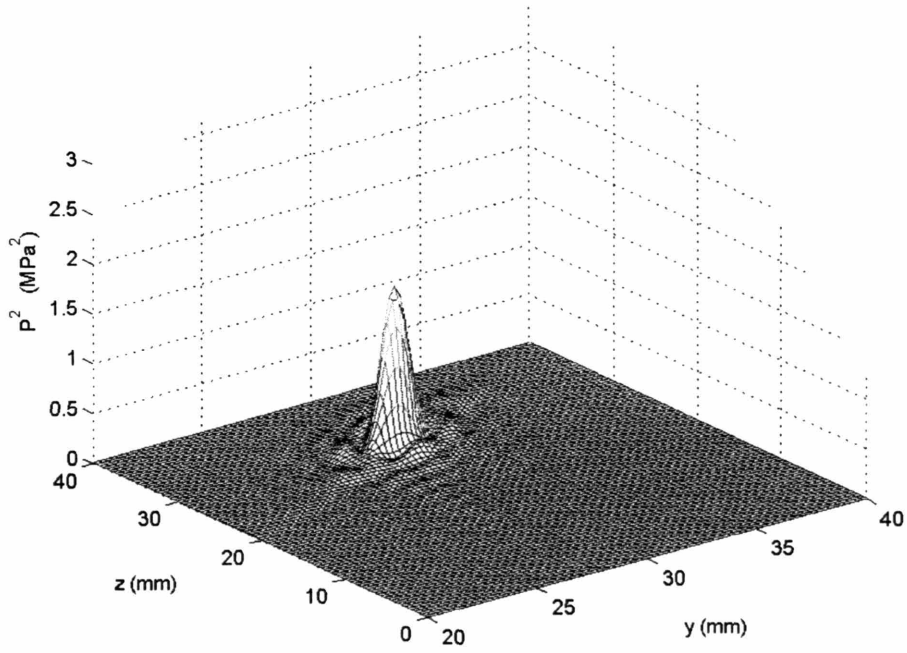

Figure 2.5 A diagram of the pressure field squared for a 128x128 element array (A) Focus at (0,0,30) (B) Focus at (30,30,30)

(A)

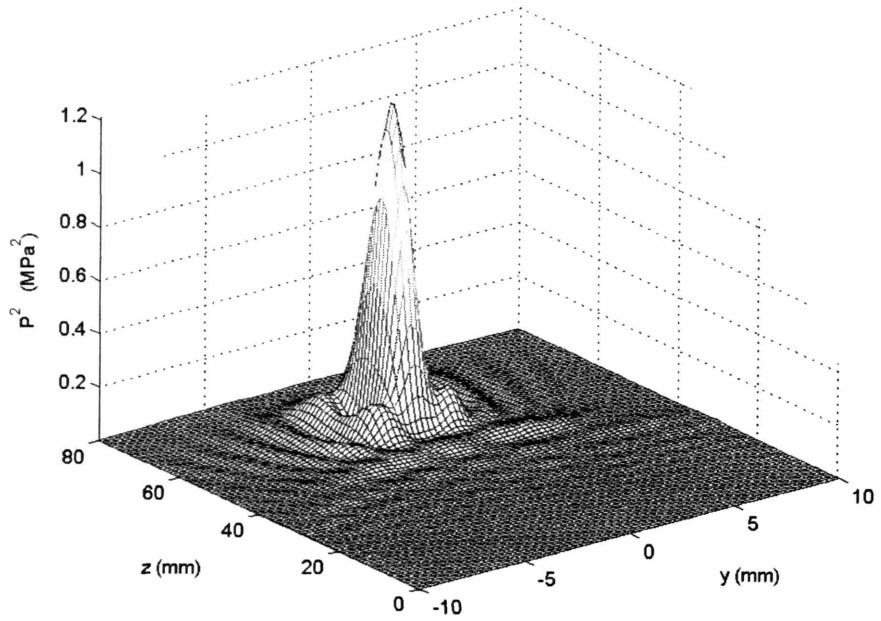

(B)

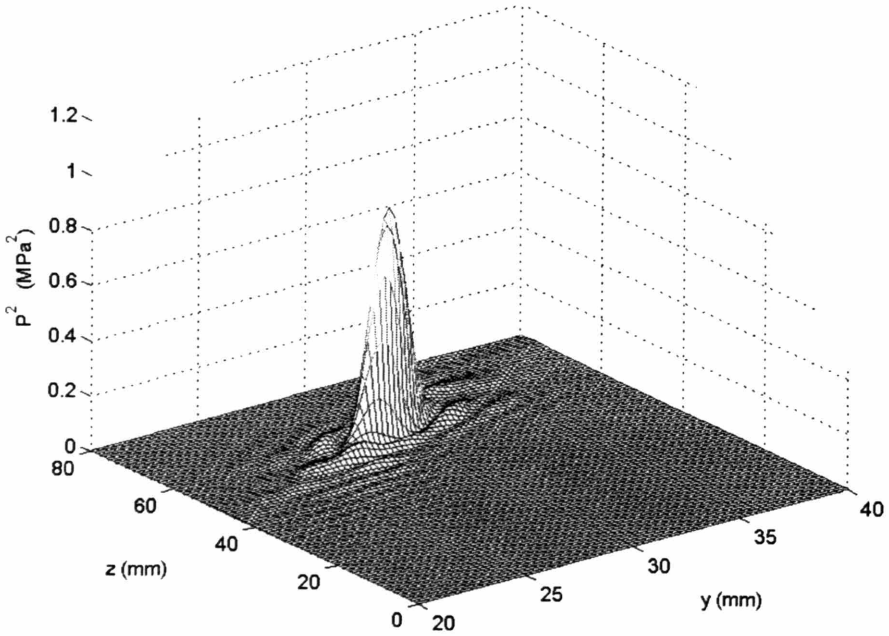

Figure 2.6 A diagram of the pressure field squared for a 128x128 element array (A) Focus at (0,0,60) (B) Focus at (30,30,60)

(A)

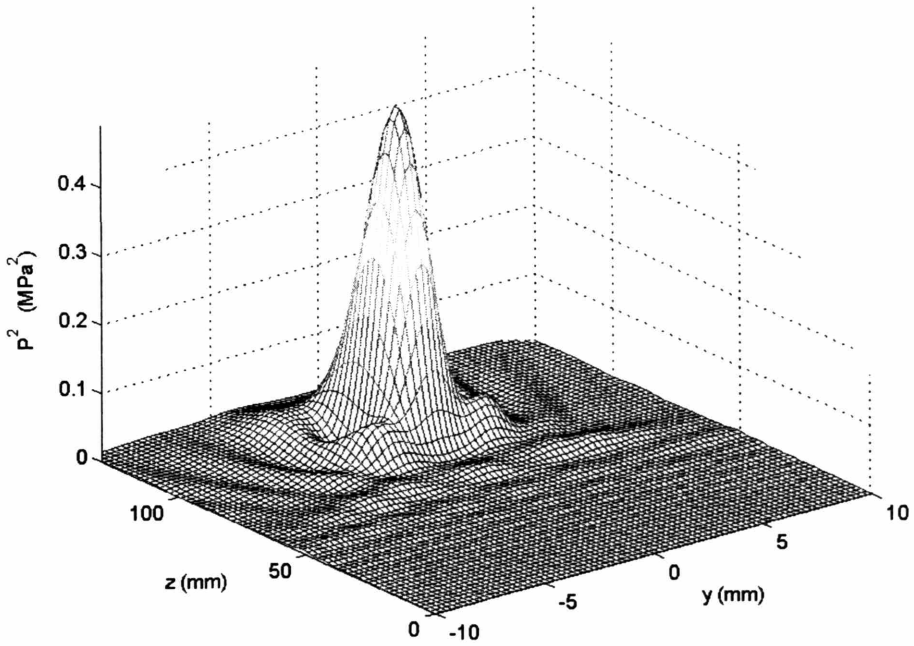

(B)

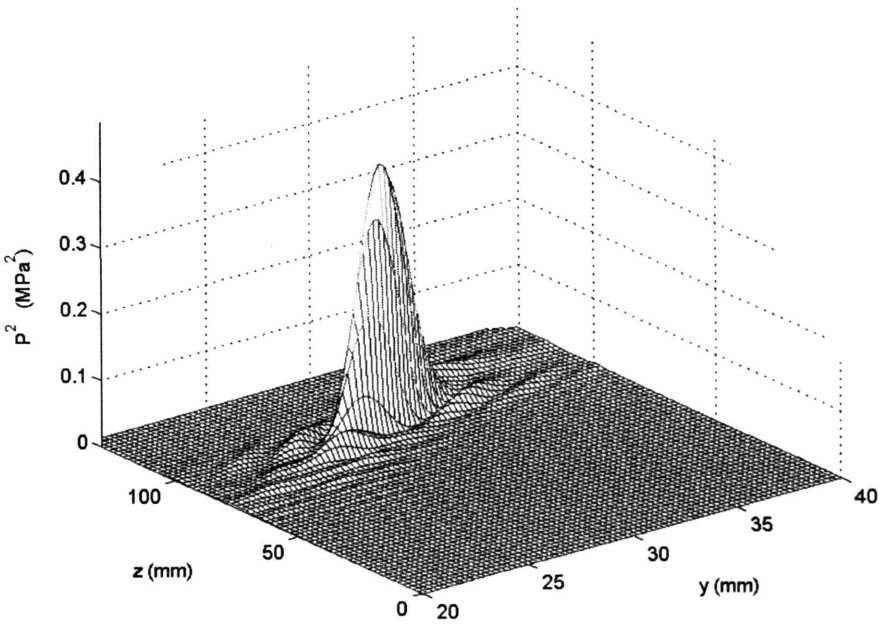

Figure 2.7 A diagram of the pressure field squared (A) Focus at (0,0,100) (B) Focus at (30,30,100)

Note that in each case the grating lobes are suppressed in the field near the transducer plane at z = 0mm.

Measurements of 3dB beam length, width and volume as well as the peak pressure squared were done as a function of the x = y = n distance from the center of the plane being considered (where n=0,10,20, and 30mm). Investigation of the ratio of the largest side lobe to the main lode was also done for the same locations. The results for the planes Z = 30mm, 60mm, and 100mm are summarized in Figures 2.8. Examination of Figures 2.8A and 2.5B shows that for the plane Z = 30mm, the peak pressure squared decreases by approximately 53% as the focus moves from the origin to the x = y = 30mm corner of the plane, with the 3dB volume increasing by 430%. Also of note is the fact that for the distances farther away, the change in peak pressure is very much less. As can be seen from Figure 2.5-2.7 and Figures 2.8C and 2.8D, the 3dB beam length shortens and in general, the sidelobes decrease relative to the main peak as the focus is moved off axis. Additionally, the similarity between the x and y 3dB widths in Figures 2.8 E and F should be observed.

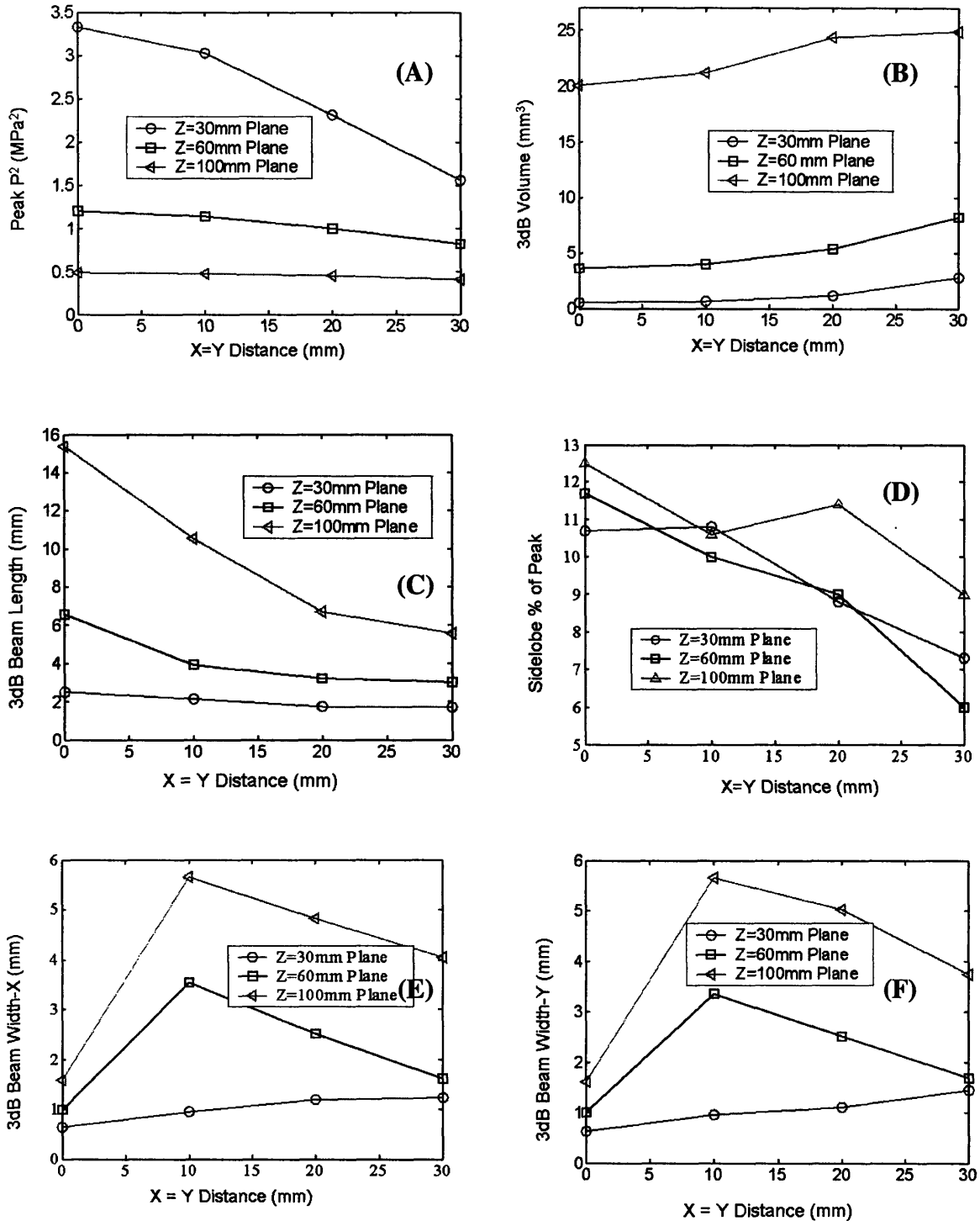

Figure 2.8 Graphs of the relationship focal distance from plane origin and focal metrics. (A) between location and peak focal pressure squared, (B) between location and 3dB volume, (C) between location and 3dB beam length (D) between location and side lobe % of the peak pressure squared, (E) between location and 3dB X beam width, and (F) between location and 3dB Y beam width

2.3.2 Array Size Results

To investigate the effects of array size on the metrics discussed in section 2.3.1, the array size was varied from 32x32 elements to 128x128 elements, in increments of 16x16 elements (7.2mm aperture increase), with the same parameters and orientation described in section 2.2.2. Figures 2.9 and 2.10 show the pressure square fields for at 64x64 element array and a 32x32 element, each with 0.45mm x and y spacings, and conditions previously described for the 128x128-element array. Note that for the off axis plots, value of 14mm and 7mm were used for the 64x64-element array and the 32x32 element array respectively. These values were chosen as they lie on the edge of the array field for their corresponding transducers. Observe that there is increased grating lobe formation as the array becomes smaller, with significant extra focal constructive interference in the 32x32-element configuration.

Figure 2.11 shows the relationships between array size, the peak focal pressure squared, sidelobe to main lobe ratio, and 3dB volume, length and x and y width for focii at (0,0,30) and (10,10,30). As shown in Figures A-D, E and F, the focus, in general becomes tighter as more elements are added.

(A)

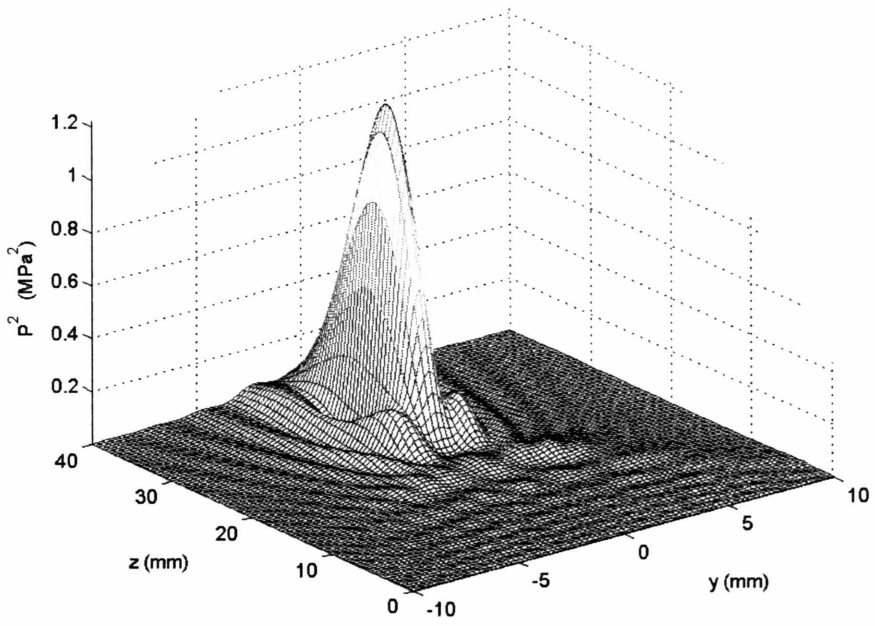

(B)

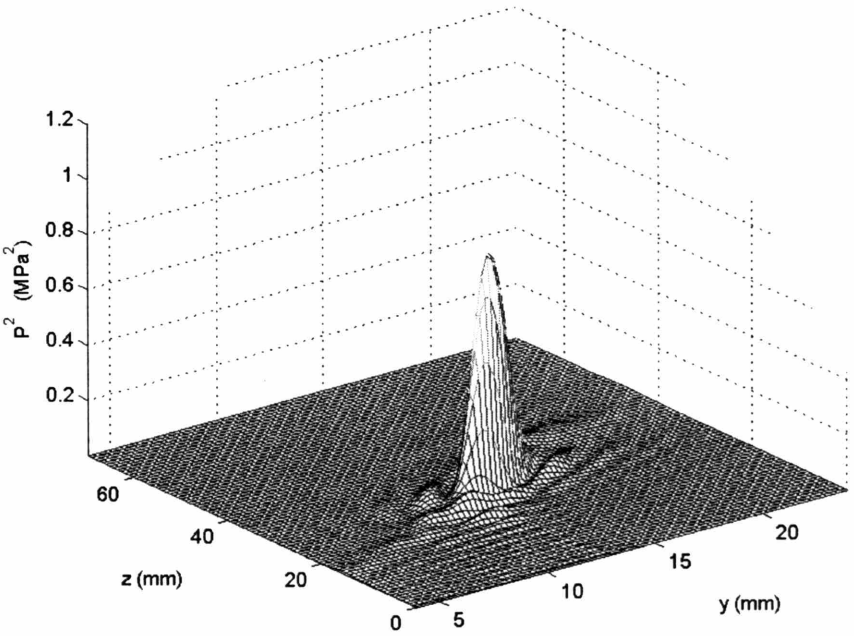

Figure 2.9 A diagram of the pressure field squared for a 64x64 element array (A) Focus at (0,0,30) (B) Focus at (14,14,30)

(A)

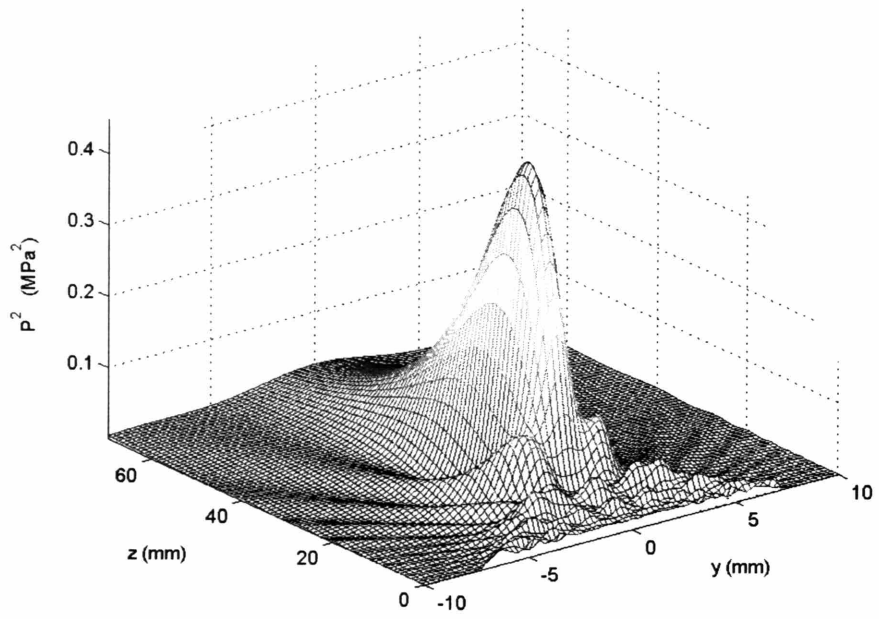

(B)

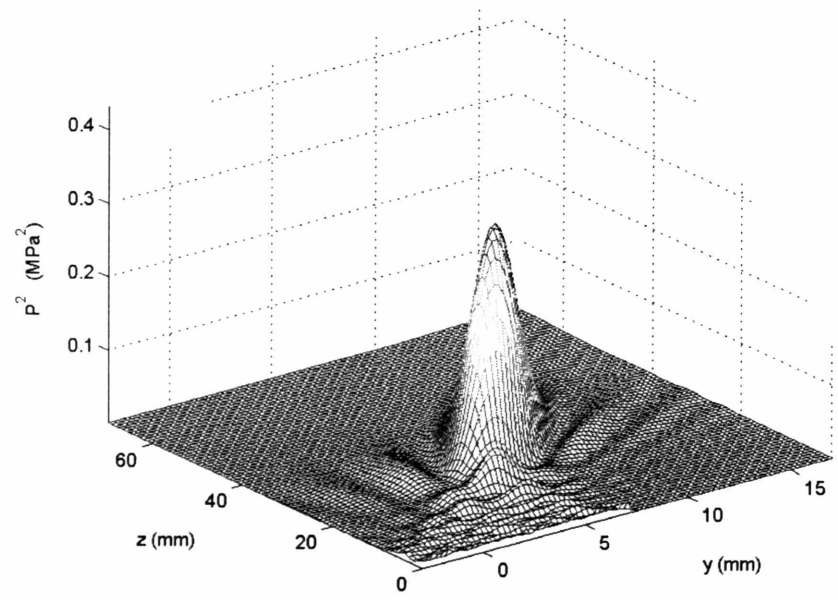

Figure 2.10 A diagram of the pressure field squared for a 32x32 element (A) Focus at (0,0,30) (B) Focus at (7,7,30)

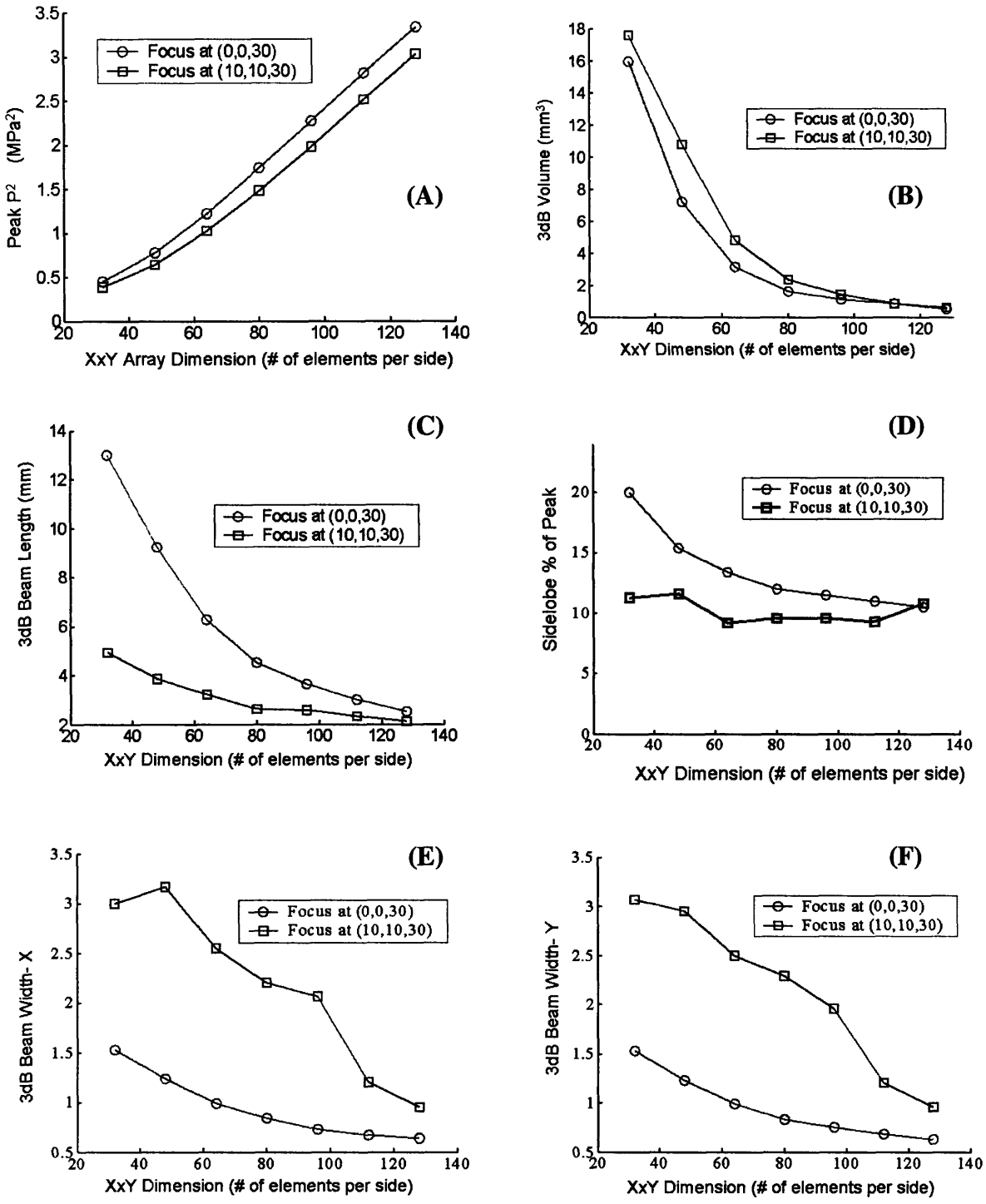

Figure 2.11 Graphs of the relationship between array size and focal metrics. (A) between size and peak focal pressure squared, (B) between size and 3dB volume, (C) between size and 3dB beam length (D) between size and side lobe % of the peak pressure squared, (E) between size and 3dB X beam width, and (F) between size and 3dB Y beam width

2.3.3 Apodization Results

Using the same metrics and orientation as those in sections 2.2.1 and 2.2.2, a study of the effects of varying the power used by each element was investigated for a 128x128 element array, with foci at (0,0,10) and (0,0,30). Figure 2.12 shows the pressure squared field and 10% contour plots for the 128x128 element array. Figure 2.13 shows the focal metrics for the apodized and nonapodized cases for foci in the planes Z=0mm and Z=30mm. Of note is the general closer agreement between the values in the plane Z=30mm than those in Z=10mm, as shown in figures 2.13 A, C ,D, and E . Also, observe that the largest variations usually occur at the extremes, x=y=30mm in each plane.

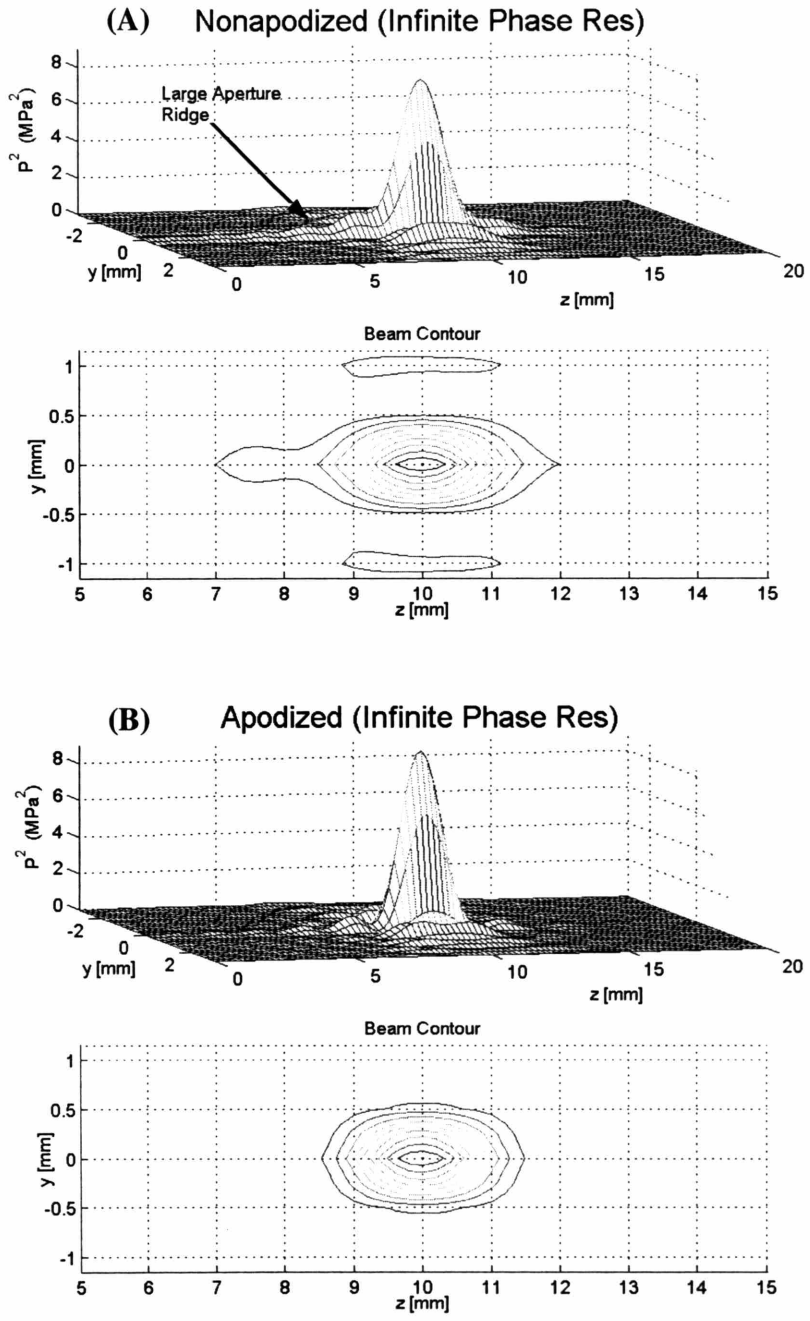

Figure 2.12 A diagram of the pressure field squared and 10% contour plots for a 128x128 element array with the focus at (0,0,10) (A) The nonapodized case (B) The apodized case

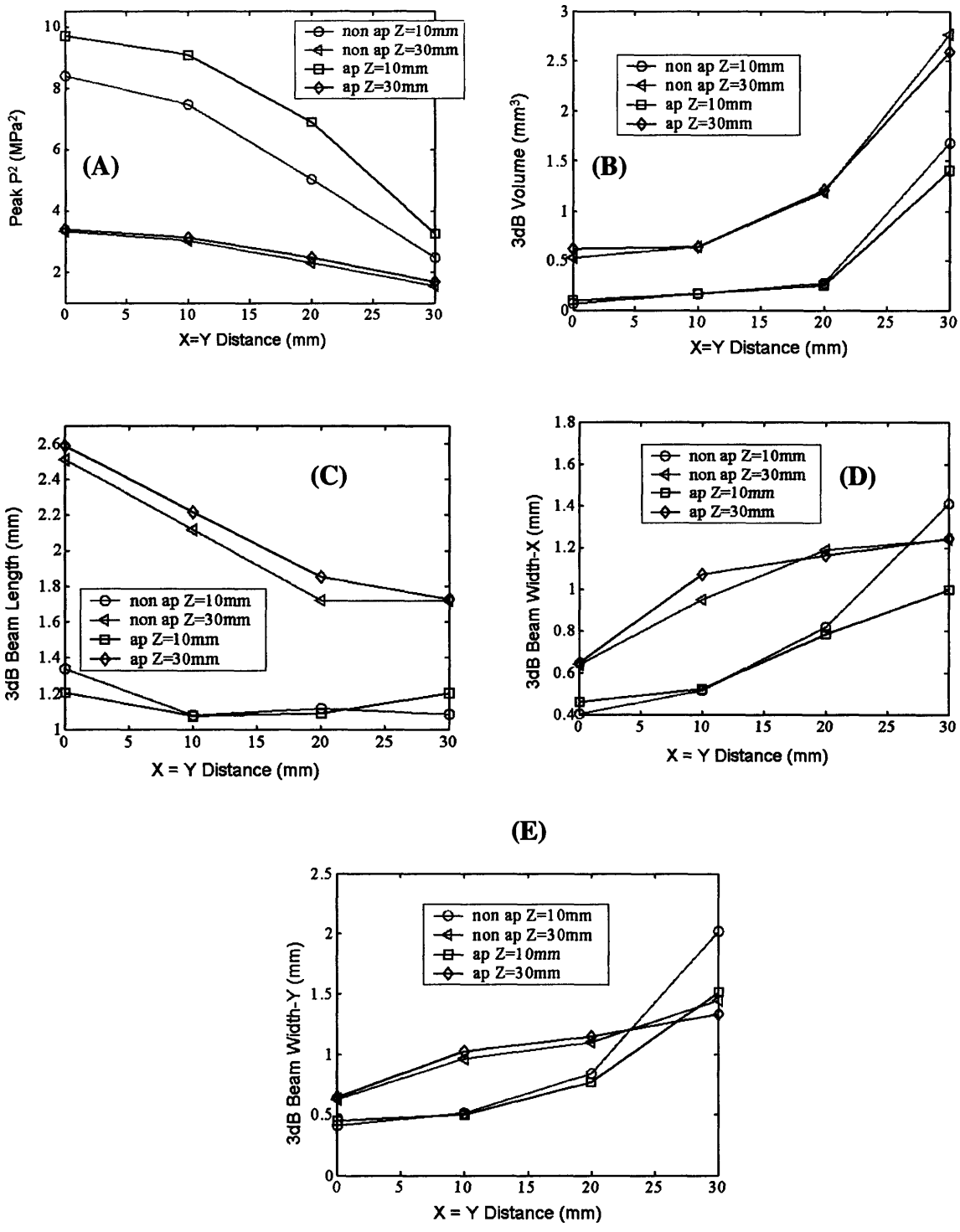

Figure 2.13 Graphs of the relationship focal distance from plane origin and focal metrics for an apodized and nonapodize 128x128-element array. (A) location and peak focal pressure squared, (B) location and 3dB volume, (C) location and 3dB beam length (D) location and 3dB X beam width, and (E) location and 3dB Y beam width

2.4 Discussion and Conclusions

Examination of Figure 2.8B shows an increase in 3dB focal volume as function of off-axis distance. It should be noted that while the 350% increase may initially seem large, at the edge of the field, the total volume is still less than 2.6mm^3. In addition focal volume for the planes Z=60m and Z=100mm remain relatively flat, as does the peak pressure squared, suggesting that father away from the array beam steering has less of an effect on the quality of the focus. Investigation of Figures 2.5-2.7 show the expected effects of steering, as the focus rotates towards a diagonal orientation as the beam moves to the edge of the array. However, the usual severe spreading found at the extremes of the plane are not as apparent. This is the result of the large number of elements, which help maintain the integrity of the focus, despite its location near the periphery of the array field. These results suggest that a high degree of focal precision could be maintained even when the focus is steered to the edge of field, provided that there is a sufficiently large number of elements.

Figure 2.11 shows the relationship between focal metrics and the number of elements as it relates to array size. Examination of the graph reveals the peak pressure squared and the 3dB volume are similar for both foci as function of size, implying that the localized delivery of the power is similarly effective. However, inspection of Figures 2.11 C, E, and F show that a divergence occurs between the 3dB length and width as the array gets smaller, with the length growing when the focus is at the origin, and the width when it is off axis. This is consistent with one would expect. Figure 2.11 shows that the beam steering capability begins to quickly degrade once the array becomes smaller than 64x64 elements, with the volumes of the foci both on and off axis increasing substantially below that size. This dramatic change is not surprising as the ratio of the number of elements between each successive increment begins to grow substantially at the point, e.g going from 64x64 elements to 48x48 represents a decrease of 45%, where as the reduction from 128x128 to 112x112 is only 23%. However, as Figure 2.9 shows, for a 64x64 element array, the grating lobes remain suppressed, while the sidelobes are below 15%, which is an acceptable limit. This implies that even with a reduced number of the elements, a 64x64 element device would still demonstrate good steering capability. These

results taken together with the previous outcomes for the 128x128 element array suggest that at distances where the f number (ratio between the distance from the array center to the focus and the width of the array) is between ½ and 1, phased arrays provide a useful means for effectively delivering directed power to a specific location.

Figure 2.12A shows the presence of a pressure "ridge" which occurs when the focus is brought close to the surface of a large aperture array. Figure 2.12B shows that when the power is apodized, the ridge can be reduced, though not eliminated completely. Inspection of Figure 2.13 A reveals the additional value of using this power scheme. The figure shows that for all focal positions in the Z=10mm plane, the apodized peak pressure squared is higher than that for the nonapodized case, by more than 31%in most cases. The 3dB beam length and width also show slight improvements for the nearer plane. As one might expect, the metrics for the two cases show more agreement in the Z=30 plane, where the relative differences in distance from the focus to individual elements is less. As such, apodizing the power appears to be effective for increasing array performance in the region close to the array surface, offering little benefit father away. It should be noted that, while the "ridge" is relatively small compared to main lobe, minimizing its impact is still useful, e.g. in a situation where cavitation is occurring and thresholds for creating tissue damage have been reduced.

.

3 Quantized Input Phase Model and Simulations

3.1 Introduction

In this chapter we examine the effects of input phase quantization on focal quality and beam steering capability. To evaluate the effectiveness of this technique, a computer model was developed, which would provide insight into the impact of various physical parameters on the ultrasonic field. In this section, we provide a theoretical basis for the design of actual systems that might employ this assignment scheme. The aim is to optimize the relationship between the number of phase inputs, focal quality, beam steering capability and array size. In anticipation of possible constraints imposed by future hardware implementations, an analysis is conducted to understand the impact of equalizing the number of times each phase is used during a given sonication (called phase representations). Two techniques for achieving equal phase representation are examined to determine which is more effective. If successful, the quantized phase protocol would provide a means for being able to drive ten thousand or more elements with very few input lines.

3.2 Material and Methods

3.2.1. Numerical Simulations

3.2.1.1. Simulation Parameters.

As in chapter 2 section 2.2.1, the pressure fields were simulated using the Rayleigh-Sommerfeld sum, in conjunction with Huygen's Principle. Similarly, each element was modeled as being composed of 9 simple sources that all used the same phase. First simulations were run for a 128x128, 1.1 MHz, array with 0.44mm x 0.44mm elements having center-to-center diagonal spacings of 0.64mm and x and y spacings of 0.45mm to determine the optimal balance between the number of phase input increments and the peak focal intensity. After the relationship between the number of phase increments and peak intensity was determined, additional simulations were run to characterize the focal properties. The medium was assumed to be water, where the speed of sound, $c = 1500m/s$, the density, $\rho = 1000kg/m^3$ and the attenuation coefficients, $\alpha =$

2.88×10^{-4} Np/m/MHz (Duck 1990). The total output power of the array was 1W. The transducer orientation is the same as that given in Figure 2.1, in the previous chapter.

As before, the resolution in the calculated pressure field in the x, y, and z directions was 0.22 mm, which gives a volume resolution of 1.1×10^{-2} mm^3. For each case, the focus was electronically steered to a number of locations and the effect on peak focal pressure squared, the ratio of side lobe to main lobe, and the 3dB length and volume, and the overall pressure field was observed. Following the previously designed protocol, the 3dB beam length and x and y widths were measured by visual inspections of the associated graphs and the peak pressure squared, side lobe ratio and 3dB volume were calculated by the program. All simulations were written using MATLAB and were run using a PC with an Athlon XP 2800 processor.

3.2.1.2. Array Size

To investigate the effects of array size on focal control, the dimensions of the 2D array were varied. In each scenario described in section 3.2.1.1, the array size was increased from 32x32 to 128x128 elements with simultaneous x and y steps of 16 elements (an aperture increase of 7.2mm). The impact on focal quality was measured using the same metrics as in section 3.2.1.1. The focus was steered in the plane Z=30mm at (0,0,30) and (10,10,30)

3.2.2. Quantized Phase Techniques

In order to reduce the bulk and complexity that results from moving to higher density arrays, the number of input lines to the driving circuitry has to be substantially decreased. One solution is to limit the phase resolution available at the input of the system, thus removing the need for each element to have its own unique driving signal. By having only a limited number of phase values available for all elements to share, the potential for having fewer input lines grows substantially. Configurations with the number of increments ranging from to 2 to 10 were examined. An input scheme using 4 phases was chosen for additional study, as phase resolution beyond this value yielded

only minimal increases in focal pressure amplitude (the limitations of the 4 phase implementation will be discussed in Chapter 4). After this, simulations were run for two cases: 1) where infinite phase resolution was available for the input signals, i.e. whichever phase value was needed to maximize focal intensity was used and 2) where only increments of 0°, 90°, 180° and 270° were available. In all cases, the amplitude of the each element's signal was assumed to be the same. The phase assignments for the 4-phase case are outlined in Table 3.1.

Phase Needed by an Element for an Ideal Focus	Assigned Phase
0° to 44°	0°
45° to 134°	90°
135° to 224°	180°
225° to 314°	270°
315° to 0°	0°

Table 3.1: Phase assignment windows for a 4 phase increment protocol

3.2.3. Equalized Phase Representation

Initial examination of the total number of times a particular phase was used in the 4 phase case revealed differences among the increments. This variation in representation could present problems if an actual system were to be designed based on this concept. One might imagine that the amplifiers needed to drive the lines for the various phase increments might be limited in the amount of current they could deliver, or otherwise constrained in the types of loads they could effectively manage. In anticipation of these and other problems that might result, an investigation of ways to mitigate the possible effects of differences in phase increment representations was performed. Two methods were examined 1) where all representations were made to equal the lowest one, by randomly turning off elements used by the higher phases (called the "sparsing" technique) and 2) where the elements were put in ascending order according to phase, and divided into 4 groups of size equal to the average, i.e. 4 groups of equal size. The

concept of randomizing the elements that are dropped finds its basis in work done by Gavrilov and others, in which showed that system performance can be improved when the elements removed are done so in a non-ordered manner (Gavrilov et al. 1997;Goss et al. 1999). While our study is different in its particular application, the results from Goss's work suggest that the technique is effective in reducing the occurrence of grating lobes, relative to other more ordered methods. The averaging protocol was thought to be an effective candidate based on promising results for the rounding done in our previous 4 phase research. Since the elements that would be affected were close to being assigned to adjoining phase windows initially, it was thought that their reassignment to those windows would have minimal impact on the field.

3.3 Results

3.3.1. Quantized Phase Results

To determine an optimal balance between the number of phase increments and focal resolution, simulations were run for a 128x128-element array, described in section 3.2.1.1. The results of the peak pressure squared simulations are shown in Figure 3.1:

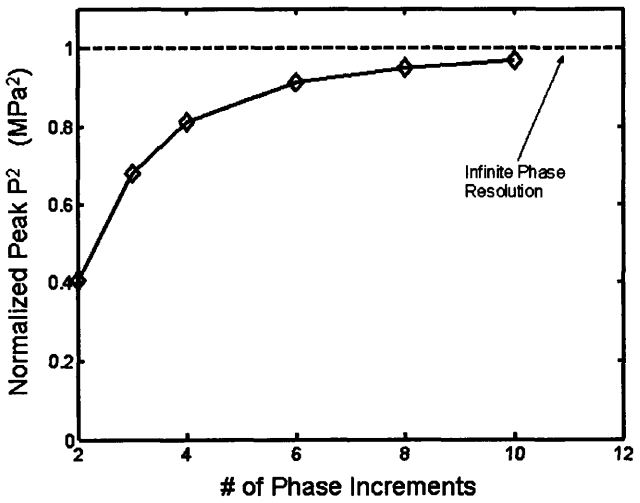

Figure 3.1 A graph showing the relationship between the number of phase increments available at the system input and the peak focal pressure squared for 128x128 element array.

It should be noted that for the 4 phase increment case, the peak value is approximately 80% of the infinite phase result. In this case the maximum error in the phase assignment would be 45°. Since this result was relatively close to the infinite case, and in anticipation of hardware implementation considerations, additional study was done for the 4 phase case. (note: 4 is a power of 2 commonly used in integrated circuit components, e.g. the number switches on a chip, as opposed to 6, which, while giving closer agreement with infinite phase case, is a much less common value in electronics). For the 128x128 element 4 and infinite phase increment cases, simulations were run in which the focus was electronically steered in the diagonal direction with simultaneous x and y increments of 10mm, from 0mm to 30mm, which is the edge of the array field. This was done for planes from z = 10mm to 100mm in 10mm increments. This range includes z = 30mm, which is the approximate location of z = 28.8mm, where the f number is 1/2 and focusing is often performed. Figure 3.2 shows the pressure squared field along the central axis (0,0,Z) for the infinite phase resolution and 4 phase case. Figures 3.3-3.5 show the pressure field squared for foci at (0,0,30)mm and (30,30,30)mm in the planes z = 30mm,. 60mm and 100mm. Figure 3.6 describes relationship between phase quantization, off axis distance and various focal metrics.

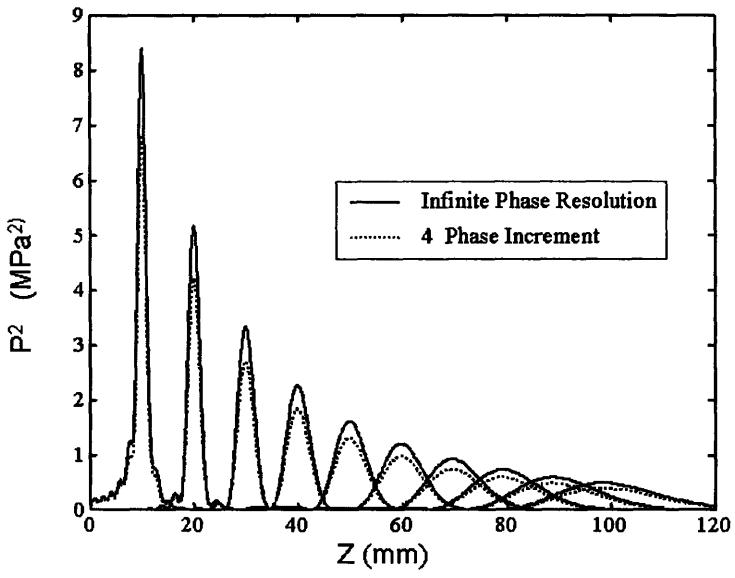

Figure 3.2 A graph of the P2 distribution along the central axis (0,0,Z) for foci from Z=10mm to 100mm in 10mm increments, for a 128x128 element array.

(A)

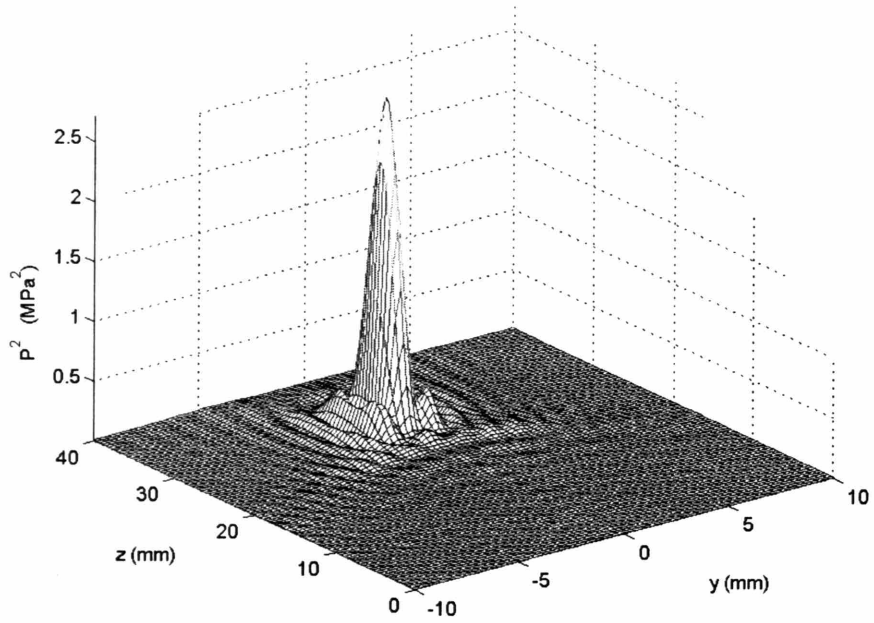

(B)

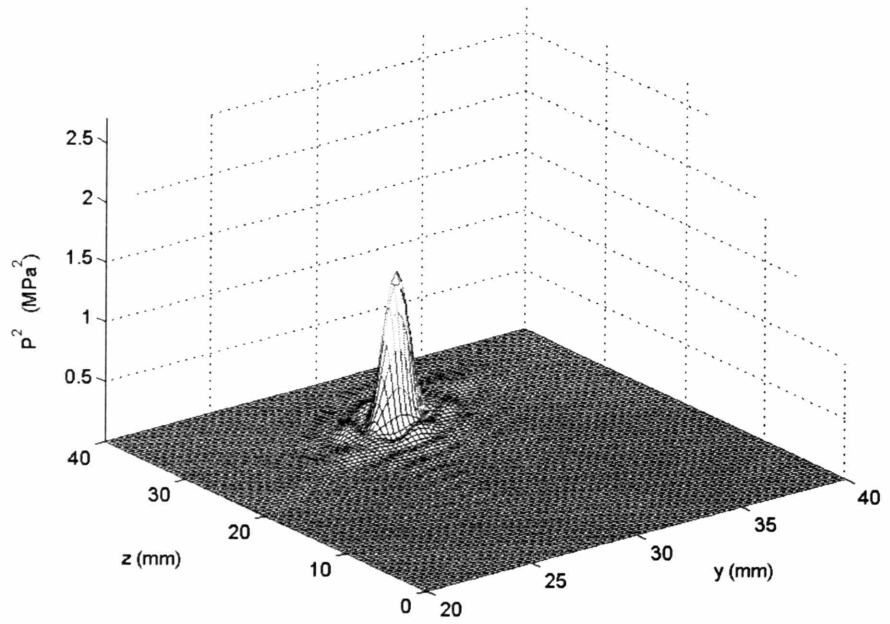

Figure 3.3 A diagram of the pressure field squared for a quantized 4-phase 128x128 element array (A) Focus at (0,0,30) (B) Focus at (30,30,30)

(A)

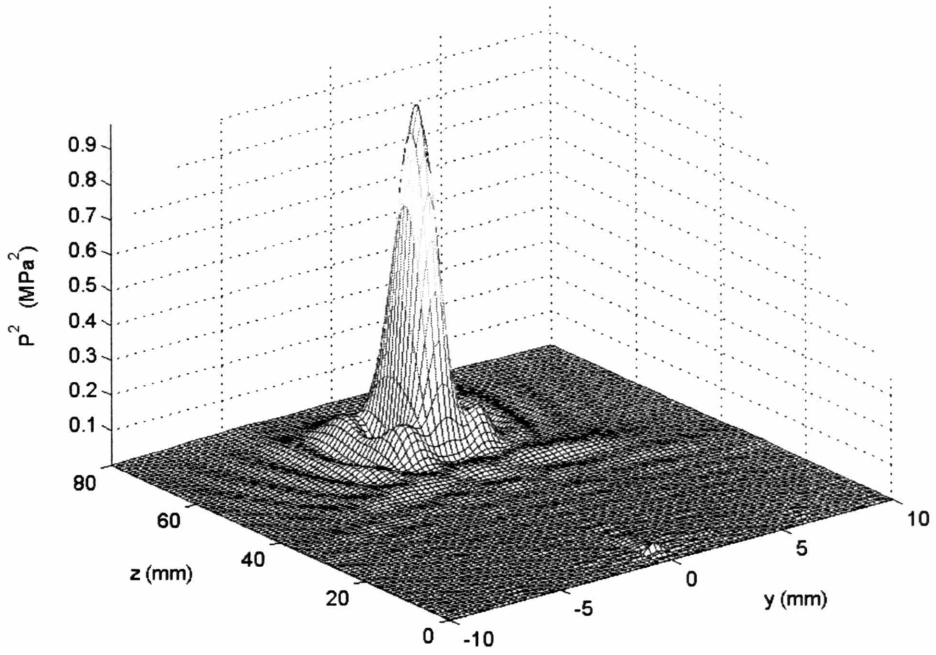

(B)

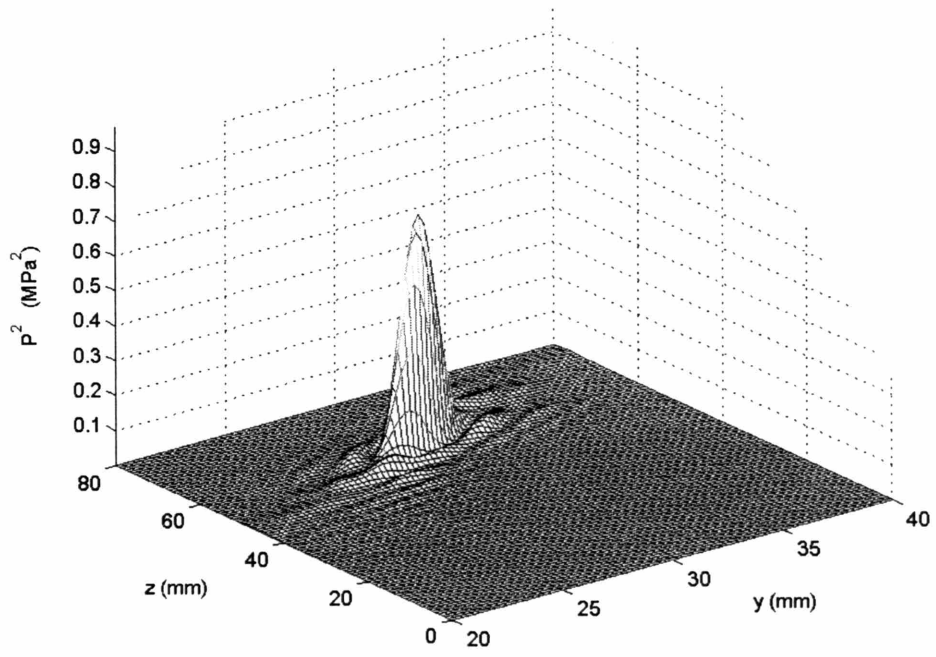

Figure 3.4 A diagram of the pressure field squared for a quantized 4-phase 128x128 element array (A) Focus at (0,0,60) (B) Focus at (30,30,60)

(A)

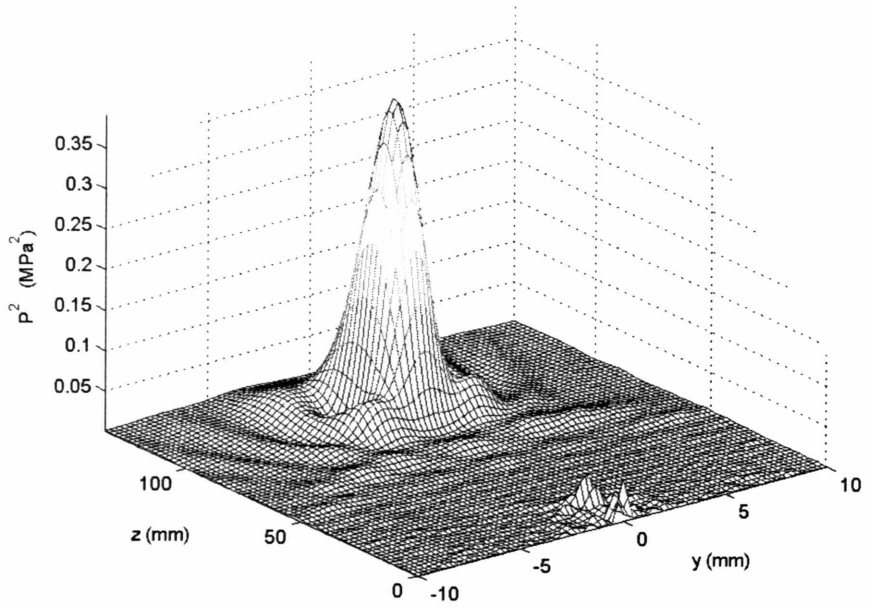

(B)

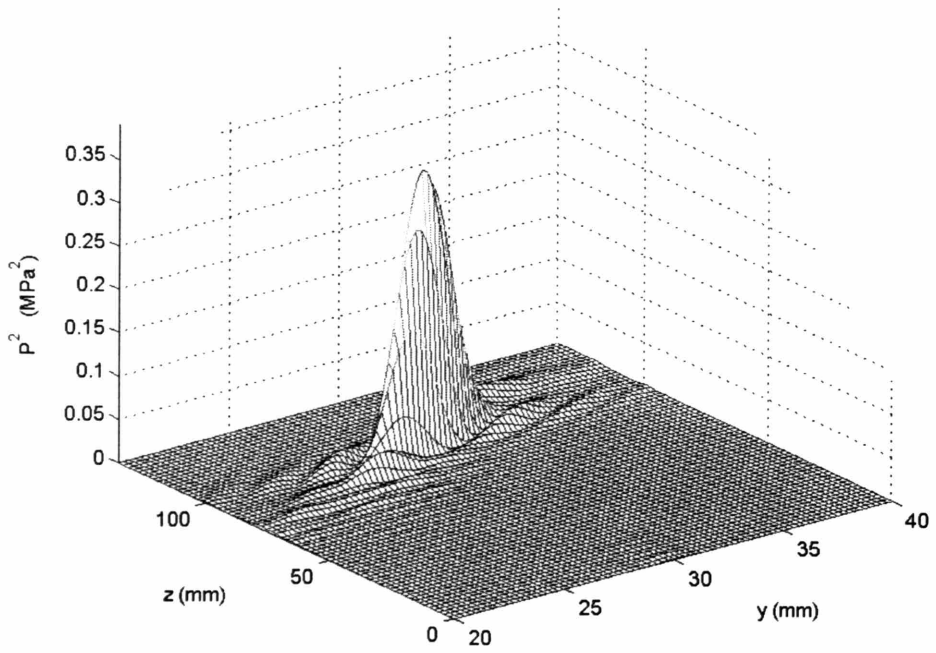

Figure 3.5 A diagram of the pressure field squared for a quantized 4-phase 128x128 element array (A) Focus at (0,0,100) (B) Focus at (30,30,100)

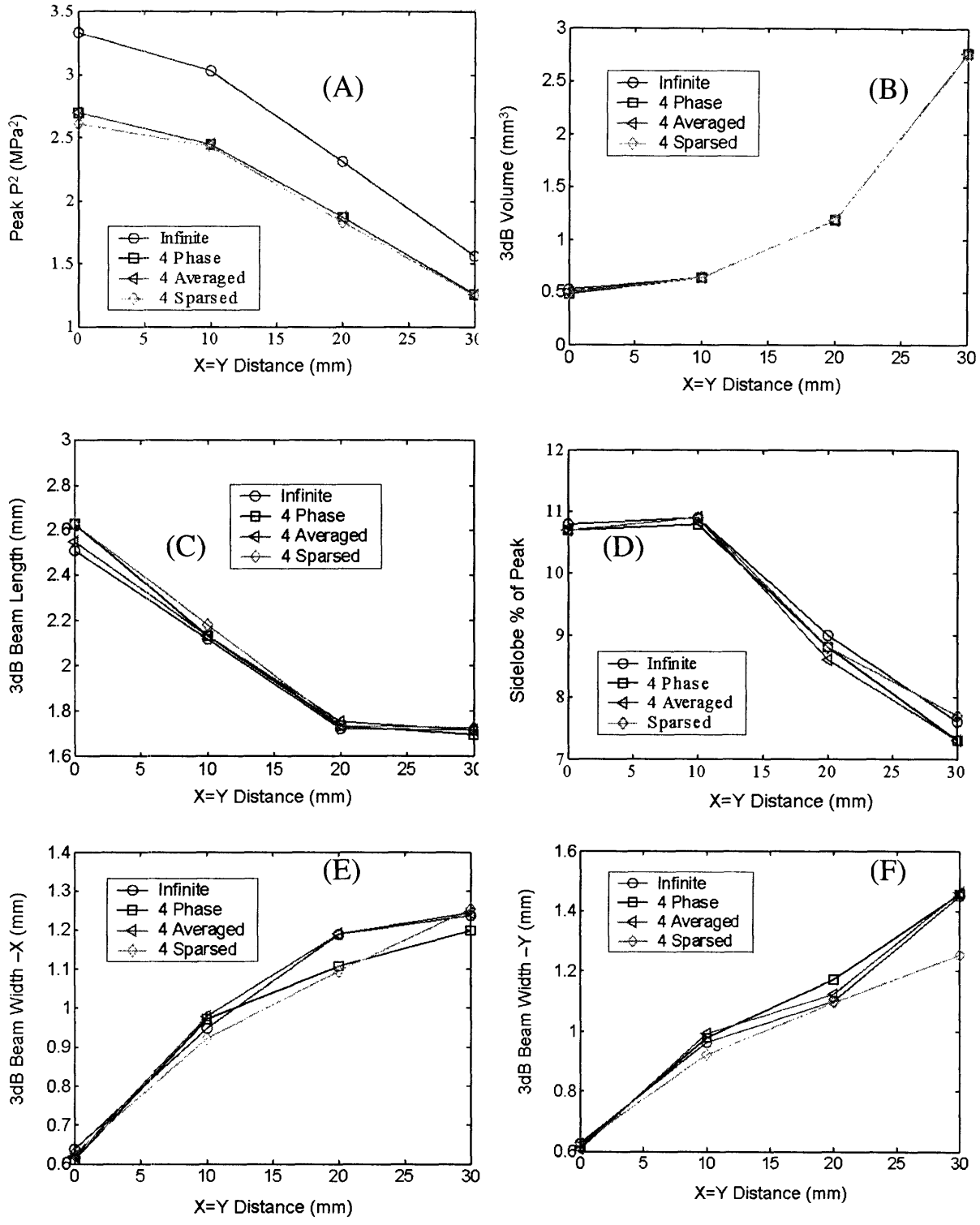

Figure 3.6 Graphs of the relationship focal distance from plane origin and focal metrics in the plane Z=30mm (A) between location and peak focal pressure squared, (B) between location and 3dB volume, (C) between location and 3dB beam length (D) between location and side lobe % of the peak pressure squared, (E) between location and 3dB X beam width, and (F) between location and 3dB Y beam width

Observe that the general trends for the quantized cases follow that of the infinite resolution case. The close agreement case be in seen in Figure 3.6 B, C, and D , which show the sidelobe % of the peak and the 3dB volume and length for the quantized configurations are all within 7% of the ideal case. Larger variation can be seen in the 3dB widths shown in Figures 3.6 E and F, in which the differences approach 25%. The greatest overall deviation comes in the peak pressure squared values, shown in figure 3.6 A, where the difference is approximately 20% at the origin and 17% at the edge of the field.

3.3.2 Equalized Phase Representation Results

The results for the 4 phase increment simulation revealed that there was a difference in the number of times each phase was used, for various focal locations. Further investigation revealed the geometric relationship between the phases used and their location on the array itself. Figure 3.7 gives an example of how the phase increments are distributed for a 64x64 element array operating under the same conditions described in section 3.2.2 (the elements size and spacing are also the same).

These phase assignments shown in Figure 3.7 are consistent with what one might intuitively expect. Figure 3.7A shows a center region where the 0^{o} reference is concentrated, with the other phases forming circles around it. This pattern follows from the fact that the elements on the circles are equidistant from the focus. Figure 3.7B shows that as the focus is moved off center, the phase assignments follow in a roughly proportional way. It should be noted that in this example a 64x64 element array has been used, however the results for a 128x128 element array would be very similar. In fact the 64x64 element center of the 128x128 element structure would be identical to Figure 3.7, and would have additional rings on the outside for the extra elements. In this case, the 64x64 element case was given in order to permit better viewing of each element.

(A)

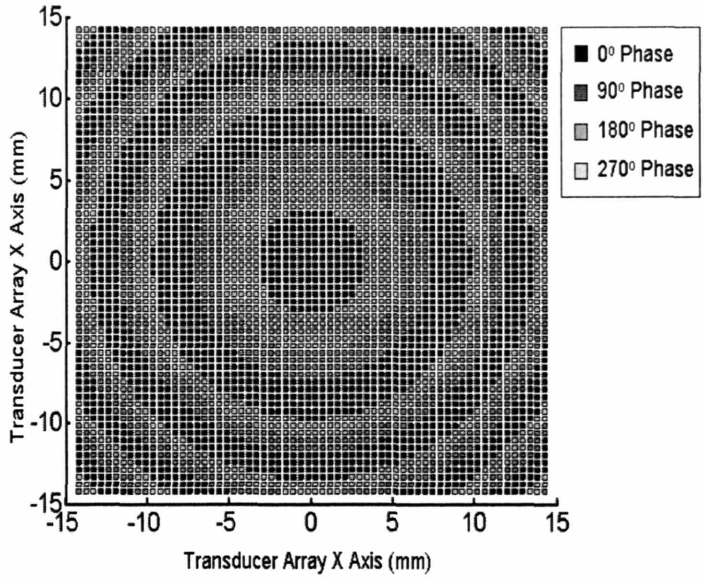

(B)

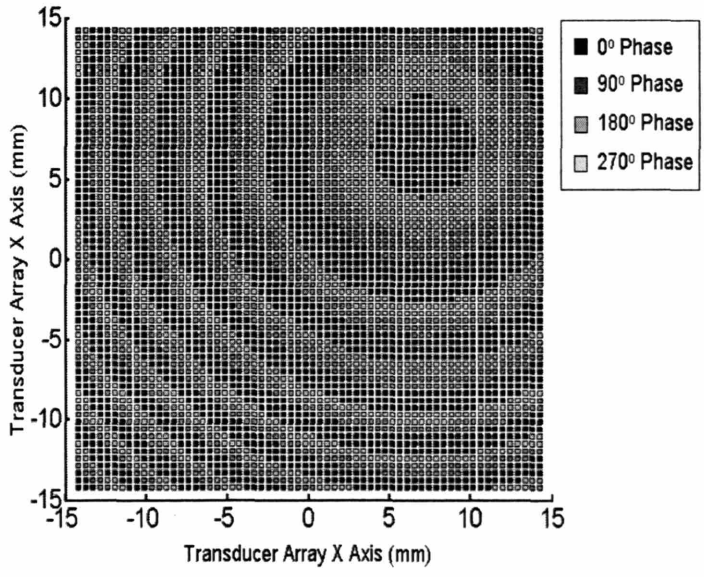

Figure 3.7 A diagram of phase assignments for a 64x64 elements array. A) shows the assignments for a focus at (0,0,30) and B) shows assignments for a focus at (7,7,30). Note: the assignments for a 128x128 element array has identical values for its 64x64 element center, but has more rings on the outside.

If one were to examine the elements for the 128x128 element case with 4 phases, one would find that in summing the total used for each increment, one would get the values given in Figure 3.8. The graph shows that at the origin in the plane Z = 30mm there is an approximately 5% difference in the number of elements driven at 90° and 180°, which represents the largest variation. When the focus is moved to the edge the array field at X=Y=20mm, in the plane Z=100mm, the values move farther apart, with the largest difference being 18%, between 90° and 180°.

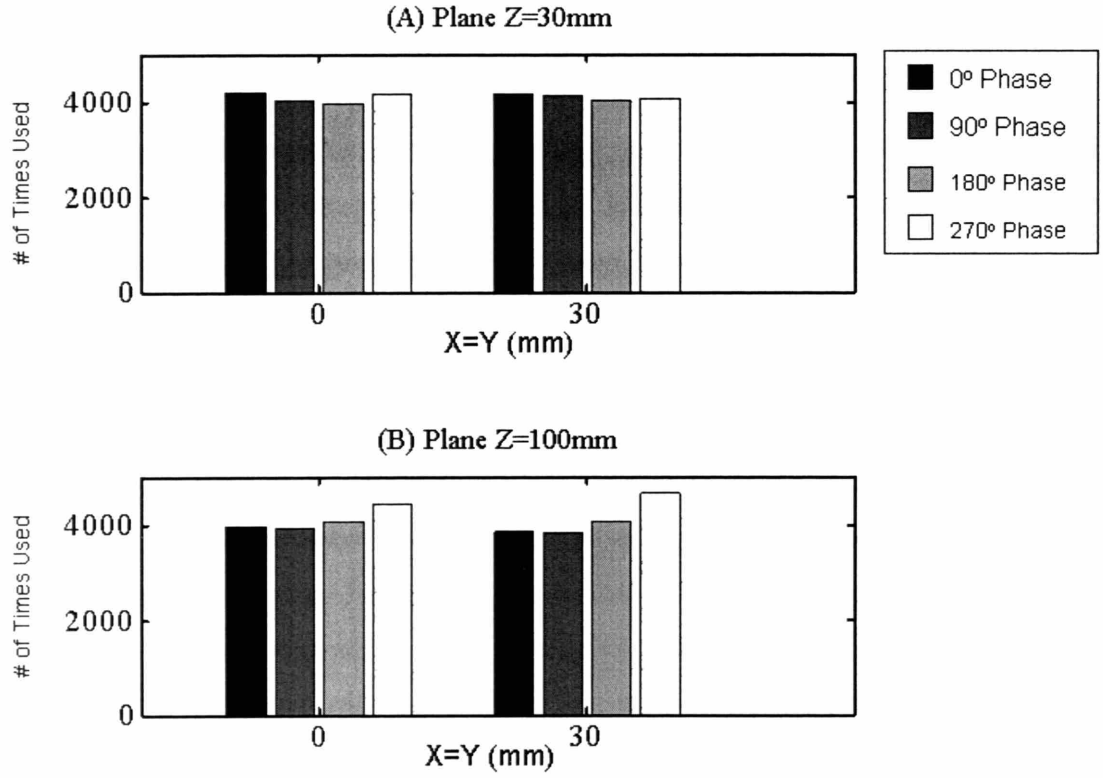

Figure 3.8 A graph of the number of times each of 4 phase increments is used for a 128x128 element array, at the origin and X=Y=30mm A) in the plane Z = 30mm and B) in the plane Z = 100mm.

In general as the focus moves farther from the origin, the differences in representation increases. Of note is the fact that for the farther distances, 80m and 100mm, the greatest difference occurs at X=Y=20mm.

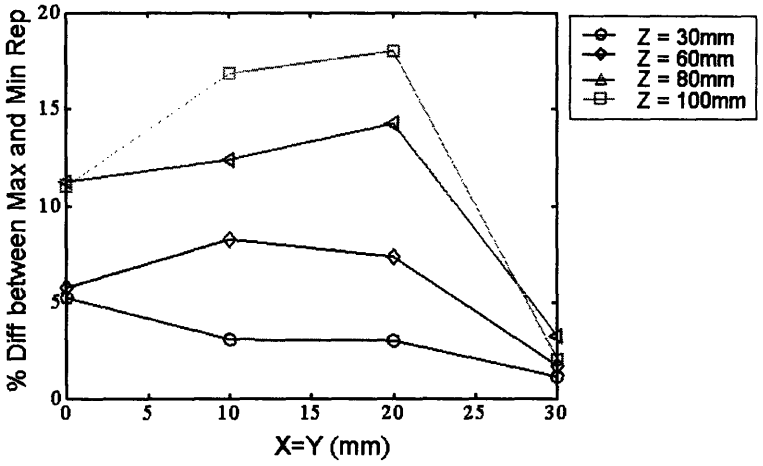

Figure: 3.9 A graph of the relationship between the percent difference between the most represented phase increment and the least represented and the distance from the origin.

It should be noted that, while there are differences in the number of times each phase is used, as shown in Figure 3.6 and Figures 3.10 and 3.11 in the next section, the metrics and overall field for the equalized cases are very similar to the simple quantized case, which closely follows the infinite resolution case. As such, the equalizing protocols are effective in preserving the flexibility offered by quantizing the phase resolution.

3.3.3 Size Results

Figure 3.10 gives the pressure squared field for 64x64 element array 4 phase increments and focus at (0,0,30) and (14,14,30) which represents the edge of the field. Figure 3.11 shows the pressure squared field for the two equalized phase representation configurations, for a 64x64 element array with focus at (0,0,30). Note the formation of a large grating lobe in the field near the transducer surface. Figure 3.12 shows the field for a 32x32 element array, with the simple 4 phase assignment protocol, and focus at (0,0,30) and (7,7,30). Observe that there is a more severe grating lobe in the field near the transducer surface. Figure 3.13 shows the impact of size on various focal metrics.

As with the offset results in the previous section, the quantized assignment scheme follows the infinite resolution case closely for most values. For arrays 48x48 or larger all metrics agree to within 8%, with the exception being the peak pressure squared and sidelobe % of the peak. For the sidelobe percent of the peak, the values diverge as the size decreases, while for the peak pressure squared, the values converge.

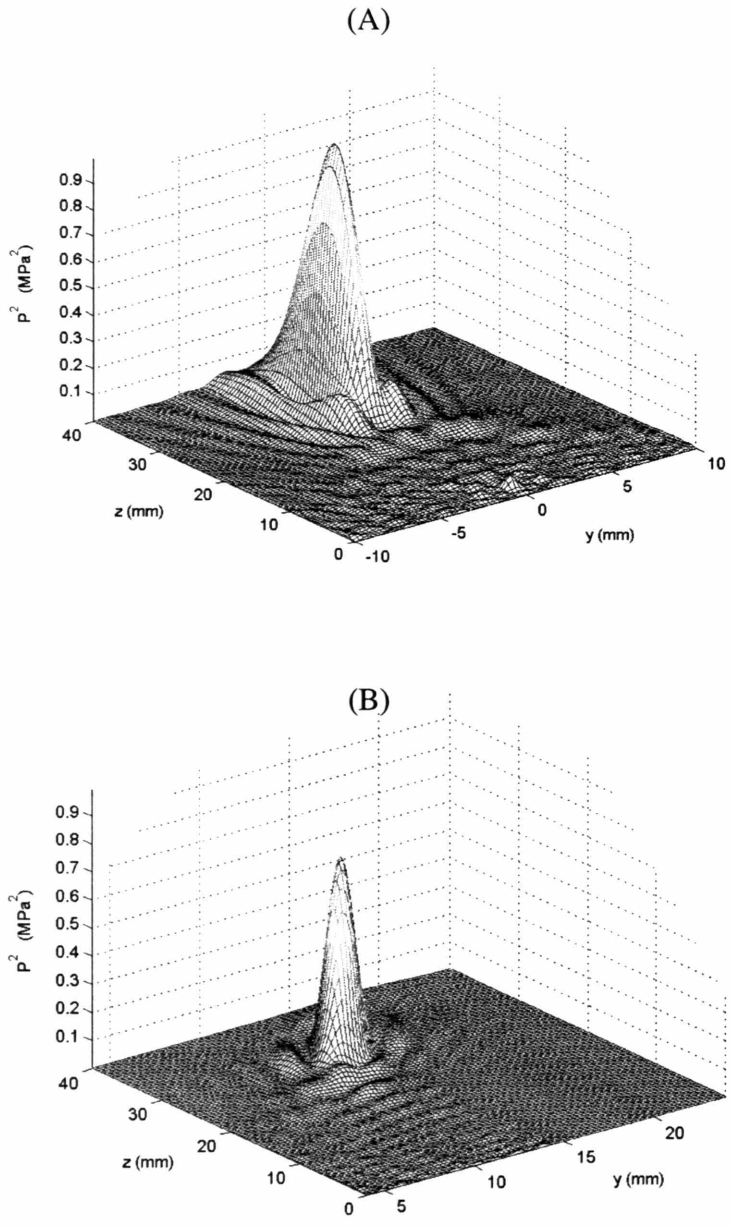

Figure 3.10 A diagram of the pressure field squared for a 64x64 element array with 4 phase increments (A) focus at (0,0,30) (B) focus at (14,14,30)

(A) Sparse Technique

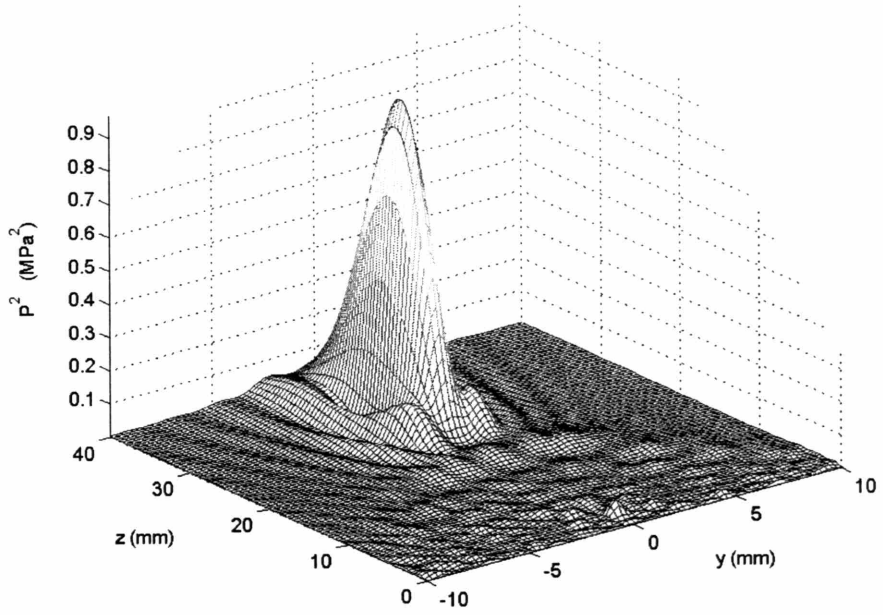

(B) Averaged Technique

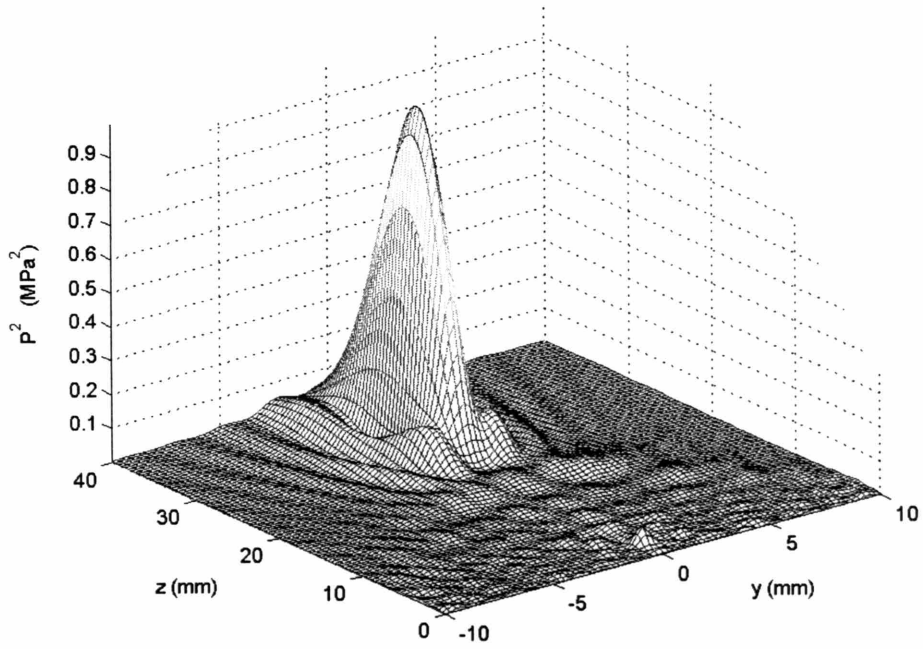

Figure 3.11 A diagram of the pressure field squared for a 64x64 element array with the focus at (0,0,30) (A) The sparse assignment technique (B) The averaged assignment technique

(A)

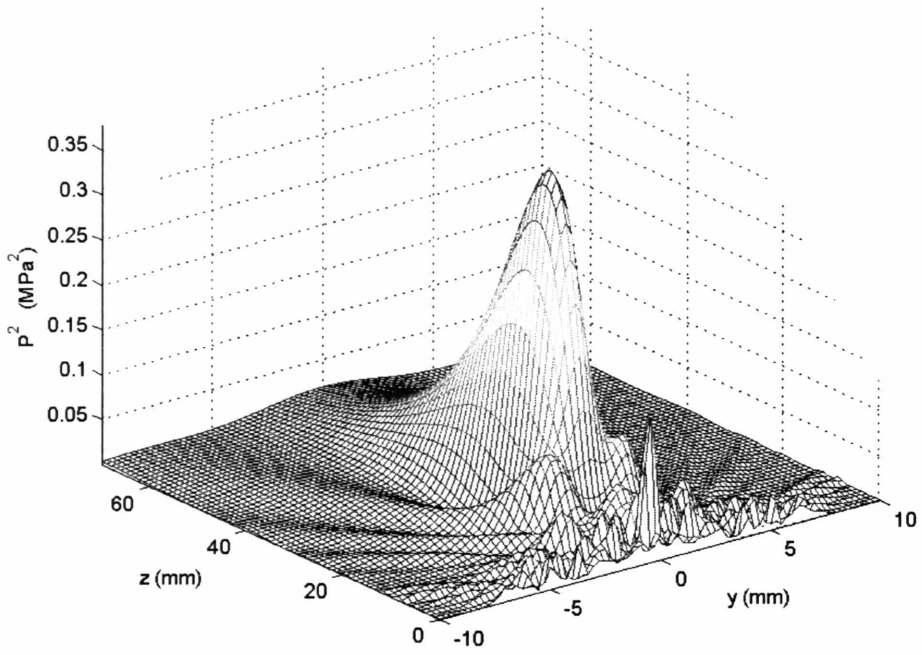

(B)

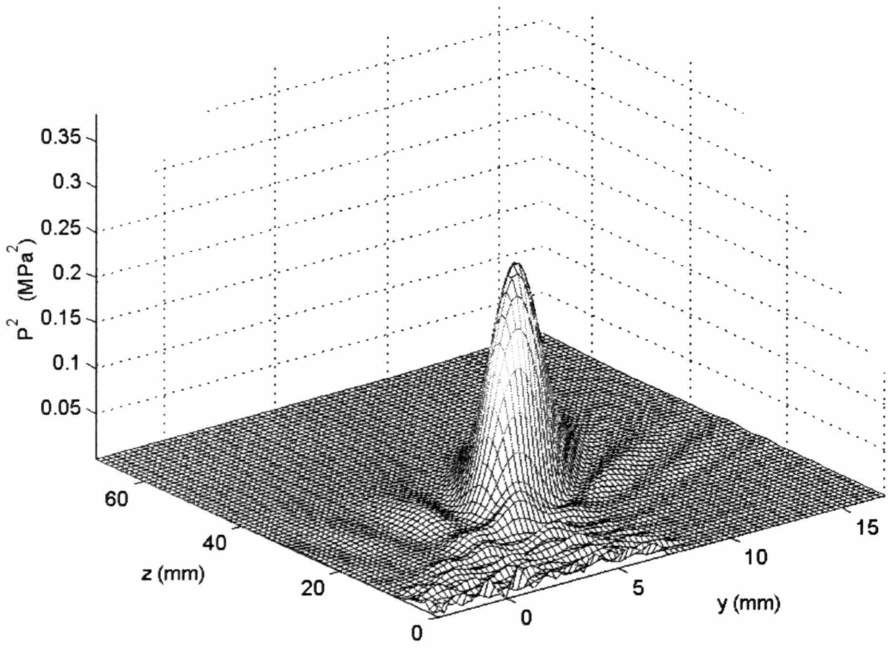

Figure 3.12 A diagram of the pressure field squared for a 32x32 element array with 4 phase increments (A) Focus at (0,0,30) (B) Focus at (30,30,30)

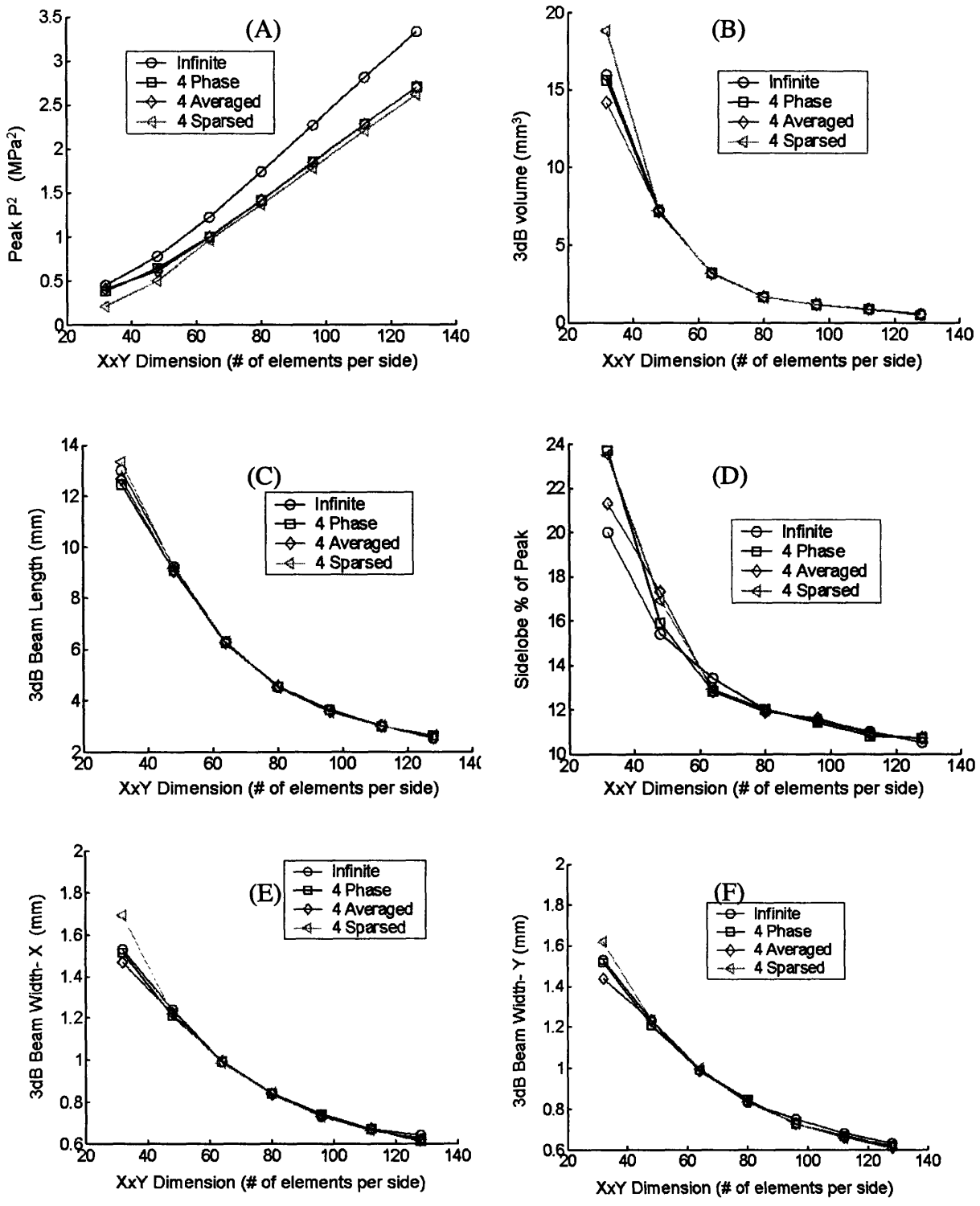

Figure 3.13 Graphs of the relationship between array size and focal metrics with focus at (0,0,30). (A) between size and peak focal pressure squared, (B) between size and 3dB volume, (C) between size and 3dB beam length (D) between size and side lobe % of the peak pressure squared, (E) between size and 3dB X beam width, and (F) between size and 3dB Y beam width

3.4 Discussion and Conclusions

Currently, ultrasound phased array systems use a 1-to-1 addressing and driving scheme for exciting transducers during sonication. This method has proven to be costly in terms of fabrication materials and time. This study has attempted to provide an alternate method for achieving greater focal precision with a simpler phase delivery protocol.

Figure 3.1 demonstrates that using a limited number of phase increments at the system input offers a viable option for greatly reducing the number of signal lines needed to drive the system. The graph reveals that with as few as 4 increments, more than 80% of the ideal peak focal pressure squared can be achieved for a 128x128 element array. If the signal amplitude of each element were increased by approximately 12%, the peak pressure squared could be recovered, while keeping the resulting side lobes below 15% of the main lobe value (from figure 3.6). It should be noted, however, that for focal distances greater than or equal to 60mm, there is the appearance of a grating lobe near the transducer surface. This phenomenon and techniques for mitigating its effects will be discussed further in Chapter 4.

Figures 3.6 D and B show that for the 128x128 element 4 phase increment case, the side lobe to main lobe ratio, and 3dB volume and length are within 7% of the infinite phase resolution configuration. Overall, as a function of distance, the 4 phase cases follow the infinite case relatively closely, with the exception of peak pressure squared which is larger for the infinite phase resolution case.

Examination of figure 3.10 shows that focusing is still possible with a 64x64 element array (29mmx29mm), and that both the sidelobes and grating lobes are within acceptable limits. This general field profile holds for both the quantized phase and infinite phase resolution cases. However, it should be noted that each of the quantized schemes shows the formation of a grating lobes slightly larger than others in the field near the transducer. This feature is much more pronounced in figure 3.12, which shows the field for a 32x32 element array. This feature will be explored further in the next

chapter. For the 64x64 element array, this lobe is much smaller than the sidelobes and would not likely contribute greatly to near field heating if used in an actual device. Investigation of Figure 3.13 shows that, overall, the quantized phase case follows the infinite case for arrays larger than 48x48 elements.

It appears that even with a quarter of the elements in a 128x128 element array, a 64x64 element apparatus still demonstrates good steering capability. These results taken together with the previous outcomes for the 128x128 element array suggest that, overall, quantizing the input phases offers a viable option for substantially reducing the number of input lines for high-density arrays. For a 128x128 element array, using 4 phases, would only require 35 input lines.

An examination of the result from the phase representation equalizing case shows that both techniques show promise for beam steering applications. Both equalization cases show performance similar to the simple 4 phase. Because the averaging added a second level of rounding in the assignment process, it, by design, should yield poorer results. However, because the adjustments were near the edges of the assignment widow, the incremental change to the error introduced by quantization was small. In addition, one would observe that in an actual hardware implementation, the averaging protocol allows for operating in the region where the amplifiers can deliver enough for the minimum phase representation, but not the maximum. In this situation, the method provides an opportunity for driving system to use all of is available resources, i.e. the maximum safe current and voltage. For situations where matching is a requirement, this technique would be extremely helpful since with an equal number of elements, the load for each input would be the same, and thus more easily predicted. As such the same matching circuit could be used regardless of where the focus is being directed. It should be noted that, as a practical matter, if more power were needed for a particular phase increment, additional amplifiers could be run in parallel to solve the current limiting problem, eliminating the need for an equalization protocol.

4 Quantized Apodization and Extreme Field Effects

4.1 Introduction

In this chapter we investigate the effects of focusing near the transducer surface (less than 20mm) and far from the array (more that 60mm). As shown in chapters 2 and 3, when the focus is brought close to the surface, a pressure "ridge" forms, which results from the use of a large aperture. The effects of this phenomenon could be minimized by apodizing the power to each element. However, varying the power to each individually requires a unique driving wire for every element. This would offset the reduction in input lines gained from quantizing the input phase. This section of the study examines the effects of quantizing not only the phase, but also the power apodization. If effective, overall, this technique would still result in a significant reduction in input lines.

In Chapter 3, it was shown that when the phase has 4 increments and the focus is 60mm or farther from the array surface, the grating lobes near the transducer surface begin to increase dramatically. In this chapter we explore the conditions under which this occurs and investigate ways to reduce its impact.

4.2 Material and Methods

4.2.1. Numerical Simulations

As in chapters 2 and 3, the pressure fields were simulated using the Rayleigh-Sommerfeld sum, in conjunction with Huygen's Principle. Unless otherwise stated, the array orientation and parameters are the same as those given in section 2.2.1. The focus was placed in various locations and the effect on peak focal pressure squared, the ratio of side lobe to main lobe, and the 3dB length and volume, and the overall pressure field was observed. Using the protocol developed in Chapter 2, the 3dB beam length and x and y widths were measured by visual inspections of the related graphs and the peak pressure squared, side lobe ratio, and 3dB volume was determined by the program. All simulations were written using MATLAB and were run using a PC with an Athlon XP 2800 processor.

4.2.2 *Quantized Apodization*

As was the case, introduced in Chapter 1 and demonstrated in Chapter 2, the quantized phase configuration showed the presence of a pressure ridge leading from the focus to the transducer surface when focusing in the very near field. The apodization coefficient:

$$K = \left(\frac{1}{d_i}\right)\exp\left[\frac{1}{d_i}\alpha\right] \qquad (2.2)$$

introduced in section 2.2.2 of Chapter 2, can also be used to mitigate this effect. However, as with using infinite phase resolution, using unique input powers for each element requires a large number of wires to control and drive the array. As such, the benefits of quantizing the phase are negated. Consequently, an additional method had to be developed to recover the gains of limiting the phase resolution. A technique that accomplishes this task is to also reduce the number of power levels available at the system input. While employing a larger number of lines than the simple 4 phase case, this method still results is a significant reduction from the infinite phase resolution design.

Employing 6 implementations of input power quantization, the impact on the peak pressure squared field was observed. A review of the results indicated that with only two increments there is a significant reduction in the ridge. As such, additional study was conducted for this configuration, A survey of number of metrics was done, including sidelobe to main lobe ratio, 3dB length, x and y widths, and volume, as well as the over all pressure field. Figure 4.1 gives an example of some of the apodization protocols that were explored.

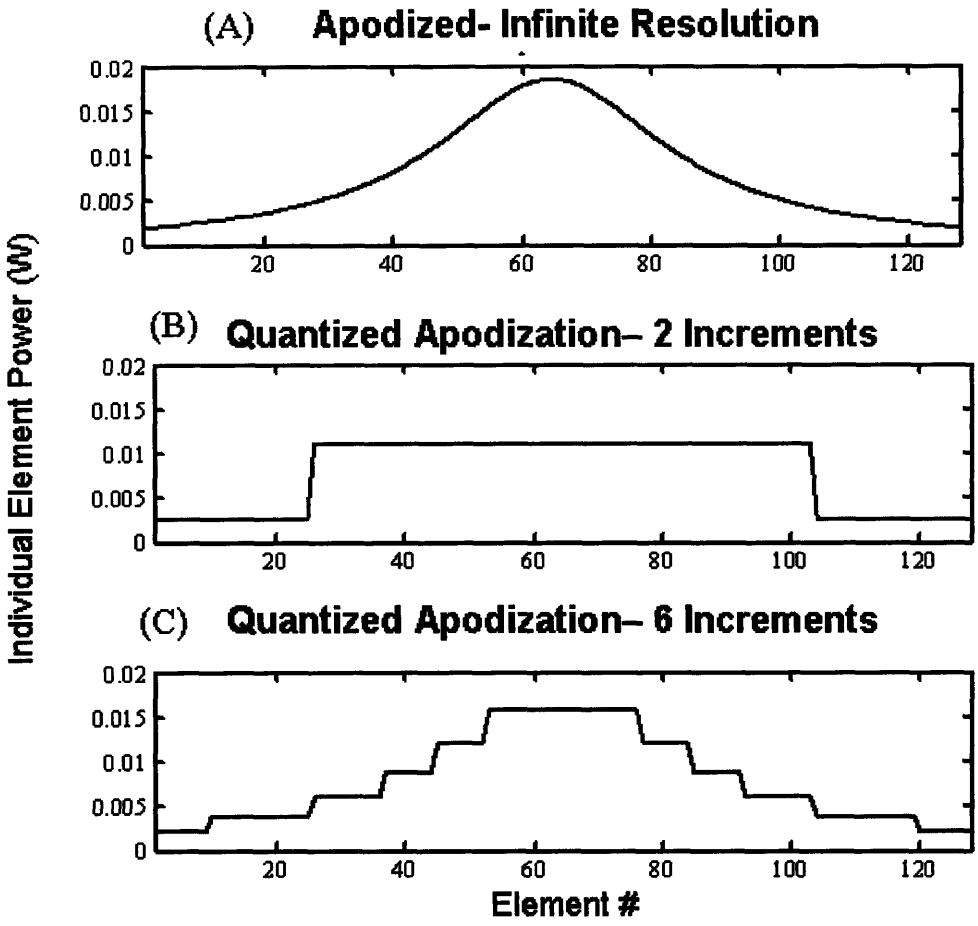

Figure 4.1 Apodization schemes for a linear 128 element array with the focus at (0,0,10) Note this also represents the power distribution for the center x or y line elements in a 128x128-element array

4.2.3 Large Focal Distance Effects

As previously noted, when the focus for a 128 element 4 phase increment array is steered more than 60mm away from the transducer, there is a substantial increase in grating lobe activity. As seen in Figure 4.2A the grating lobes approach the magnitude of the sidelobes, which would make them significant contributors to extra-focal heating. Figure 4.2B shows a more extreme case, which features a 32x32 element array with the focus at Z=30mm. In both examples, the focus is far from the transducer, when compared to its size. To better understand when these grating lobes form, the magnitude was measured as a function of several variables, including array size, distance from the array along the central axis, and distance from the origin in the plane Z=100mm. These simulations were run for the simple 4 phase increment case, as well as the two other equalized representation cases. Deviating from the previous protocol, the resolution was changed in order to view the entire field from transducer surface to 10mm beyond the focus. This was done to permit simultaneous examination and measurement of the grating lobes and the main peak. In the case of the aforementioned metrics, the resolution was 0.25mm in the y direction and 2mm in the Z direction.

(A)

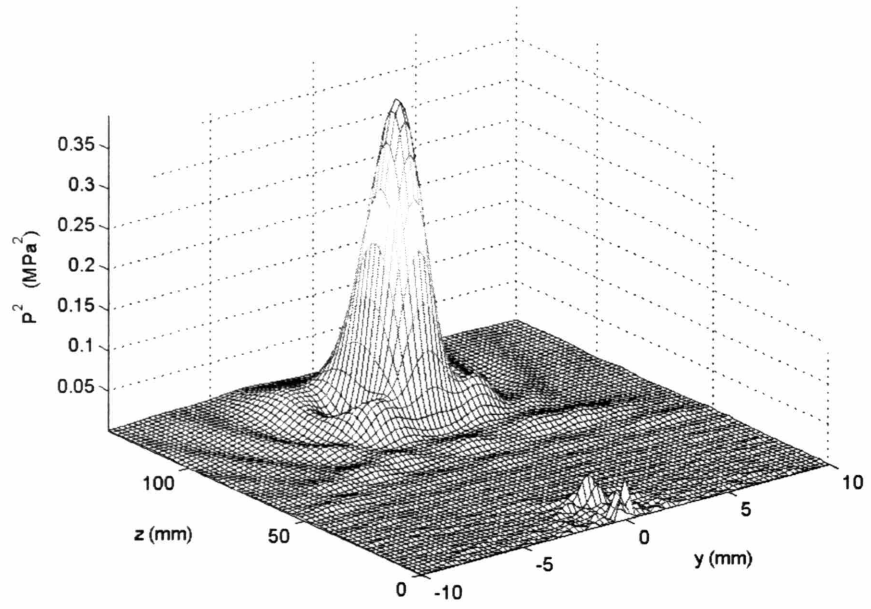

(B)

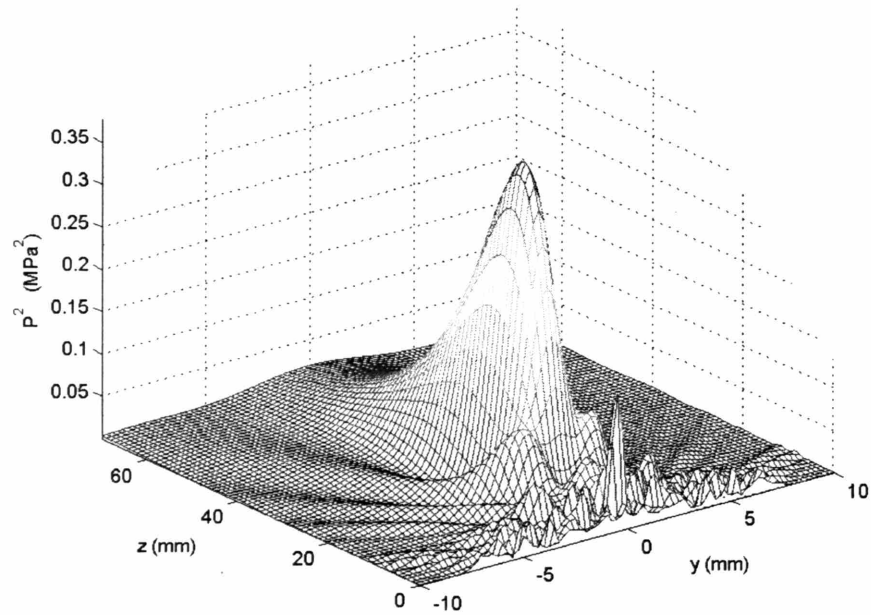

Figure 4.2 A diagram of the pressure field squared for a quantized 4-phase array (A) 128x128 element array with focus at (0,0,100) (B) A 32x32 element array with focus at (0,0,30)

4.2.4 *Energy distribution*

Thus far, it has been shown that for a number of different metrics and configurations, the quantized phase method closely follows the characteristics of the infinite phase resolution case. One consistent exception is the peak pressure. In chapter 3 we determined that for a 128x128 element array with the focus located at (0,0,30), the 4 phase increment arrangement had a peak pressure squared about 80% of the ideal value. One might expect that with a lower peak value, the focus would be less sharp. However, Figure 3.6 revealed that the general shape of the focus and sidelobes for the 4 increment case are very similar to the infinite. The question might arise as to where the rest of the energy goes.

Using a 64 x 64 (~30mm x 30mm) element array with the same parameters described in section 2.2.1.1, a series of experiments was run to show that the energy diverges more in the quantized configuration. To illustrate this fact, the pressure squared field for two xy planes were plotted for the quantized and infinite resolution configurations (portions of planes parallel the array). First, the sum of the field was taken for a 60mm x 60mm plane located 1mm from the transducer surface, with focus located at (0,0,30), i.e. a slice of the field away from the focus was measured. This was done for both phase implementations. This measurement was taken to illustrate the case where the energy does not have enough space to spread out a great deal before being measured. As such, one would expect that the sum for each method would be similar.

Next a plane of the same size and orientation was placed at Z= 9.9mm, and sum of the pressure field squared was measured. Again this was done for both phase assignment protocols. By taking a measure relatively far from the surface, the energy has sufficient distance to diverge, for the less focused arrangement. In this situation, one would expect that the difference between the two sums would be significant. Note that both measuring planes were made to be larger than the size of array. This was done to ensure that field of the diverging energy could also be captured.

4.3 Results

4.3.1 Quantized Apodization Results

As in the case with infinite phase resolution, the quantized phase results showed the presence of a pressure ridge leading from the focus to the transducer surface, when focusing in the very near field. Figure 4.3 shows the impact on the pressure squared field of the 4 phase case, for the various apodization schemes. Note that in both the quantized and simple apodized cases the "ridge" is suppressed. Also note that in both cases the peak pressure squared is higher. Figure 4.4 shows the corresponding 10% contour plots for each design. Observe that the small side lobes found in Figure 4.4A are suppressed or eliminated in the apodized arrangements.

Figure 4.5 gives the effect on various focal metrics as they relate to the apodization scheme and distance from the origin. Observe that in Figure 4.5A the simple apodized 4 phase increment peak pressure squared approaches that of the nonapodized infinite phase resolution case. In addition, note that the 3dB volume, given in Figure 4.5B is very similar for all cases.

(A) Nonapodized 4 Phase

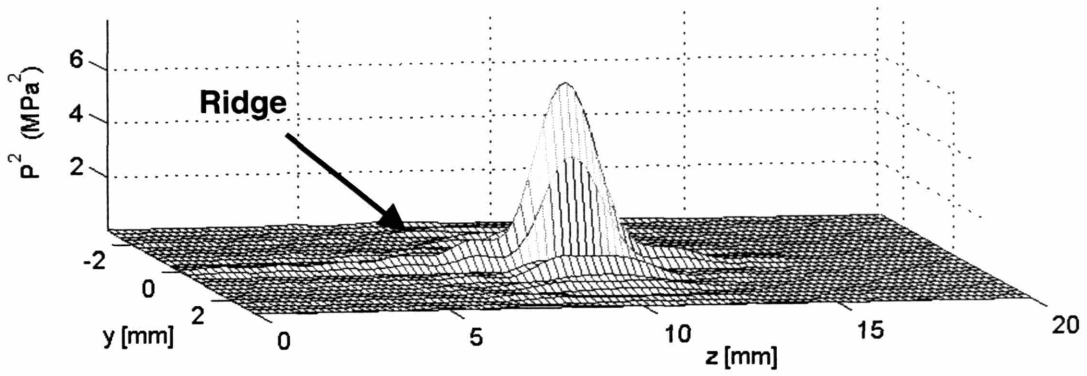

(B) Apodized 4 Phase (Infinite Resolution)

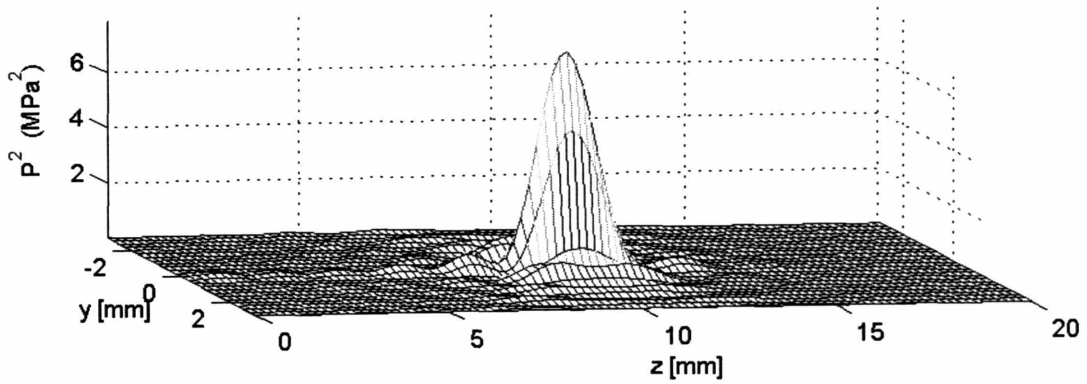

(C) Apodized 4 Phase (2 Step Quantization)

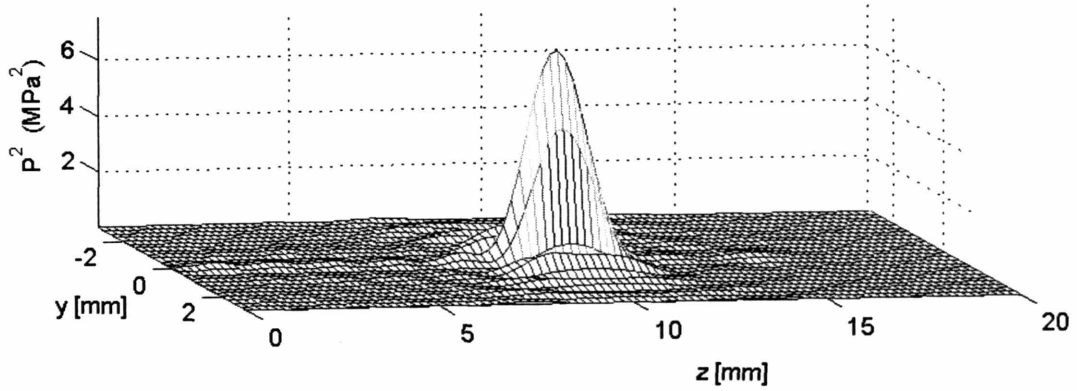

Figure 4.3 A diagram of the pressure field squared for a 128x128 element array with the focus at (0,0,10) (A) The nonapodized 4 phase increment case (B) The infinite resolution apodized 4 phase increment case (C) The quantized apodization 4 phase case

(A) Nonapodized 4 Phase

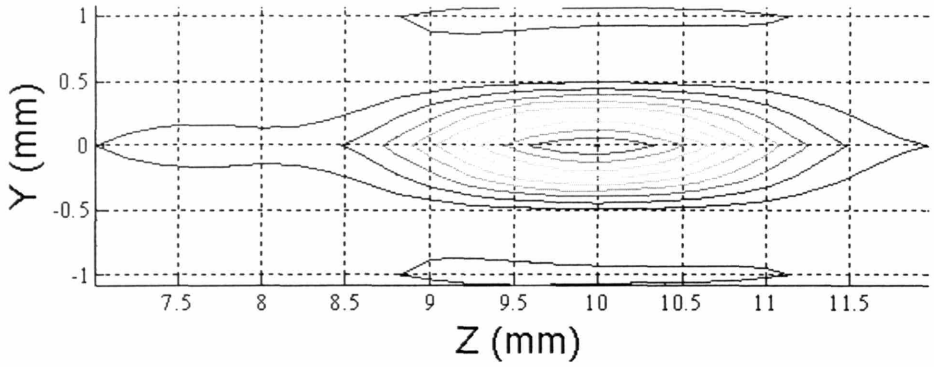

(B) Apodized 4 Phase (Infinite Resolution)

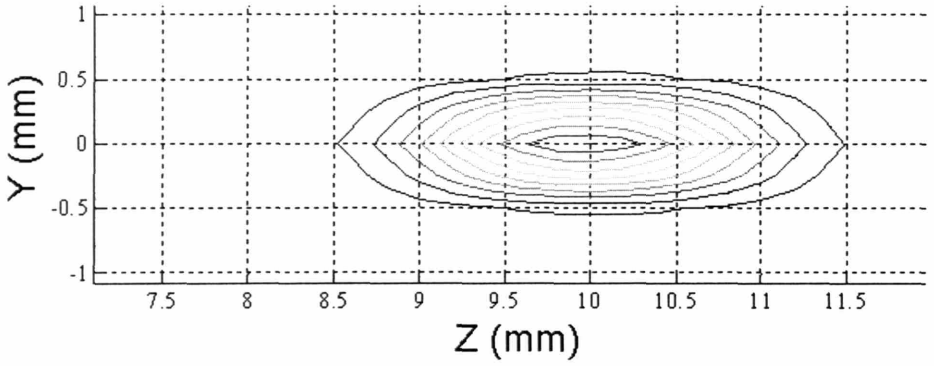

(C) Apodized 4 Phase (2 Step Quantization)

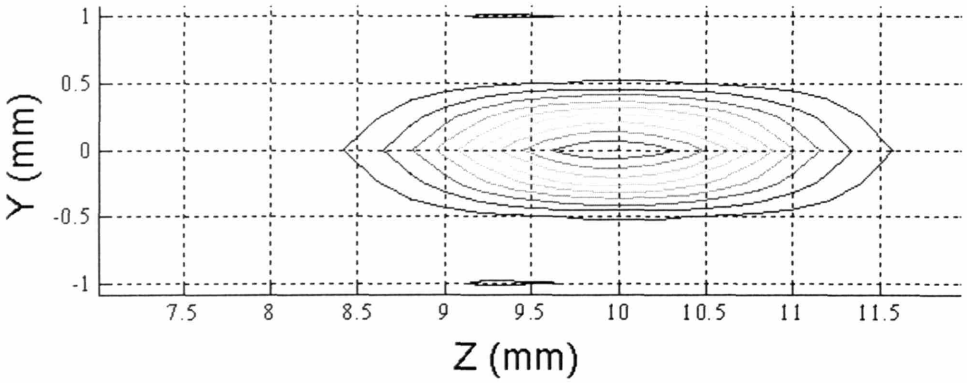

Figure 4.4 A diagram of the 10% contour plots for a 128x128 element array with the focus at (0,0,10) (A) The nonapodized 4 phase increment case (B) The infinite resolution apodized 4 phase increment case (C) The quantized apodization 4 phase case

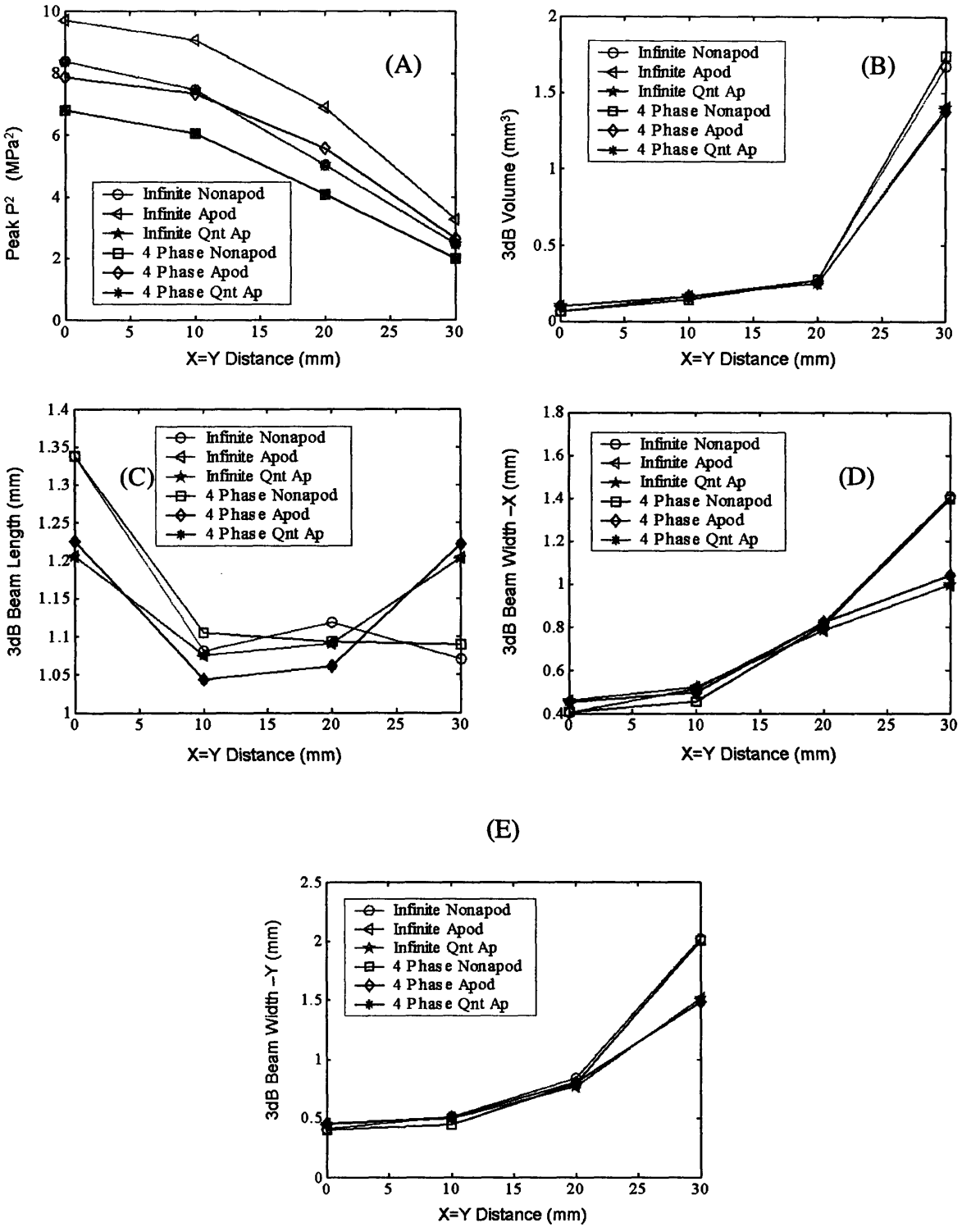

Figure 4.5 Graphs of the relationship focal distance from plane origin, apodization scheme and focal metrics. In the plane Z=10mm (A) between location and peak focal pressure squared, (B) between location and 3dB volume, (C) between location and 3dB beam length (D) between location and 3dB X beam width, and (E) between location and 3dB Y beam width

Figure 4.6 shows the impact of quantized apodization on the quantized phase configuration. In order to quantify the presence of the ridge, measurements were taken of the first and second axial peaks (numbered from the focus towards the array). Like other aspects of the focus, these peaks are related to the frequency and element spacing. Note that, in general, as the focus moves father away, the first and second peaks decrease in size.

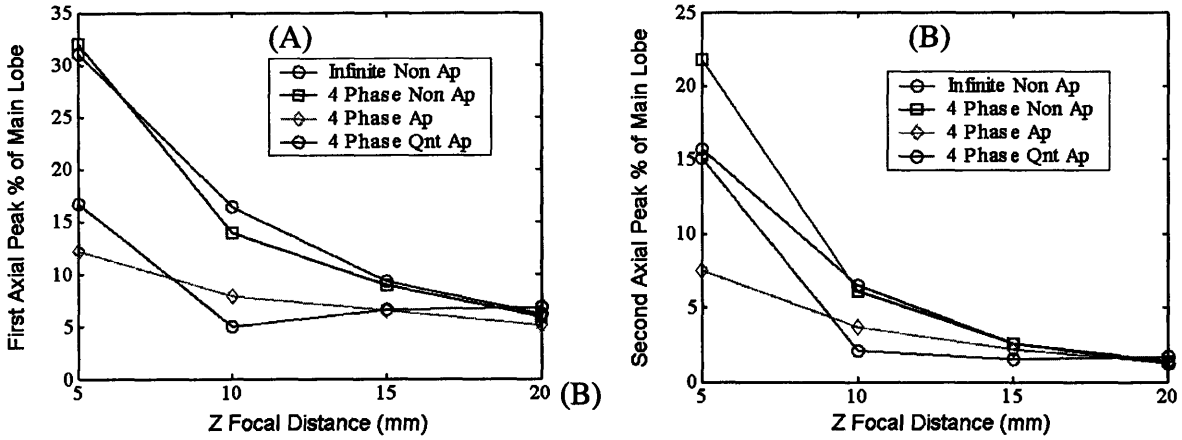

Figure 4.6 The graph of the axial peaks % of the main lobe, in relation to the focal distance from the array (A) First axial peak (B) Second axial peak

4.3.2 *Large Focal Distance Results*

As previously mentioned, in the quantized phase case, when the focus is sufficiently far from the array, there is increased grating lobe activity as shown in Figure 4.2. Figure 4.7 gives an alternate view of the lobes.

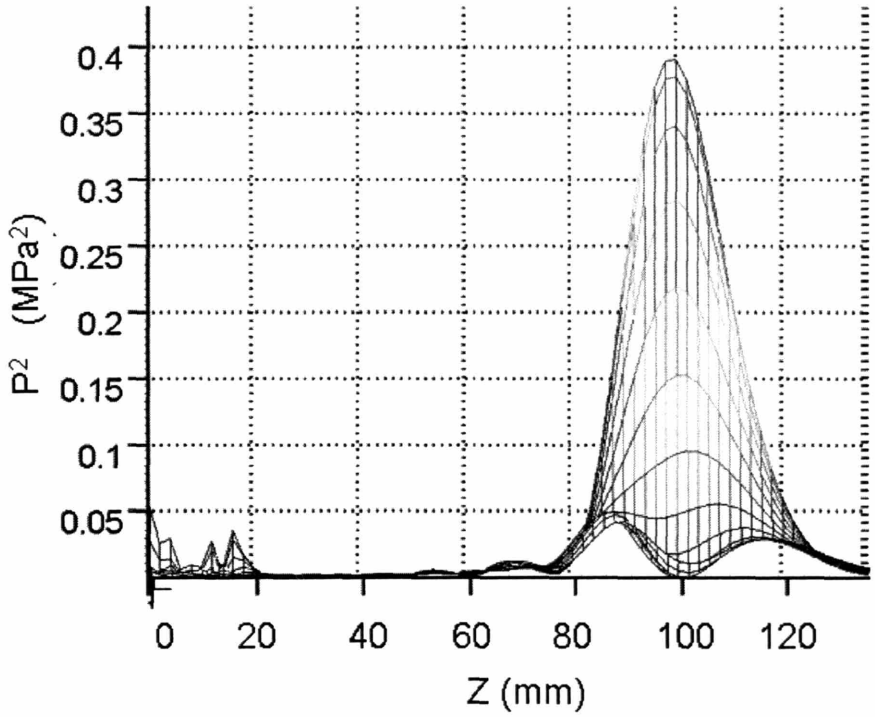

Figure: 4.7 A graph of the projection of the pressure square field for a 128x128 element array with the focus at (0,0,100). Note the presence of the large grating lobe near the transducer surface at Z = 0mm

Figure 4.8 describes the relationship between the grating lobes and a number of different focal and array characteristics. As one might expect the grating lobes are suppressed as the phase resolution is increased, as shown Figure 4.8 A. Similarly, as Figure 4.8C shows, the lobes also decrease as the array size increases. Note that for the averaged 4 phase increment case, when the array size is 64x64 elements, the grating lobe is actually larger that the main lobe. Also, of note is the fact that, in general, the grating lobes decrease in size as the focus is steered off axis, as illustrated in Figure 4.8B.

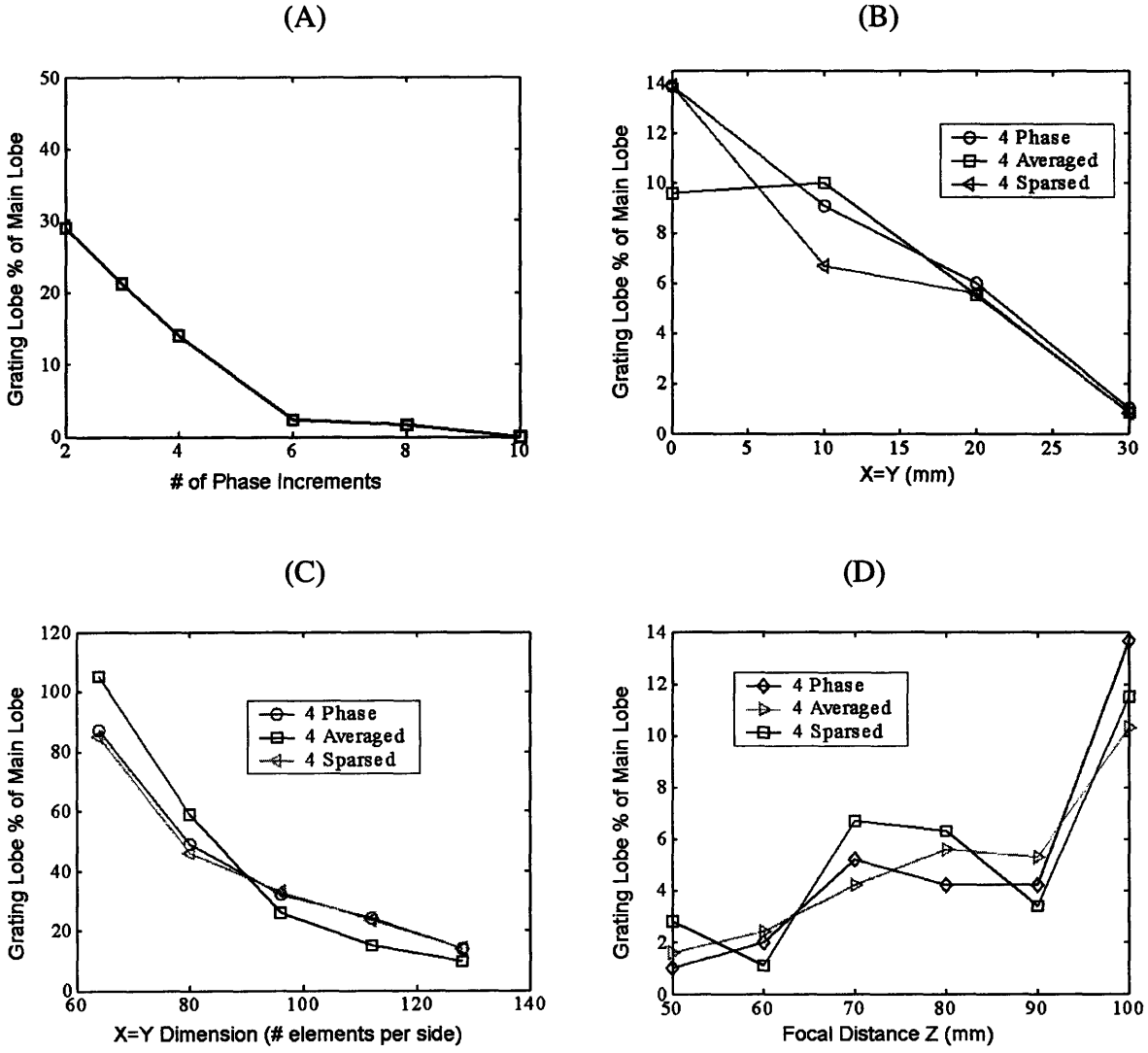

Figure 4.8 The relationship between the grating lobe % of the main lobe for various focal metrics: A) between # of Phase increment and grating lobe % of main lobe with focus at (0,0,100) B) between X=Y distance from the origin in the plane Z==100mm and grating lobe % of main lobe C) between array size and grating lobe % of main lobe D) between distance from the array along (0,0,Z) and grating lobe % of the main lobe

It should noted that in Figure 4.8B the averaged case crosses the other two configurations when the focus is moved from (0,0,30)mm to (10,10,30)mm. This crossover is possibly due to the way that the averaging protocol assigns the phase values (see section 3.2.3 for a description of the phase assignment process). Since phases are rank ordered and then divided, it is possible that some phases are reassigned in a way that causes the field to deviate significantly from the other techniques.

4.3.3 Energy Distribution Results

The metrics given in Figure 3.6 and field plots in Figures 2.4-2.7 and 3.3-3.5, show that the general shape of the focus is the same in both the infinite and 4 phase resolution cases. In addition we know that overall the energy in both case has to remain the same. Figure 4.9 gives the plots for the xy plane very close the transducer surface for the two phase assignments schemes. Note that in the 4 phase case there is considerable energy near the periphery of the field, relative to the infinite configuration. Figure 4.10 shows the xy field for a plane near the focus and relatively far from the array. Note that the shapes are similar, except that the quantized arrangement has a lower peak and slightly more energy in the areas away from the focus.

(A)

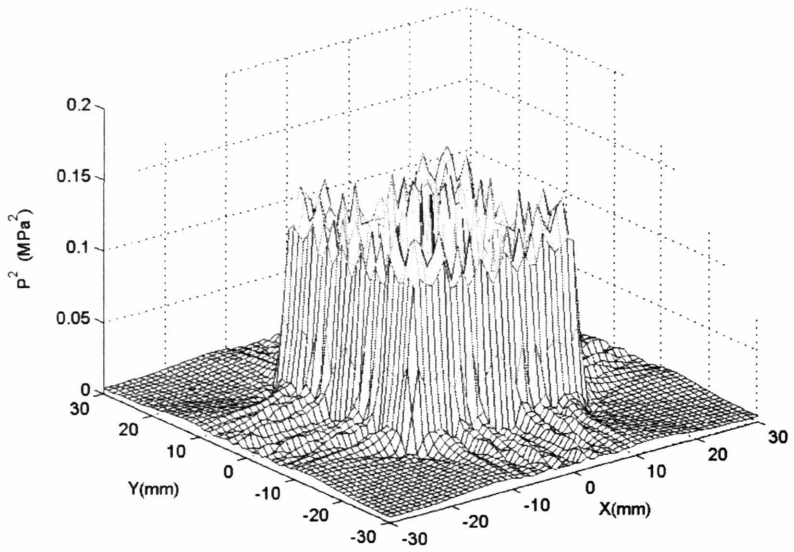

(B)

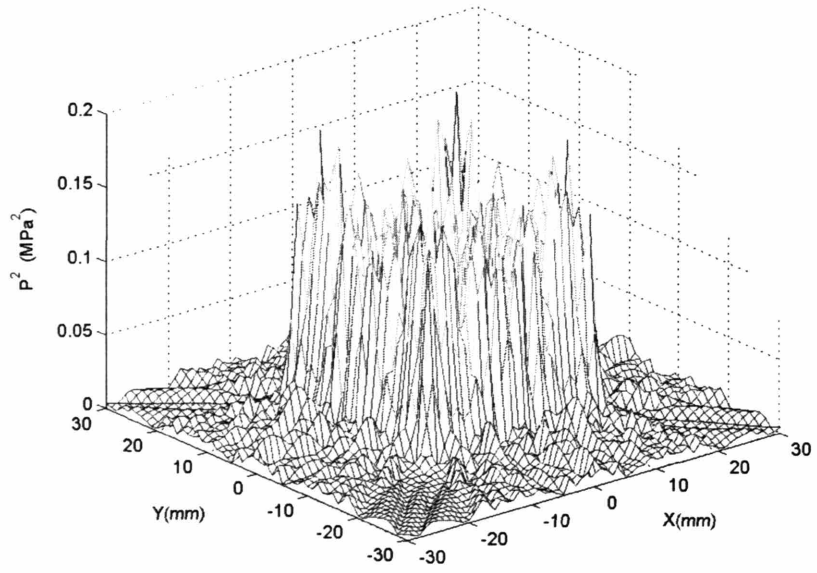

Figure 4.9 The pressure square field in the xy planes for Z =1mm. A) for the infinite phase resolution case B) for 4 phase increments

(A)

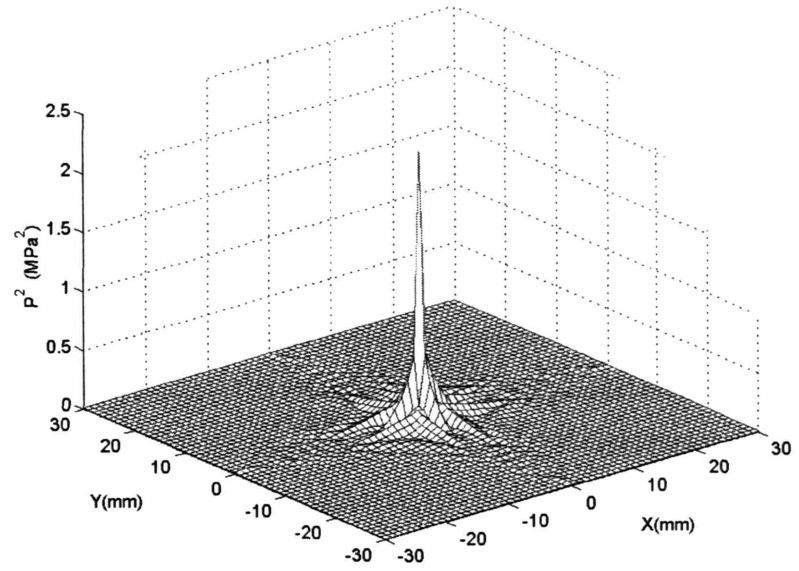

(B)

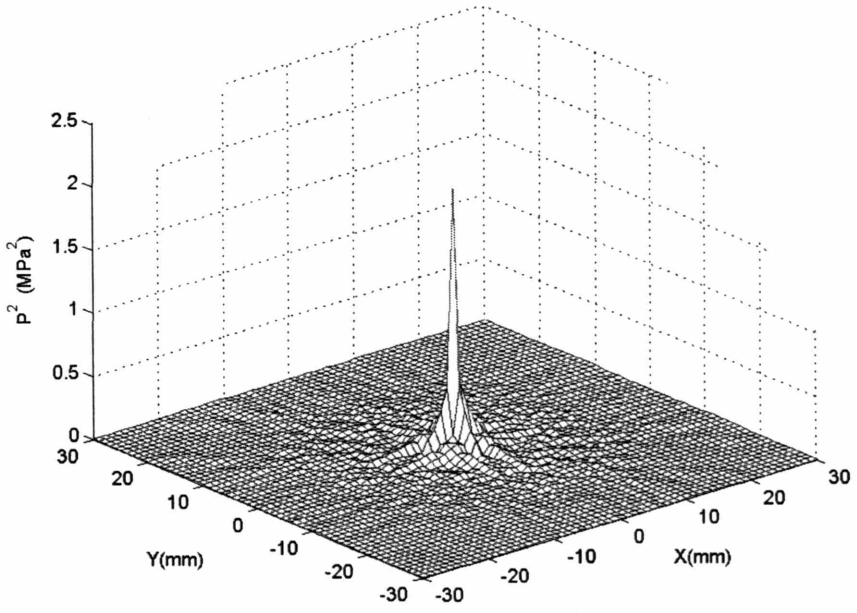

Figure 4.10 The pressure square field in the xy planes for Z =9.9mm. A) for the infinite phase resolution case B) for 4 phase increments

4.4 Discussion and Conclusions

In this and the previous chapter, we have attempted to show that quantizing the phase resolution available at the input of an ultrasound system significantly reduces the number of input lines needed to drive a high density array. Moreover, evidence has been offered which suggests that the overall focal quality and beam steering capability make this technique a viable option for use in selectively delivering energy to a specific location. However, as previously mentioned, there are a number of characteristics unique to phased array designs and quantized phase implementations that require additional methods for increasing their effectiveness as a treatment option. Specifically, in the fields close to and far from the array surface, there is extra-focal constructive interference that might present problems during the actual implementation of a quantized phase design.

Figures 4.3 and 4.4 show that apodizing the power to each element of an array is effective in suppressing the pressure ridge that forms when the focus is in the very near field. Figure 4.5 suggests that with even as few as 2 levels, significant benefit can be gained from this reduction in resolution. Of note is the fact that the 3dB volume is nearly the same for all apodizing schemes, which suggests that apodization affects mainly the secondary lobes. As mentioned previously, this technique has been used in diagnostic arenas for a number of years to shape side and grating lobes (Eaton, Melen, & Meindl 1980;Karrer et al. 1980a), but, until now, has not been investigated for therapeutic applications. Overall, with minimal impact on the reduction of input lines, quantized apodization shows promise for extending the range of beam steering to the very near field (Note, the 2 level apodization scheme, doubles the number of input lines for the 4 phase case, however for a 128x128 element array, this still would only require 35 + 4 = 37 incoming wires).

While the pressure ridge characteristics of phase arrays are noticeable and may have an impact on the pressure field, the grating lobes created by phase quantization impose a more severe limitation on the actual implementation of the concept. As Figure 4.5 shows, while the 3dB characteristics of the focus are sufficient for therapeutic

purposes, the grating lobes would very likely cause significant heating near the skin. However, Figure 4.8A shows that adding an additional two levels of resolution, would reduce the sidelobes to less than 3% of the main lobe. This would result in a slight increase in the number of input lines. However, as alluded to in Chapter 2, 6 is a less common value for integrated circuit component packages. As such an actual implementation would likely use an 8 increment configuration. As will be discussed later in Chapter 6, this might pose problems, since the largest amount of active real estate on the PCB is used by the phase selection switches themselves (this concern also arises when quantized apodization is introduced into the system).

One additional point that should be made relates to the sparsing technique. Figure 4.8 gives the impact on the grating lobes for a number of different metrics. It should be noted that the values given for the sparsed configuration represent only one of many possible results, i.e. because the sparsing technique randomly removes elements, the active elements in each simulation vary, causing the results to change slightly.

While the 4 phase increment case does suffer from a slight reduction in pressure amplitude, overall the focal quality rivals that of the infinite phase resolution case. As Figures 4.9 and 4.10 demonstrate, the energy that is lost is dispersed to locations far outside of the focal region. This fact can be deduced by the increased difference between the sums of the pressure square fields for the two protocols. Because the energy is distributed in this way, it is diffuse, and would not contribute significantly to heating, if used in an actual system. As such, the 4 phase case has the added benefit of being able to recover much of the lost focal amplitude by simply increasing the power to the array.

As such, for a 128x128 element (58mm x 58mm) array with 0.45mm inter-element spacings, 4 input phase increments, and 2 input power levels, effective focusing can be achieved over an x and y range of 60mm (X and Y = -30mm to 30mm) and a z range of 80mm (Z= 10mm to 90mm), for a total theoretical treatment volume of 288000mm^3 or 288cm^3.

5 Quantized Input Phase Hardware Implementation

5.1 Introduction

As discussed in the previous chapters, in order to achieve greater focal control and beam steering capabilities, inter-element spacing would need to be reduced to $\lambda/2$. For 2D arrays operating at therapeutic frequencies from 0.5 to 4 MHz, this constraint would require that elements size be reduced to 0.19 to 1.5mm on each side. To deliver enough power for use in thermal ablation, whether by cavitation or simple heating, transducer arrays would need to be composed of thousands of element. Research has shown that phase array techniques offer the greatest flexibility and promise for treating large tissue volumes (Daum & Hynynen 1999a;Fjield et al. 1997;Hynynen, McDannold, & Jolesz 1999). Currently there are very few systems capable of driving more than a few hundred elements. Even in these advanced systems, there are a number of issues related to fabrication difficulty and cost that have prevented higher density systems from being developed, based on their designs. In this chapter, we examine one implementation of the quantized input phase concept. The system was designed, built and evaluated, with the intention of being able to scale it to 10000 or more channels. Making use of a novel switching scheme, flexible circuit technology and phase assignment protocol, this configuration attempts to offer solutions to many of the problems that have prevented focused ultrasound (FUS) systems from gaining wider use as surgical alternatives.

5.2 Methods

5.2.1 System Design Considerations

The overall goal was to design a system that is easily scalable, simple to build, and capable of delivering an appreciable amount of power. Figure 5.1 shows a diagram of the overall High Density Array Addressing and Driving System (HDAADS). First, the required phases for a given focus are calculated by a program written in MATLAB. This information is then converted to a digital data stream, using a custom LabVIEW script, which then passes the data to the selection hardware.

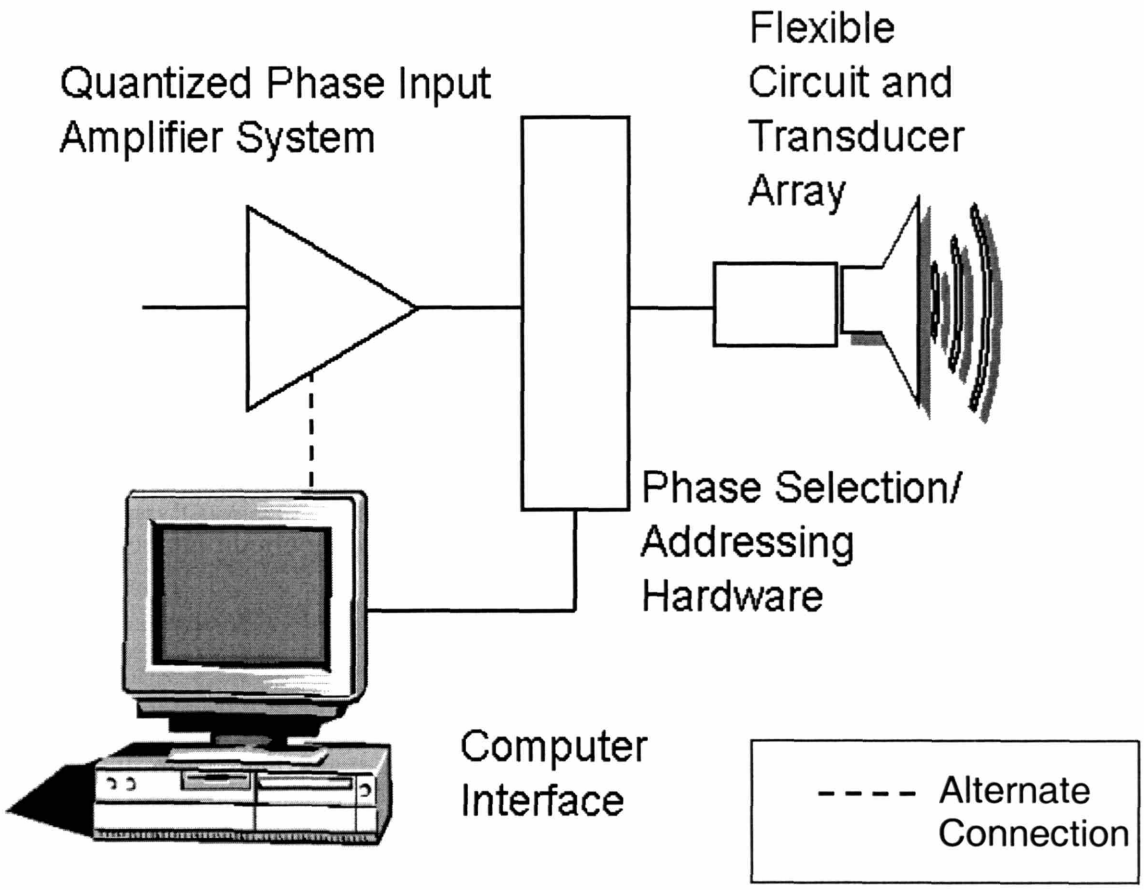

Figure 5.1 A block diagram of High Density Array Addressing and Driving System (HDAADS)

The 4 input phase increments are first passed through their respective 4 high power operational amplifier circuits, and then selected based the data from the PC. The analog driving signals from the input bus are then distributed to the individual elements, which have been connected to the system via a flexible circuit jumper.

5.2.1 Flexible Circuit Jumper

5.2.2.1 Motivation for the Use of Flexible Circuits

One of the limiting factors which has slowed the move towards higher density arrays is the need to form interconnects to each of the elements. Traditionally, connections have been made by soldering individual wires to pre-constructed arrays of elements. This method is sufficient for smaller arrays with large or widely spaced elements. This is especially appropriate for curved arrays that have been specially shaped to geometrically place the focus at a specific location. With the advent of phased array technology and the ability to obtain good focal precision from planar arrays, the requirement of being able to connect to rounded surfaces is no longer a concern. Moreover, with the benefits of $\lambda/2$ spacing driving the move towards higher spatial element density, the soldering of single, loose wires becomes prohibitively difficult. One solution, which is explored in this study, is the use of a flexible circuit jumper to connect the transducer array to the driving circuitry.

Figure 5.2 shows a block diagram of the interface between a transducer array and its driving system. The assembly works as the input signal comes from the amplifier (via the phase selection system to be discussed later) through a co-axial wire bundle, which is adapted to mate with a flexible circuit, which in turn passes the power to the array.

A 128-element cylindrically curved array with a 40mm radius of curvature, element length = 30mm and width = $\lambda/2$ = 0.67mm, and resonant frequency = 1.1MHz has been designed in our laboratory, and constructed by Imasonic (Imasonic 2725 BXXX). Figure 5.3 shows a diagram of the array. Note that each of the elts or pads on the back of the array connects to a transducer on the opposite side of the device. Using conventional techniques would call for soldering a micro coaxial cable directly to the array (micro-coaxial wire is used for shielding purposes). The wire's ground and signals sections would first be separated, then connected to their respective pads. From the diagram, it can be seen that soldering to each of the pads might prove difficult, due to the

relative closeness of each (<0.7mm), and the need to keep the wires separated. While making connections could be facilitated by the use of a microscope, the problem is further complicated by the need to minimize the space taken up by the wire assembly. If this array were operating at a higher frequency, the $\lambda/2$ requirement would move the elements even closer together, further worsening the problem.

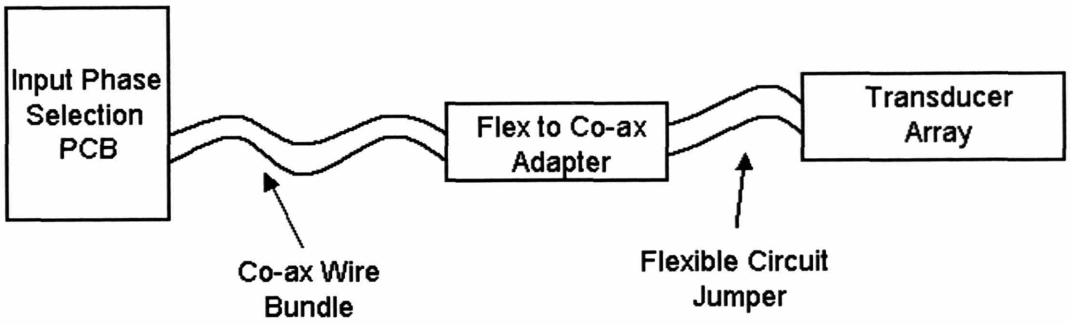

Figure 5.2 A block diagram of the flexible circuit interface between a 128-element array and an amplifier system

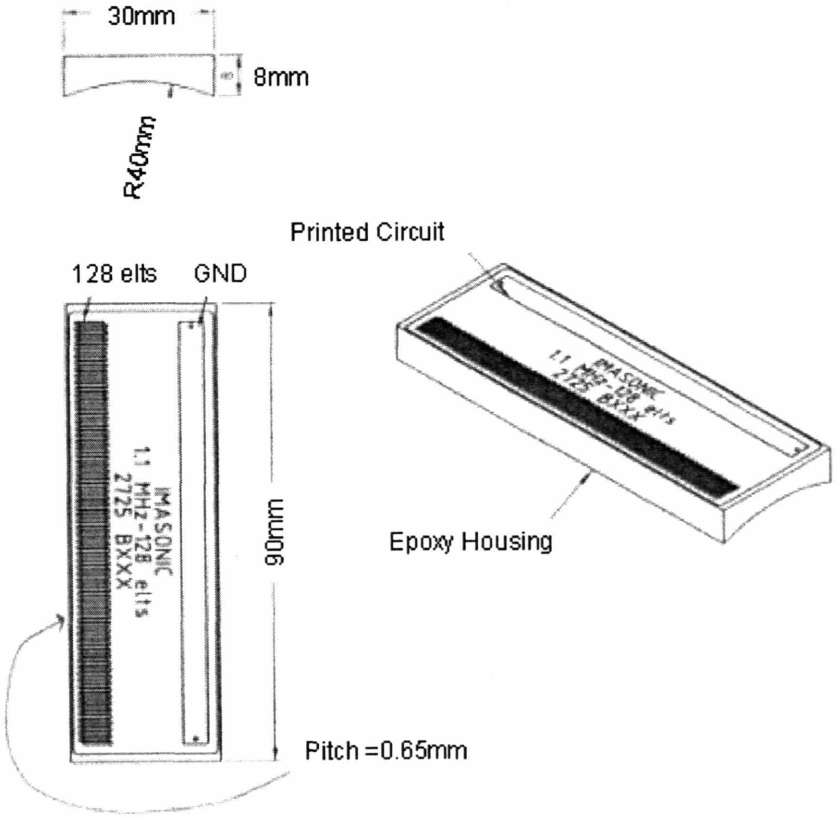

Figure 5.3 A diagram of the Imasonic 2725 BXXX 128-element 1.1MHz linear array (diagram adapted courtesy of Imasonic)

5.2.2.2 Flexible Circuit Design and Assembly

A flexible (flex) circuit is one solution, this study offers, to the problem of connecting to a large number of closely packed pads. There are a number of characteristics which make the flexible circuit a better choice for connecting to a linear array: 1) use can be made of common printed circuit board (PCB) design tools to tailor the circuit to mate with the small and evenly distributed pads on the array case, 2) the flex circuit can be turned or twisted, thus maintaining some of the properties of a wire assembly, and 3) the flex circuit can be made to be compact, making it well suited for use in the limited space available on the back of the array.

A flexible circuit, as its name implies is an electronic device, which can bent without altering its functionality. Traditional PCB's are usually composed of layers of FR4, a rigid base material, with copper or some other conductor used to provide signal paths to the various components or connectors that interface with the board. The flexible circuit used here is similarly constructed, except that instead of using FR4 as a substrate, polyimide is employed. A polymer, polyimide provides a stable base material without the rigidity found in normal PCBs. While, polyimide itself is highly flexible, the copper or other conductors used to make the circuit usually are not as supple. Thus, the extent to which the circuit can be deformed is strongly tied to its design and application. As previously mentioned, because a flex circuit is essentially a regular PCB with a polyimide base, it can be designed and fabricated using most commonly available design packages. In this case Protel 2004 (produced by Altium, Frenchs Forest, Australia), being run on a Windows based PC with a dual 400MHz Pentium III processor was used to design our flex circuit.

For versatility of use, a 1 ounce copper process with a minimum trace width of 0.254mm was chosen, enabling each channel to carry 750mA. These values allow the circuit to be used not only with the driving system described in section 5.2.1, but also with other amplifier systems in our laboratory. Initial design considerations centered on connecting the flex circuit to the array pad. Figure 5.4 illustrates an 8-channel version of the method used to interface with the case: Using Protel 2004, the mating pads could be

precisely designed to fit with transducer pads. Most of the area where the actual connections were to be made was left insulation-free. The tips of the traces remained attached to the insulation for the purpose of keeping the connecting "fingers" aligned. Both the array pads and the exposed copper traces on the flex circuit were tinned (pre-coated with solder) to facilitate easier connection.

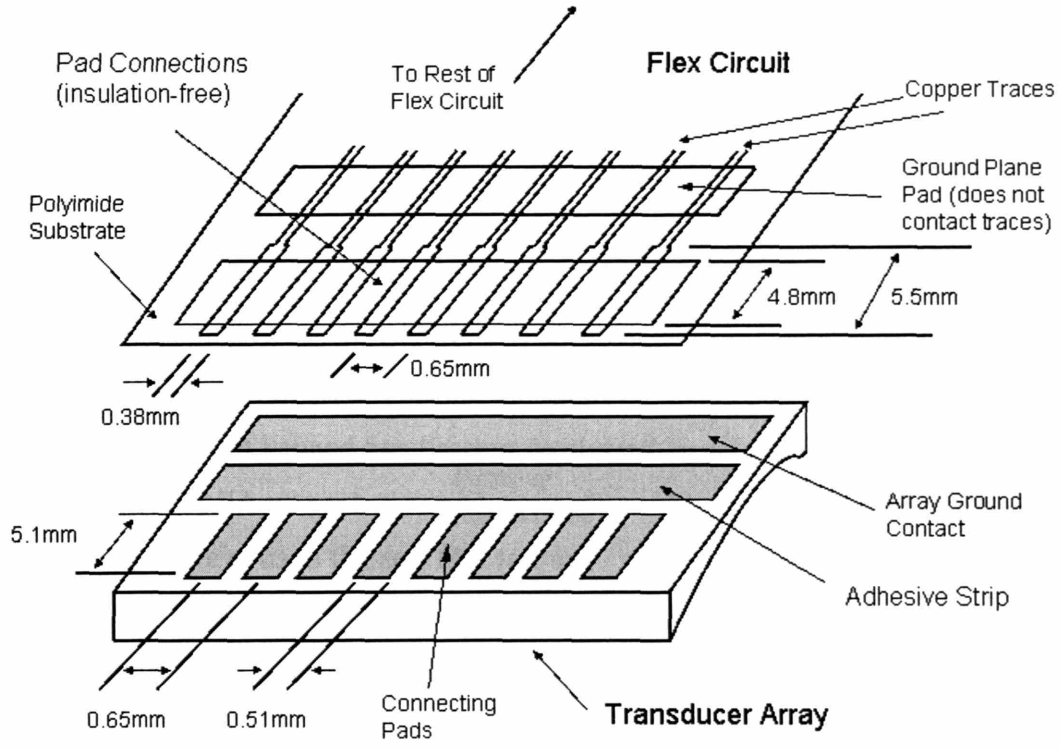

Figure 5.4 A diagram of the interface between an 8-element transducer array and a flex circuit. The connection interface for the 128-element array is identical, except for the increased number of elements.

The traces were aligned with the pad and lowered onto the array case, and were held in place by a 3M double-sided adhesive strip (3M Scotch 467MP). Because the traces and pads had been tinned, they were simply touched briefly with a soldering iron to bond them to their respective pads. The traces that were bonded to the array pads were shielded by using a ground plane, and isolated by using 0.254mm inter-trace spacing to minimize cross-talk among channels.

The 128-element array used in this study was designed, among other applications, for intracavity use, i.e. inside of the body. This fact imposes severe size constraints, since, for example, prostate treatment is most effectively accomplished by passing the transducer array through the anus and into a more optimal position for sonication. As such, the overall axial cross-section of the flex/array assembly had to be minimized. To accomplish this task, the flex circuit had to be folded. To further reduce the profile, the 128 traces were divided into groups of 14 or 15 lines and routed through strips that would terminate in zero insertion force tabs at the tip of the flex circuit, i.e. the traces leading from the main connecting pad were split into smaller groups that would eventually mate with smaller connectors on the other end of the flex circuit. Figure 5.5 shows a 21-channel, three layer, twofold version of the flex circuit and the folding process (the actual jumper had 9 layers and 8 folds). Figure 5.6 shows the flex circuit just before the last fold was made. The other layers have been pressed and bonded to one another using the previously mentioned 3M adhesive. This bonding was done by All Flex Inc (Northfield, MN), who also fabricated the circuit. The last fold was left open to allow soldering of the pads, which after completed, was closed. It should be noted that the length of the layers is staggered, which was done to minimize the axial profile. The motivation for this will be explained in the next section.

The widest total width, and length of the circuit were 533mm and 242mm respectively, with 8.9mm wide signal strips being staggered by 20mm.

(A)

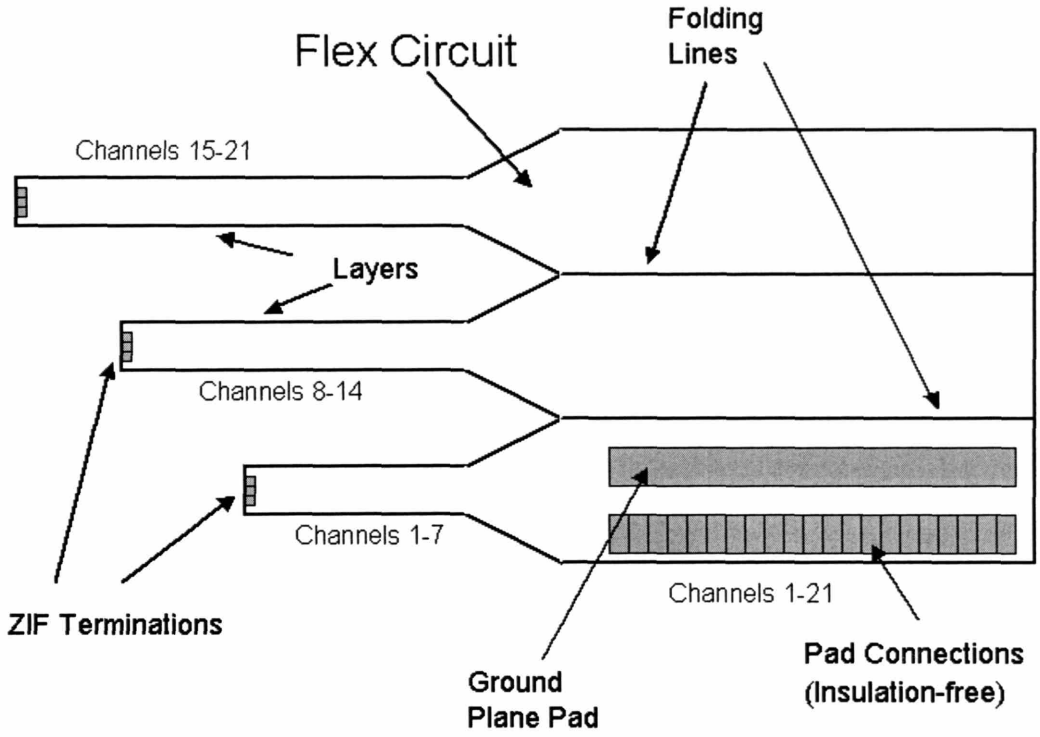

(B)

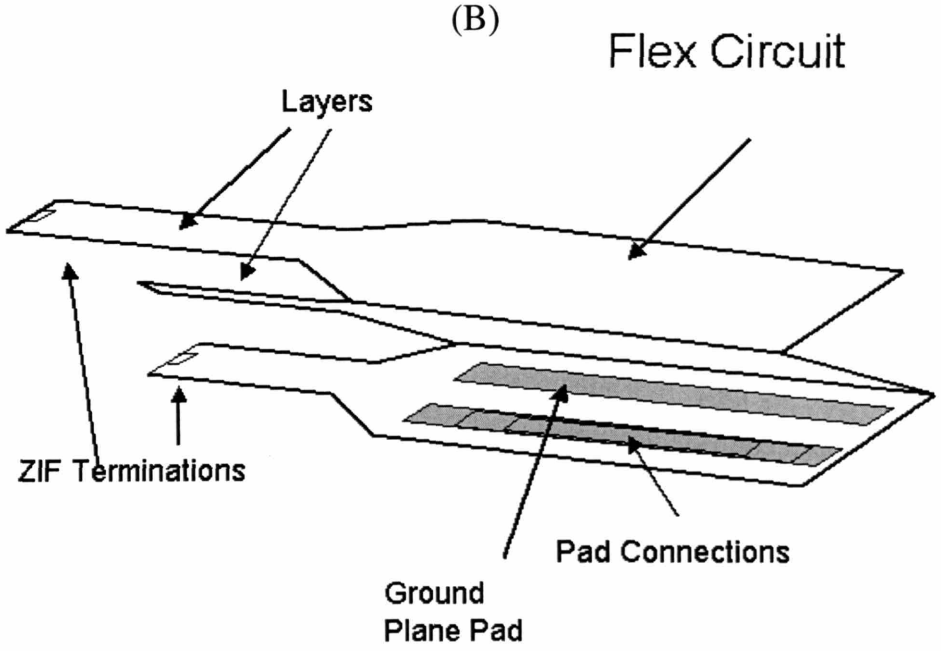

Figure 5.5 A diagram of the folding process for a flexible circuit, used to reduce the axial profile. (A) Unfolded circuit (B) Partially folded circuit. Note the actual circuit had 9 layers

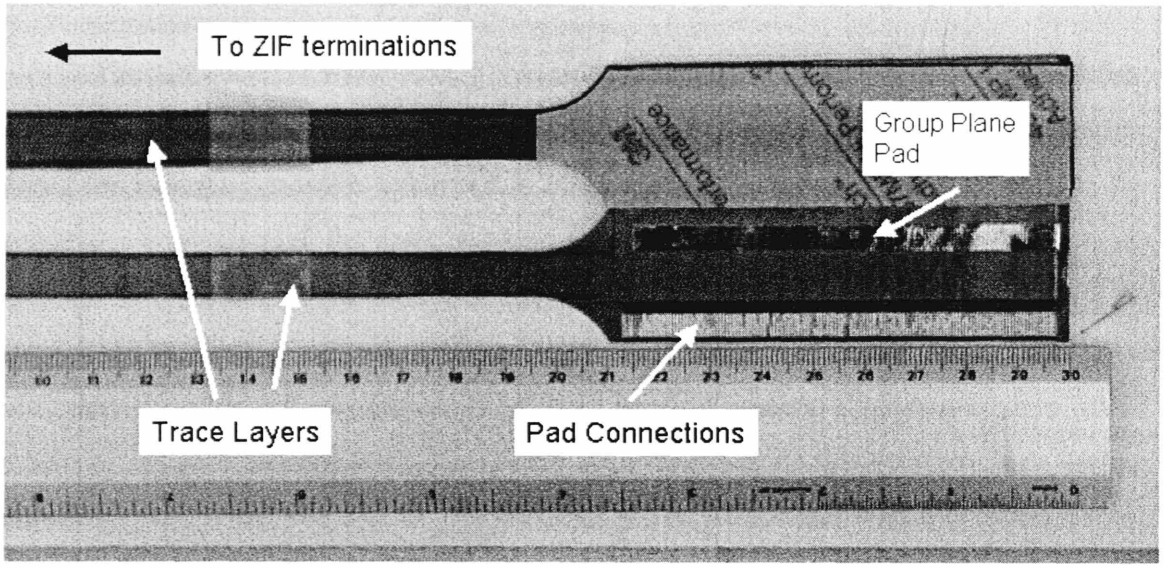

Figure 5.6 A photograph of the flex circuit just prior to connection to the array and final fold

5.2.2.3 *Flex to Co-axial Adaptation*

Ideally the flex circuit would have been fabricated such that the traces could interface directly with the driving circuitry. However the connecting lines would have to be more that 2 meters long, making the flex circuit prohibitively expensive to construct. As such, the ZIF ends of the flex circuit "layers" were adapted to groups of 14 and 15 micro co-axial cables via a Molex 0528931690 connector mounted on 15mm x 13mm mini PCBs. This particular part was selected for its small size and ability to pass more than 400mA of current per terminal. One side of the board contained the Molex connector and on the other the pads to which the coaxial wires were soldered. Once all of the wires had been connected and the flex circuit inserted, the assembly was stabilized by an acrylic case machined using a Denford CNC Microrouter. As mentioned in the previous section, the layers were staggered to reduce the axial profile. Because the strips were of different lengths, the Molex connectors did not rest directly on top of one another when connected. The thickness of the entire assembly was only a little more than the sum of one PCB/connector and the contributions from all of the flex layers. Figure 5.7 shows the Molex 0528931690 with accompanying PCB.

(A)

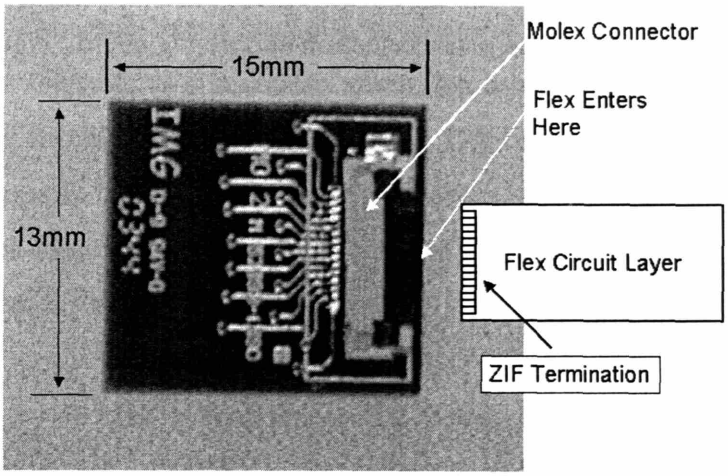

(B)

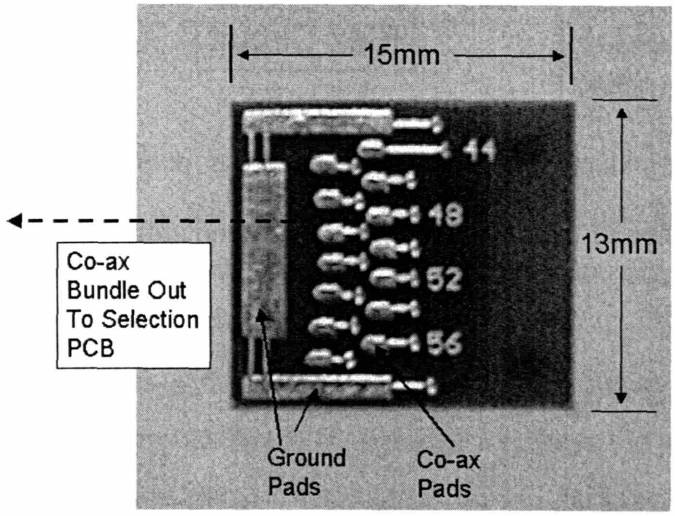

Figure 5.7 A photograph of a mini PCB used to connect the flex circuit to a coaxial cable assembly (A) to Top view of the PCB (B) the Bottom view

The opposite ends of the micro co-axial wires were terminated in two 200 pin DL5-260P connectors (each of the 128 signal lines had an accompanying ground, which gives 256 lines, thus the need for two connectors). These connectors would be joined with mating DL260R receptors, located on the phase selection addressing board. Figure 5.8 shows the completed flex circuit assembly.

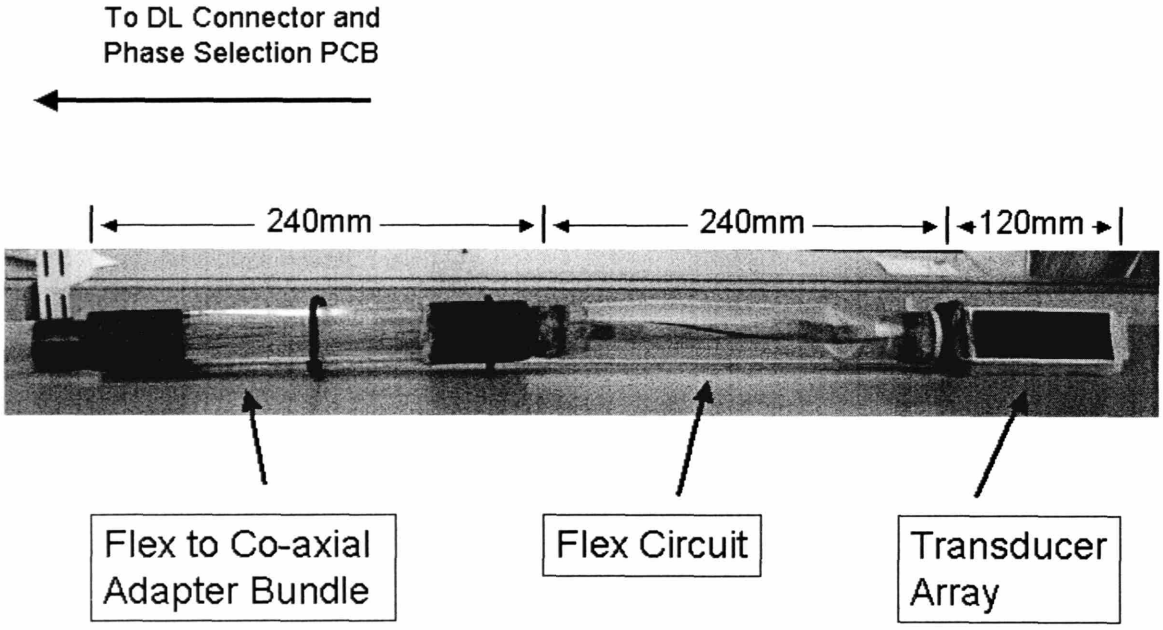

Figure 5.8 A photograph of the completed flex circuit and array assembly. Note, the flex circuit is encased in translucent rubber tubing (Cole-Parmer Instrument Company) for water proofing purposes

5.2.3 128-Chanel Phase Selection PCB

The core of the quantized phase concept was implemented via a 128-channel PCB. The design called for a simple selection scheme, which chooses one of a group of phases, which is then passed to individual elements in the transducer array. The selected phase is based on an assignment protocol, or phase window. In this case a 4-phase configuration was selected, as simulations show that this provided good focal precision and beam steering capability (Chapters 2 to 4). A 128-channel array was chosen for this section, since one was readily available in our laboratory and contained a sufficiently large number of elements to illustrate the benefits of the concept, yet was small enough to be constructed from discrete components.

The primary factors considered in the design were compactness and power capabilities of the board. As such, the size and number of the components were important. Initial designs used multiplexers to accomplish the phase selection. However the power limitations of existing components prevented them from being used. Most multiplexers were current limited to tens of mA's and those with larger currents, were voltage limited. The final design settled on a multi-switch chip, with specifications that were compatible with driving high impedance loads. Figure 5.9 shows the basic design for the selection scheme.

The ADG452, which is a quad digital switch package with positive "on" capabilities (Analog Devices Inc) was selected for its relatively high maximum voltage swing, 48Vpp (17Vrms) and continuous current limit of 100mA, which yields a maximum output power of 1.7W. With a relatively high voltage capability (others were limited to between 1 and 4Vrms, this switch was well suited for the small higher impedance elements likely to be found in high-density arrays. In addition, being housed inside a 16-pin small outline integrated circuit (SOIC 16) package, made it a good match for our size constraints (Note: after the phase selection PCB fabrication had begun, the ADG452 became available in a 16-pin thin shrink small outline package (TSSOP 16), which is approximately 48% smaller than the SOIC 16; future designs might consider using this part instead). The other components were common digital parts.

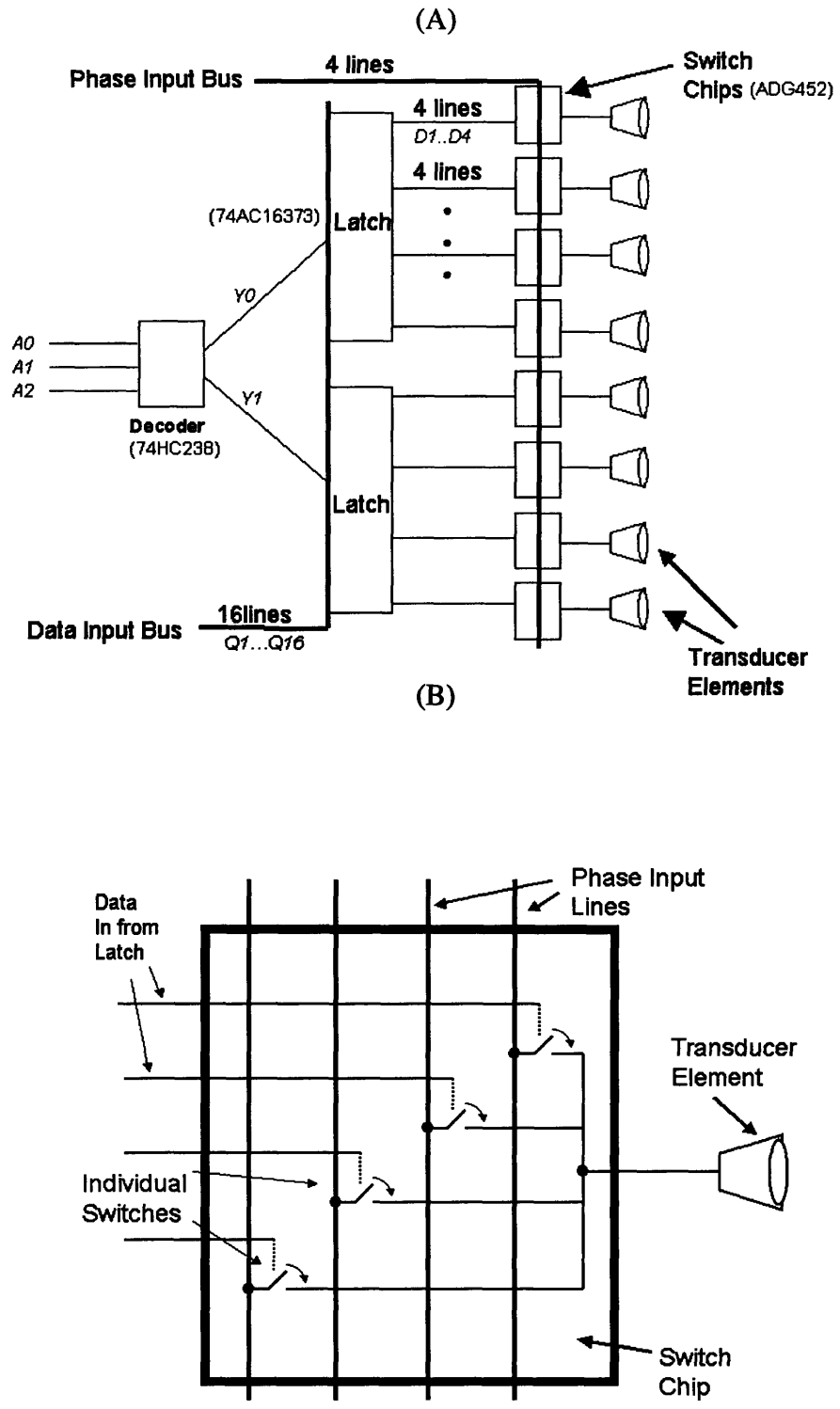

Figure 5.9 (A) A block diagram of the HDAADS phase selection circuit. Note: labels in *italics* represent chip address/pin names (B) A close up of the selection switch chip

The SN74AHC16373DGGR is a popular general-purpose latch and the CD74HC238M is a non-inverting version of the CD74HC138M, which is often used in decoding applications. Its non-inverting configuration was chosen to match with latch enable polarity of the SN74AHC16373DGGR which is high when receiving data, and low when latched.

The control signal is generated using a custom program written in MATLAB, which is converted to a digital 24-bit word by a LabVIEW script. The phase selection data is placed on the data input bus, which is accessible by all of the latches. The selected latch receives the data, while all other are in a latched state. The control signal uses the decoders to determine which latch will receive the data. The phase selection information is serially loaded into each latch, which minimizes the number of control lines. After all of the latches have acquired their data, the information is then passed to the switches, which select the appropriate phase, based on the location of the focus.

In order to verify the viability of the topology, before building the full 128-element design, a smaller 8-channel version was constructed. The schematic for 8-channel PCB is identical to that given in Figure 5.9, except for the number of elements. Figures 5.10 and 5.11 show the completed 8-channel and 128-channel boards.

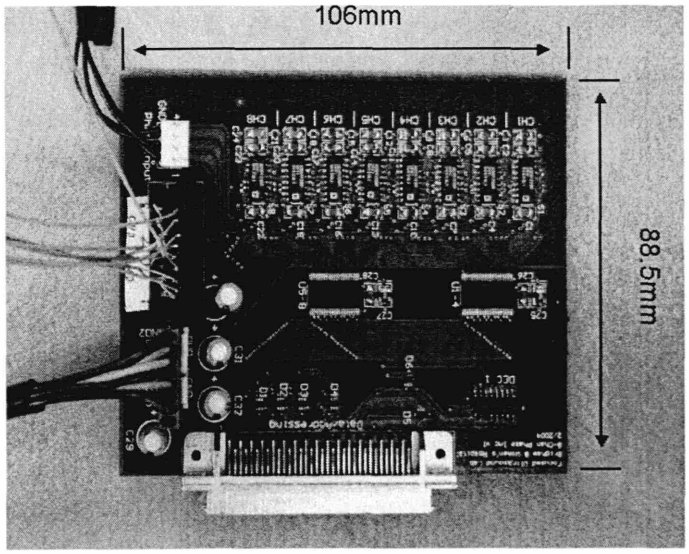

Figure 5.10 A photograph of the 8-channel HDAADS phase selection prototype circuit

(A)

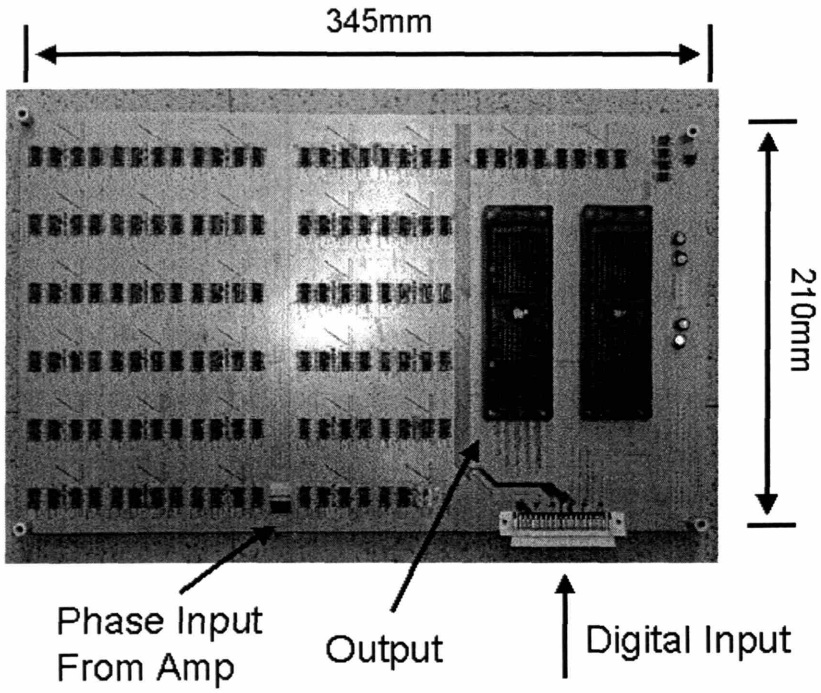

(B)

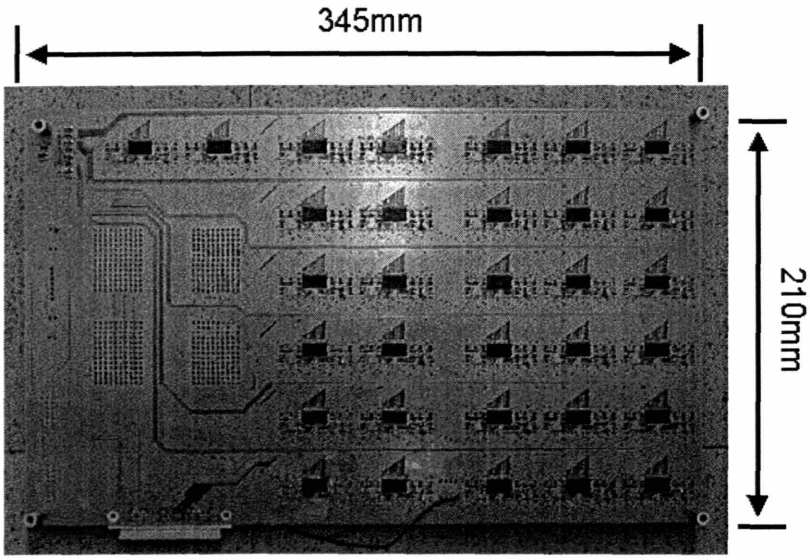

Figure 11 A photograph of the 128-channel HDAADS phase selection circuit (A) Top View (B) Bottom View

5.2.4 *Input Phase Amplifier*

The four phases used by the selection section of the system were generated by a synchronized bank of signal generators (Stanford Research System Model DS345). Each of the four signals was amplified using an operational amplifier (op-amp) wired in an inverting configuration. Figure 5.12 shows the amplifier circuit.

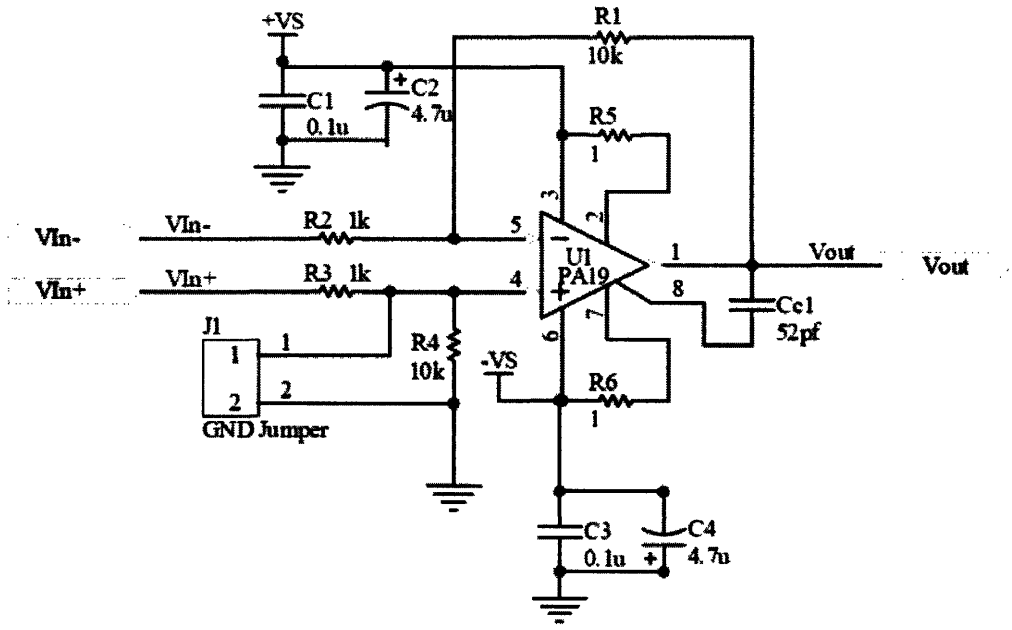

Figure 5.12 A schematic of the HDAADS phase input amplifier.

Note that the presence of the GND jumper enables the circuit to be converted to a differential op-amp amplifier, which could be used for subsequent experiments. As observed by Sokka, who first implemented this kind of topology for therapeutic ultrasound applications, because this is not a matched configuration, the power transfer efficiency is not optimized (S. Sokka, MIT PhD dissertation, 2003). However, there is tremendous benefit in that this design eliminates the need for matching to each channel, by using the op-amp in a feedback configuration to actively adjust for changes in the load. This allows for changes in the number of times a particular phase is used, as the focus is steered, or the number of elements in the array changes.

The core of the circuit is the PA19 power operational amplifier (Apex Microtechnology Corp), which has a maximum output voltage of 80Vpp, and a maximum continuous current limit of 5A. In order to maintain the stability of the amplifier, low temperature dependence capacitors and ultra low inductance metal film resistors were chosen. As the PA19 is very sensitive to stray inductances, inter-component spacing was also minimized to ensure stability of the circuit. To minimize power consumption, the supply rails were chosen to be +15V and –15V. To cool the opamp during operation, a combination of the TW03 thermal washer and HS02 sink were used (both made by Apex Microtechnology Corp). The finished board is shown in Figure 5.13.

For each of the four channels, the components and power supply voltages were initially selected to give a closed loop gain of 10, output voltage of 26Vpp and output current of 2A. These values minimize the possibility of exceeding the tolerances of the ADG452 switches, which carry out the phase selection on the adjoining PCB. It should be noted that the input amplifier board was made separate from the selection PCB to allow for the possibility of driving additional boards, if needed. Figure 5.14 shows the overall completed HDAADS.

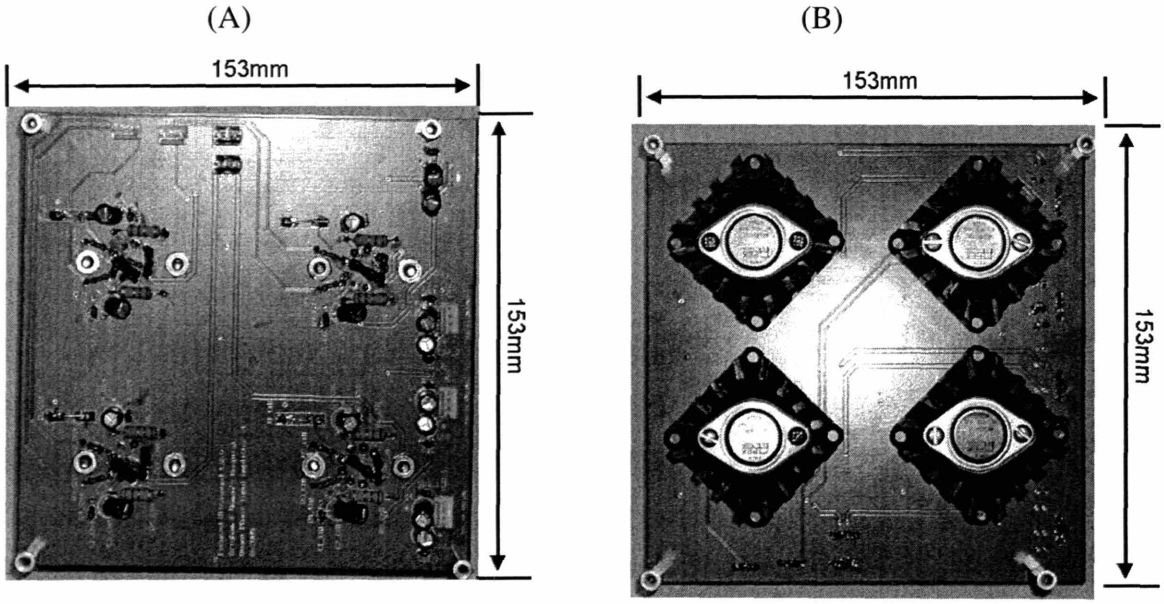

Figure 5.13 A photograph of the HDAADS input phase amplifier PCB. (A) Top View (B) Bottom View

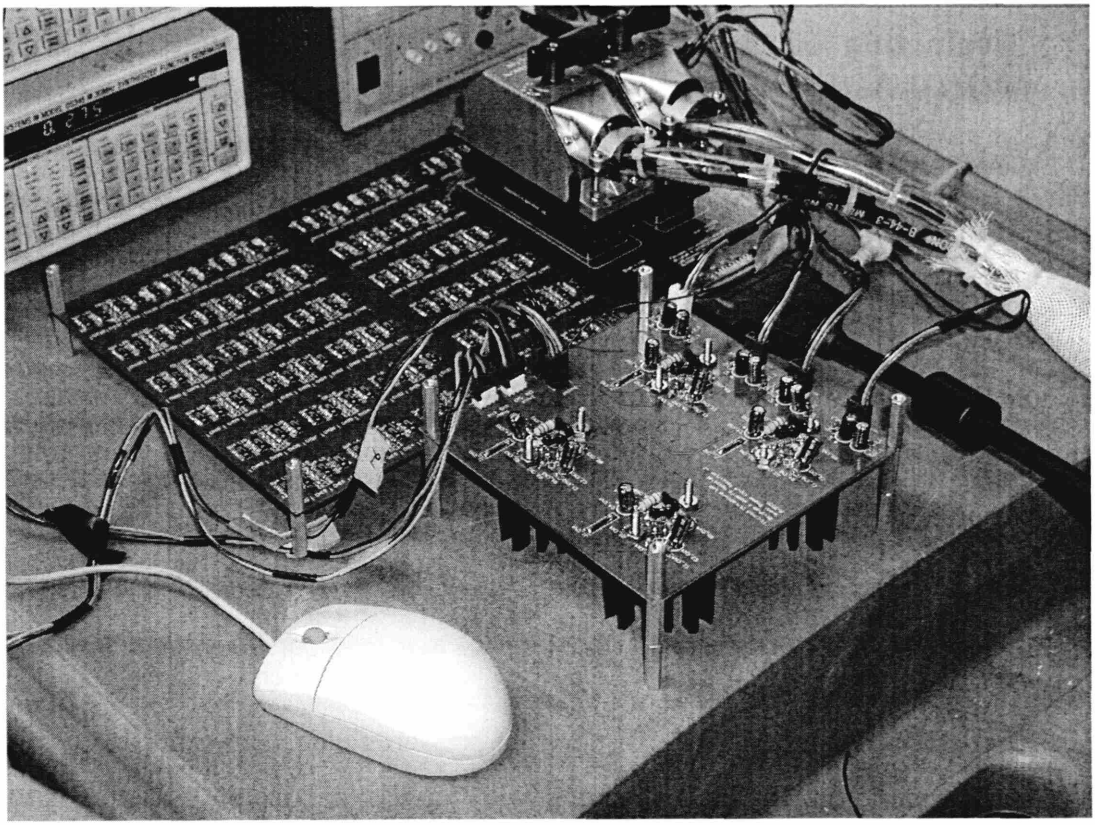

Figure 5.14 A photograph of the overall HDAADS

6 Evaluation of the High-density Array Addressing and Driving System (HDAADS)

6.1 Introduction

In this chapter we assess the viability of constructing an addressing and driving system capable of being scaled to thousands of channels. In the previous section we introduced the motivations and design for such a system, and here the intent is to evaluate its functionality as an implementation of the quantized phase concept. Its performance in beam steering and focal quality will be compared to an infinite phase resolution protocol and simulations run for a theoretical array of similar dimensions.

6.2 Material and Methods

6.2.1. Numerical Simulations

As described in chapters 2, 3, and 4 the pressure fields were simulated using the Rayleigh-Sommerfeld sum, in conjunction with Huygen's Principle. In this case, in modeling the actual dimensions of the Imasonic 2725 BXXX transducer introduced in the previous chapter, the simulated array was given at total area of 83.2mm x 30mm. However, in order to model the curved surface of the transducer, each of the 128 elements in the simulated array was broken up into 67 0.44mm x 0.55mm sub-elements with 0.45mm inter-element spacings. This size and distribution was chosen, since, as described in the Chapter 2, the 0.45 spacing satisfies the $< \lambda/2$ requirement and best approximates the focusing ability of a cylindrically curved transducer.

As before, the medium was assumed to water and the total power of the array was 1W. Because curved linear transducers are designed for optimal focusing only in 1 dimension the focus was moved in the y direction along the length of the array. The orientation of the array is the same given in previous sections. The focus was placed in various locations and the effect on the overall pressure field was observed. All simulations were written using MATLAB and were run using a PC with an Athlon XP 2800 processor.

6.2.2 *Electrical Testing*

6.2.2.1 Input amplifier Testing

While the 128-element Imasonic array is resonant at 1.1MHz, i.e. has its highest output power for a given input at 1.1 MHz, the overall frequency response of the input amplifier was assessed. A 0.5Vpp sinusoidal signal was used as an input to each of the 4 opamp circuits in the input amplifier, and the frequency was varied from 0.01 to 10MHz, for a 50Ω load. The input was provided by Stanford Research Systems Model DS345 and Agilent 33250A signal generators, and power given by a Topward Electric Instruments Co LTD TPS-4000 Series power supply.

It was discovered during testing that the HS02 heat sink, while sufficient for the 10% duty cycle used during actual medical treatments, was inadequate for continuous operation at 2A. Since the goal was to produce a measurable pressure field, a voltage output of 4.5 Vpp was chosen for each channel. This value allowed the amplifiers to run, with a small fan, for several consecutive hours, with very little heating. To verify that the system could be run at higher output levels, experiments were run which used larger input voltages (see acoustical testing section).

6.2.2.2 Flex Circuit Assembly and Transducer Array Testing

In order to assess the effects of the flex circuit and coaxial cable assembly on the overall system, phase and impedance measurements were taken of the cable alone, the transducer and the cable together and the entire assembly (flex circuit, transducer and cable).

6.2.3 *Acoustical Testing*

In order to assess the effectiveness of the quantized phase concept for use in beam steering applications, the HDAADS system was used to create and move foci to a number of locations. The overall acoustical testing arrangement is shown in Figure 6.1. The assembly works as the ultrasound waveform is generated by the HDAADS and the pressure field is measured using a 0.2mm hydrophone needle, which uses a Velmex Inc VP9000 Controller for positioning. The captured signal is amplified using a Preamble

Instruments 1820 Differential Amplifier, and recorded by a Techtronix TDS 3012 oscilloscope.

To test the viability of the simple quantized phase concept, experiments were run which compared simulated quantized phase, experimental infinite phase resolution and quantized phase results. The overall pressure squared field in the YZ-plane was obtained for each regime, with the focus being placed at (0,0,40)mm and (0,16,40)mm. It should be noted that for the comparisons with the infinite phase resolution case, only the first 100 elements in the array were used. This was done because the amplifier system, which generates the waveforms for the high phase resolution case, only has 100 channels. It should also be noted that the resolution of the "infinite" resolution system is actually 3^{o}. In both the simulated and experimental arrangements, the resolution in the Y direction was 1mm and in Z was 1mm, over a range of Y = -10mm to 10mm and Z = 10mm to 70mm.

Next, the central line pressure squared fields from Z= 30m to 60mm, in 10mm increments, for line along X=Y= 0mm were calculated for each of the 4 phase increment cases. The spatial resolution for the simulations and experiments was 0.25mm in the Z direction (since the scan ran in Z along the line containing the origin, no resolution values are given for the X or Y axis).

To verify that the amplifier could run at higher input voltages, the focus was placed at (0,0,40) and input was to be varied from 5Vpp to 40Vpp in 5V increments, and the output recorded. However, it was discovered that there was distortion in the signal of one of the amplifiers when the voltage was increased to greater than 13Vpp. Investigation revealed that it was a slew rate issue, caused primarily by the current limiting resistors, which were set to only allow 1.2A. A 13Vpp output signal at 1.1MHz, into a 730pF load, requires approximately I = Cdv/dt = 1.3A (see section 7.2.1 for deviation of load value) As such, the measurements were only taken from 1Vpp to 13Vpp, in 1 Volt increments.

Lastly, in anticipation of use for treating larger volume, which require rapid movement of the focus, an examination of the timing limitations of the HDAADS was performed. This included calculating the delays associated which each component in the signal path of the circuit.

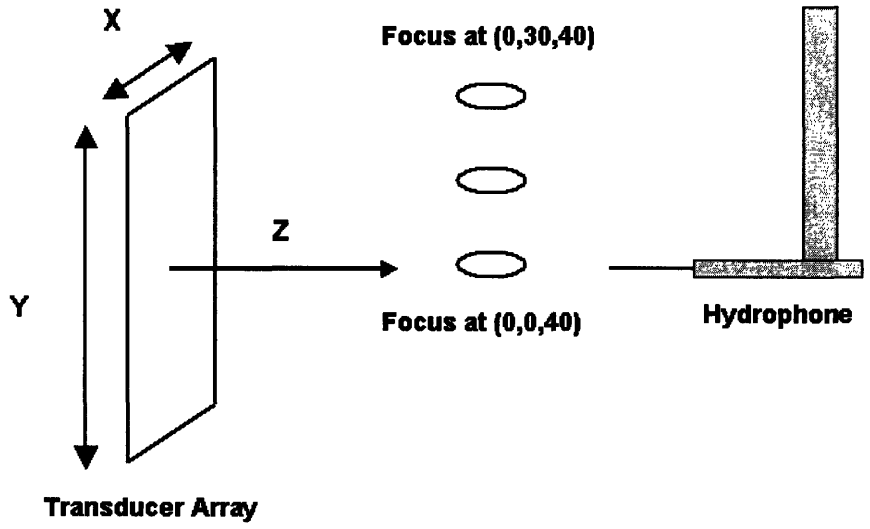

Figure 6.1 The 128-element transducer array acoustical testing arrangement

6.3 Results

6.3.1 Electrical Testing Results

The output characteristics of the input phase amplifier are shown in Figure 6.2.

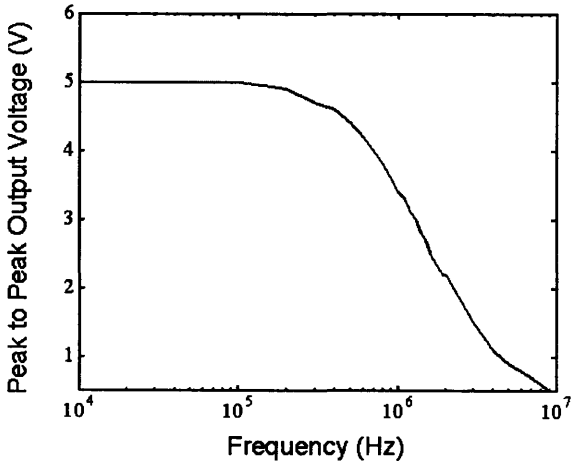

Figure 6.2 The frequency response of the HDAADS Input Amplifier.

It should be noted that each of the 4 amplifiers, had output values that were identical for most frequencies, which the largest difference being approximately 4%. As such, Figure 6.2 only shows the values for channel 1. Observe that at 1.1MHz the response has already declined by 40% from its initial value.

Figure 6.3 shows the impact of the flex circuit assembly and its subsections on the HDAADS. Note that in Figure 6.3 the phase response is largely dominated by the co-axial cables, which contribute more than 300pF of capacitance, resulting in a significant phase shift. The magnitude of the impedance is also largely governed by the cable. It should be noted that at the transducer resonant frequency of 1.1 MHz, each channel has a magnitude of approximately 350Ω and phase shift of -88°. This fact will have important implications for the amount of power that will actually reach the array itself.

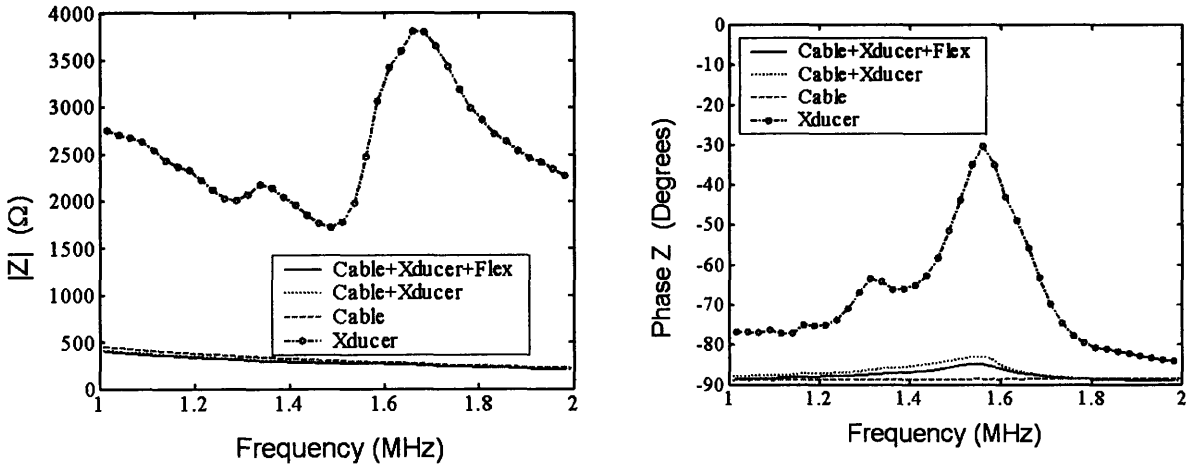

Figure 6.3 Graph of the phase and magnitude of the impedance of the 128-element transducer, mini co-axial cable and flex circuit assembly. Note the measurements of the array were actually taken from a 24-element array, which had the same manufacture's specifications for element size, material, radius of curvature and resonant frequency, as the 128-element version, except that there were fewer elements

Observe that with the addition of the flex circuit, the characteristics of the assembly change very little, with the phase still being approximately -88° and the magnitude 330Ω

at 1.1MHz. However, it should be noted that the flex does add a small bit of negative phase, implying that it has a capacitive contribution. If the flex circuit were much longer, its contribution to the capacitance of the assembly would likely increase

6.3.2 Acoustical Testing Results

Figure 6.4 shows the experimental pressure squared field for the 128-element linear array.

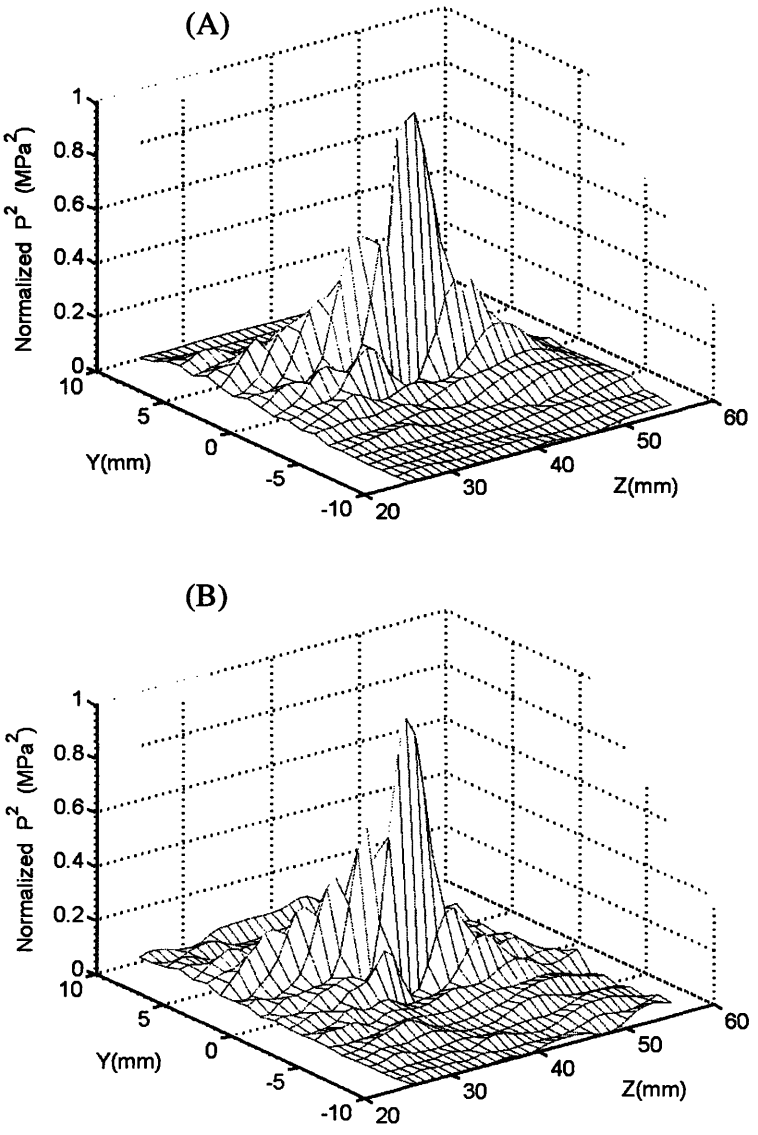

Figure 6.4 The normalized pressure squared field for a 128-element linear array with focus at (0,0,40)mm. (A) infinite phase resolution (B) 4 phase increments

Figure 6.5 gives the simulated results for the 128-element linear array.

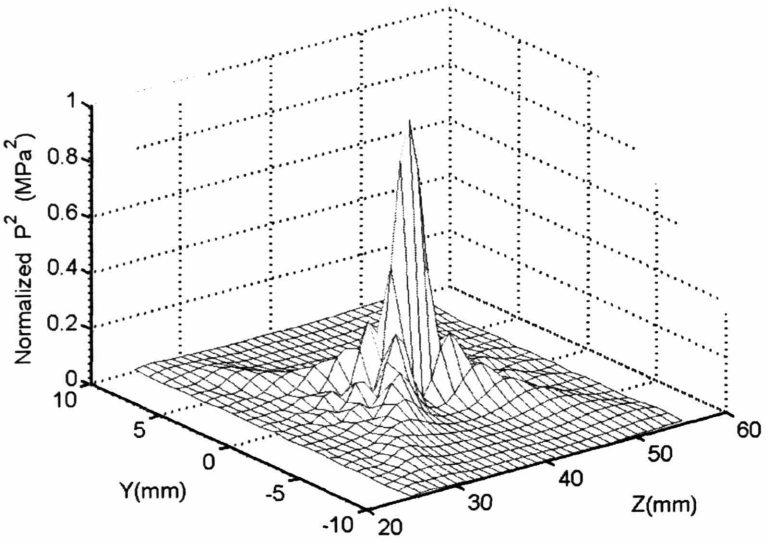

Figure 6.5 Simulated pressure squared field for a 128-element linear array, with focus at (0,0,40)mm

Note that a clear focus is present in Figure 6.4B and that there is little extrafocal activity. Also of note is the presence of a slight distortion on the near field side of the peak. This structure likely results from variations in the manufacturing of the elements in the array. Observe that the distortion is also present in the infinite resolution case shown in Figure 6.4A. Of importance is that fact that the foci in Figure 6.4 are very similar to one another, suggesting that the phase quantization protocol is effective and affected in ways similar to the infinite resolution case. With the exception of the extra lobe, both experimental results resemble the simulated field given in Figure 6.5.

Figure 6.6 gives the 10% contour plots for the simulated and experimental fields in Figures 6.4 and 6.5. Note the slight distortion in the experimental results.

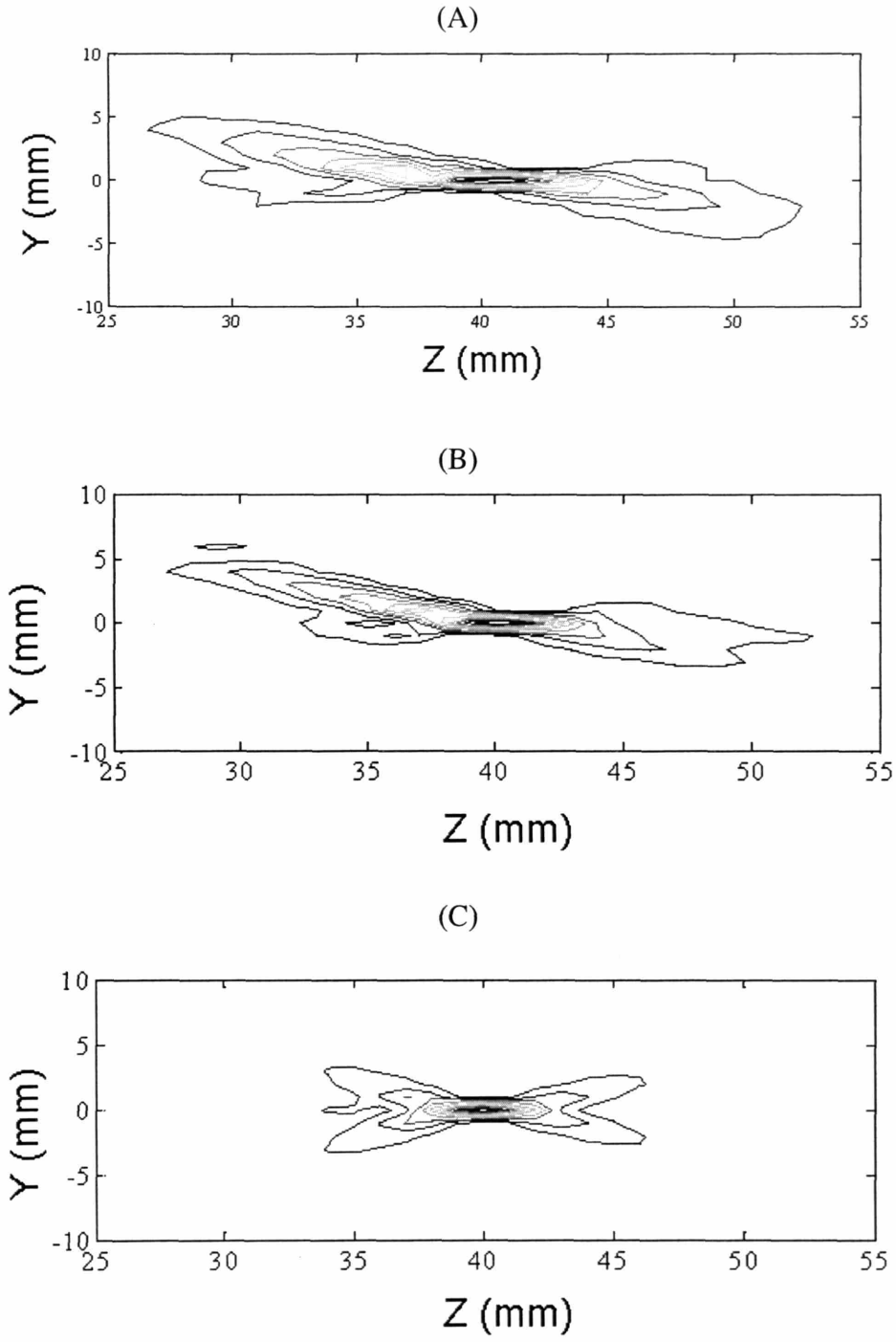

Figure 6.6 The 10% Contour plots of the experimental results for the 128-element linear array with the focus at (0,0,40)mm (A) experimental infinite phase resolution case (B) experimental 4 phase increments case (C) simulated 4 phase increments

Observe that the general shapes are similar, with the quantized case having slightly more energy deposited just outside of the focus. Figures 6.7 and 6.8 show the normalized pressure squared field for the experimental infinite resolution and 4 phase increment, and simulated 4 phase increment case respectively, with the focus at (0,16,40).

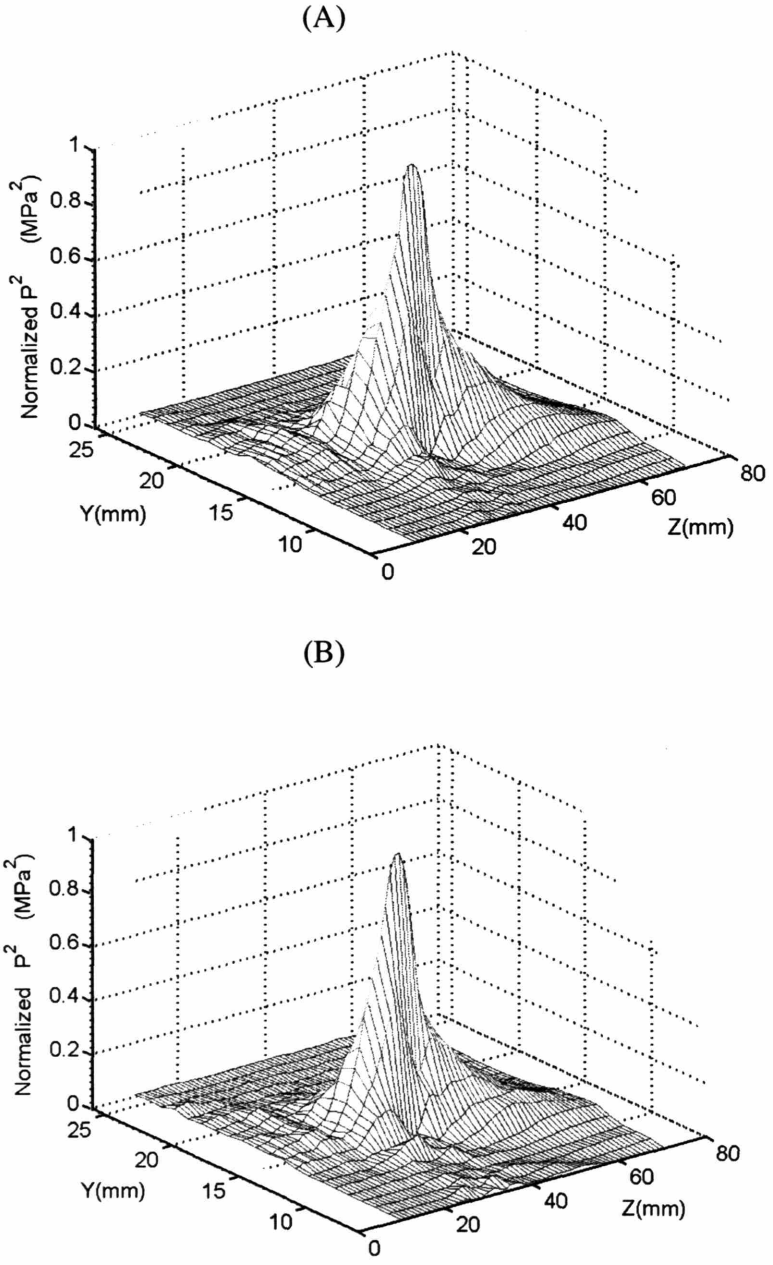

Figure 6.7 The normalized pressure squared field for a 128-element linear array with focus at (0,16,40)mm. (A) experimental infinite phase resolution (B) experimental 4 phase increments

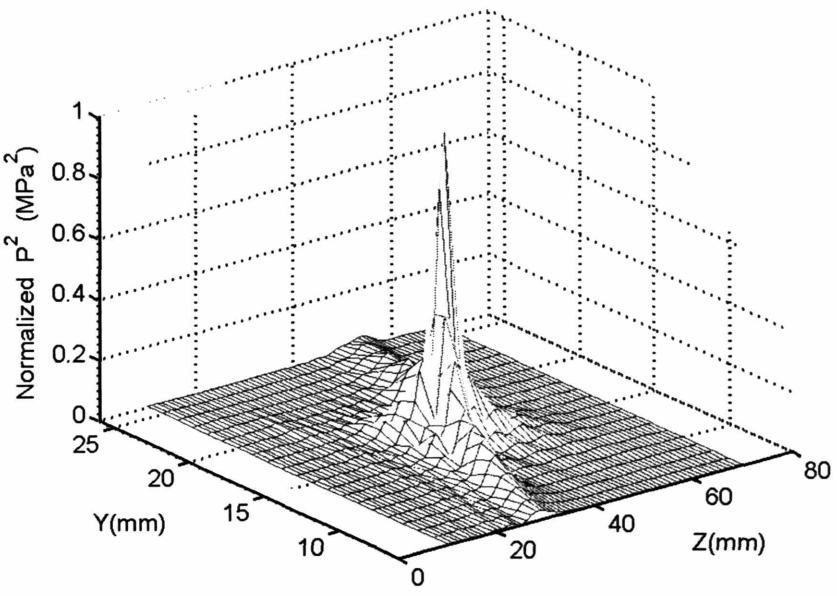

Figure 6.8 Simulated pressure squared field for a 128-element linear array, with focus at (0,16,40)mm

Observe that, similar to the centered focal arrangement, a clear focus is present. In this case, the distortion manifests itself as a broadening of the focus. As before, this effect is likely due to manufacturing variations the transducer elements. However, it should be noted that both of the experimental results are consistent with one another, though they differ slightly from the simulated results.

Figure 6.9 gives the 10% contour plots for the fields in Figures 6.7 and 6.8. Here, the spreading of the focus in the experimental results can be seen more clearly. However, the absence of significant sidelobes is also evident, suggesting that they have been absorbed by the spreading of the main peak. Because the focus is still clearly defined, this spreading would not likely have a significant impact on the array's performance in clinical applications.

(A)

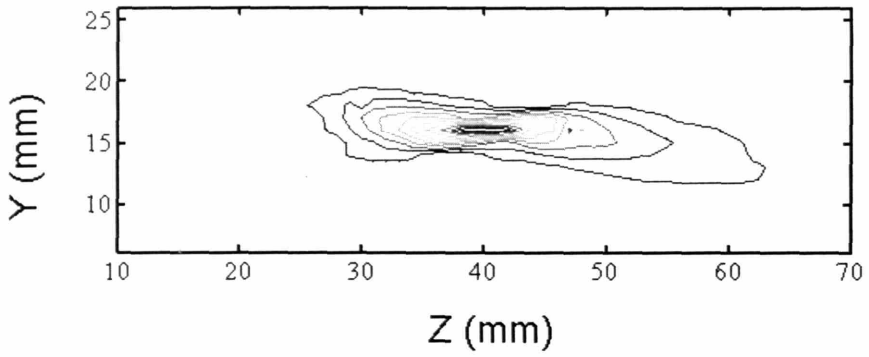

(B)

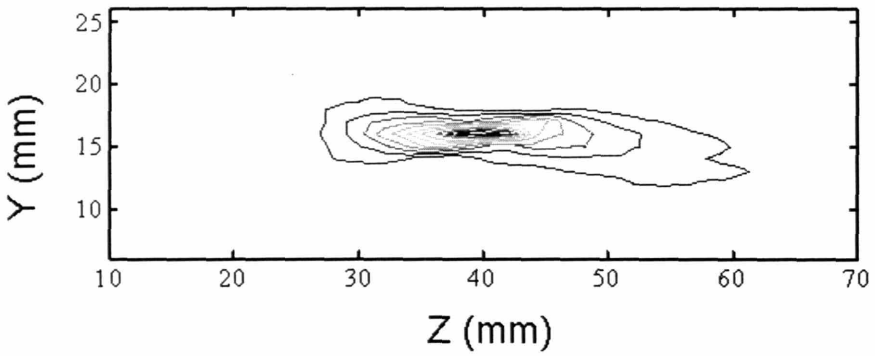

(C)

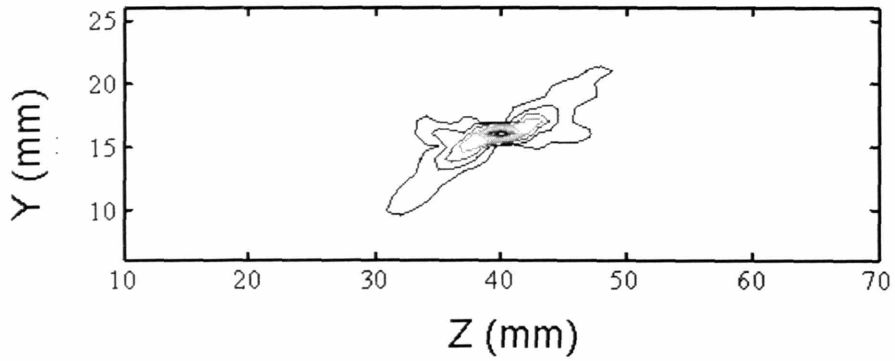

Figure 6.9 The 10% contour plots of the experimental results for the 128-element linear array with focus at (0,16,40) (A) experimental infinite resolution case (B) experimental 4 phase increment case (C) simulated 4 phase increments case

Figure 6.10 gives the normalized pressure squared along the central axis for the 128-element array for the two assignment protocols. Note that the peak values away from Z=40mm are smaller, which results from the fact that the transducer has a radius of curvature = 40mm. Figure 6.11 shows the normalized pressure amplitude as a function of the cable assembly input amplitude.

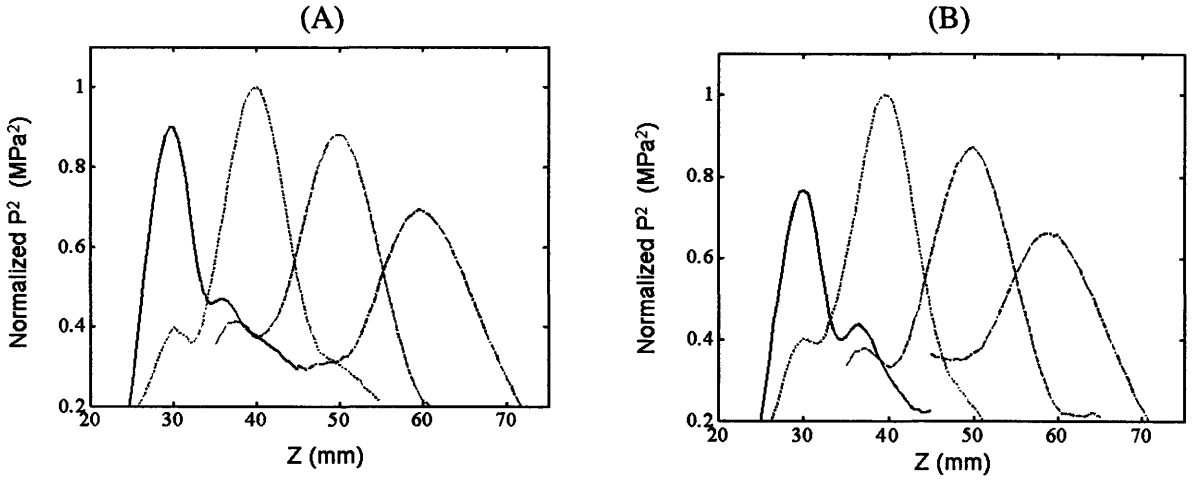

Figure 6.10 A graph of the central axis plots for the 128-element linear array along the line (0,0,Z) for foci at 20, 30 ,40, 50, and 60m. (A) for the infinite phase resolution case (B) the 4 phase increment configuration

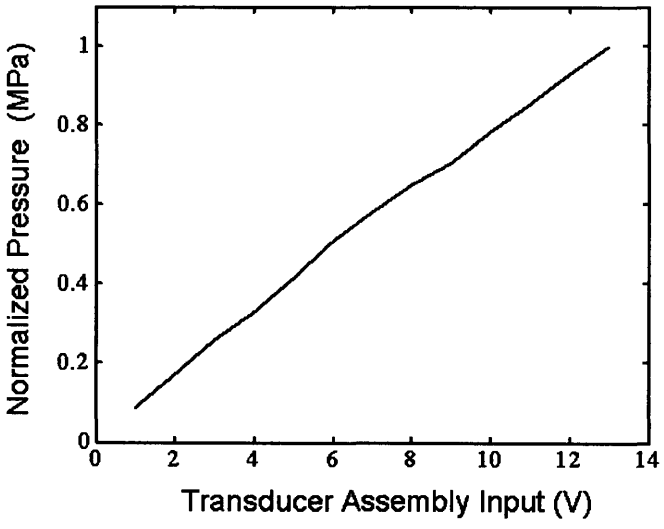

Figure 6.11 The relationship between input and output signal amplitude for the HDAADS

Note that, as one might expect, in general the relationship is between the output and input in Figure 6.11 is linear.

While the experimental results presented thus far suggest that beam steering is possible using a quantized phase assignment protocol, the question may arise as to how quickly the focus could be moved. This question is important in the context of treating larger volumes, which might require nearly continuous movement of the focus. Table 7.1 gives the conservative values for the total delay for one channel of the HDAADS, which is the sum of the propagation delay, set up time etc. for each of the components.

Component	Delay (ns)
Decoder (784HCT238)	600
Latch (74AC16373)	60
Switch (ADG452)	320
Software (4 channels)	~400
Total	~1400 = 1.4us

Table 7.1 The delays associated with 1 channel of the HDAADS

The delay of 1.4us given in Table 7.1 is the time that it would take to change the value of one group of switches associated with a particular latch (switches are loaded in parallel, see Figure 5.9). As such, the total time for shifting the focus of the 128-channel HDAADS (with 32 latches) is 32 x 1.4us = 44.8us. For a 128x128 element array (16384 elements), this would require 4096 latches, or 4096 x 1.4us = 5.73ms. If a duty cylce of 50% is assumed (the transducer is off during loading), the focus can be shifted approximately 1 / (2 x 5.73ms) = 87 times per second.

6.4 Discussion and Conclusions

Traditional therapeutic ultrasound systems have relied on a 1 to 1 arrangement between individual elements and their corresponding amplifiers for delivering phase information in phased array devices. This study has attempted to show that it is possible to significantly reduce the number of lines needed to drive and manage a relatively large number of elements, without sacrificing focal quality or beam steering capability. Experiments done using a linear 128-element cylindrically-curved transducer array suggests that quantizing the phase effectively accomplishes this reduction.

Figure 6.5 shows that when the focus in at the origin of the plane Z=40mm, which is at the radius of curvature of the array, the pressure square field for the infinite resolution and the 4 phase increment case are very similar. The 10% contour plots in Figure 6.6 show similar agreement. Examination of the central lines plots in Figure 6.10 also show that 4 phase case tracks the ideal scenario closely. From these results, one can conclude that both on the central axis and off-axis beam steering can be done, using only a limited number of phase increments, in this case 4.

As such, the focal control that would have to taken 128 input lines in a traditional system, has been reduced to only 24. It should be noted that only half of the scaling capability of the 128-channel selection PCB has been used. The main decoder, which is used to select the latches to be loaded, only has 4 of its 8 outputs in used. The unused 4 outputs have the potential to control 32 more latches, or 128 additional channels. If these additional channels were added then the overall area per channel would decrease from approximately 750mm^3/channel to 660mm^3/channel.

Investigation of Figure 6.2 shows that at 1.1MHz the response of the input amplifier has already began to decline. This suggests that the 52pF capacitor used to compensate the system is too large. A smaller capacitor would give the system greater bandwidth, and allow more efficient use to be made of the amplifier. During the acoustical testing, slight amplitude adjustments had to be made to each of the 4 inputs to phase selection PCB to ensure that they were the same, i.e. the outputs of the amplifier.

This likely resulted from the fact that the loop gain of the opamp was not high enough to handle the load variations that come with moving the focus to different locations. Overall, the system performance was acceptable for creating a measurable field and focus, though improvements could be made to the input amplifier to increase the output power, e.g. selection of a larger heat sink and more effective compensation.

One common method that could be employed to better compensate the amplifier is called lead compensation. Since the PA19 used in the core of the circuit is, in effect, a two-stage op amp, it would be possible to easily change the frequency response with very few components. The initial roll off in the open loop transfer function results from the 52 pF compensation capacitor shown in Figure 5.12., with the later accelerated decline near the unity gain frequency is caused by the internal capacitances of the opamp. Because the compensation capacitor is too large, the initial roll off begins early. As a result, the transfer function crosses unity gain well before the second pole can contribute more negative phase, and drive the circuit towards instability. While this value for the compensation capacitor ensures that the amplifier is stable, it also makes it so that at 1.1 MHz the loop gain has become so low that the feedback afforded by a high gain op amp is lost.

To correct this situation, a smaller compensation capacitor could be used. This would then require some method for preventing the second pole from significantly altering the phase of the transfer function before it reaches 1.1MHz. This neutralization is accomplished by simply placing a resistor Rc in series with the compensation capacitor, as shown in Figure 6.12. What this addition does is to introduce a zero into the transfer function. This zero can then be moved to the left of the second opamp pole, thus introducing a positive phase shift and increasing the phase margin. We thus would have a configuration which is both stable and has an increased loop gain at 1.1 MHz. By restoring the loop gain, the feedback capabilities of the circuit are recovered, and the need to adjust the amplitude of the output for each focal location is removed.

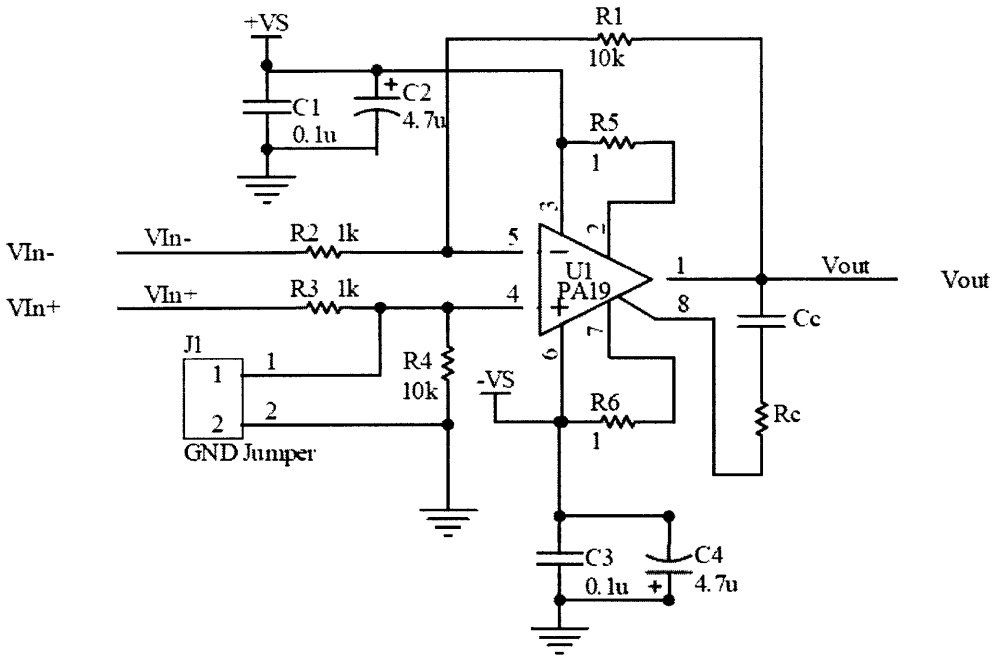

Figure 6.12 A schematic for an improved compensation scheme for the HDAADS input phase amplifier

While more effectively compensating the opamp does improve system performance in general, in this case, the limiting factor is the slew rate of the PA19. As described in section 6.2.3, at 1.1MHz the output of the amplifier is limited to 13Vpp, which is due to the fact that we have a large capacitive load and relatively large current limiting resistors. When the frequency was reduced to 0.5MHz the output could be taken as high as 36Vpp for +20V and –20V rails. Subsequent version of the circuit should consider employing smaller limiting resistors.

7 Conclusions and Recommendations for Future Work

7.1 Conclusions

In recent years, the move towards using phased arrays in the therapeutic applications of ultrasound and the drive for $\lambda/2$ inter-element spacings has presented an interesting problem for practical implementations of FUS systems. This study has attempted to present a series of solutions to the issues of constructing high density arrays and managing the distribution of power and information elements. Overall, the concept of quantizing the input phase shows promise for future use in therapeutic applications.

Simulations of a 128x128 element arrays with $< \lambda/2$ inter-element spacings and only 4 phase increments show strong agreement with the infinite phase resolution implementation of similar arrays. This is true along a number of metrics, including sidelobe to main lobe ratio, and 3dB beam length, width and volume. The only metric where there is significant deviation is peak pressure squared, which has a difference of approximately 20%. However, as demonstrated in chapter 4, the extra-focal energy lost in the quantized case is diffuse, and as such allows correction of the lower peak pressure by simply increasing the input signal. Moreover, simulations show that by using amplitude apodization, a volume of over 288 cm^3 can be effectively treated.

This study has also provided one possible implementation of the quantized phase technique in the High Density Array Addressing and Driving System (HDAADS). Measurements of the device show that an appreciable amount of power can be delivered to a $<\lambda/2$ spaced array, and is enough to generate a significant pressure field in water. Investigation of the data from the HDAADS reveals that focusing is possible and that beam steering can successfully be done over a range of 30 millimeters. In addition, the design of the 128-channel HDAADS easily lends itself to scaling to larger numbers of channels. For example, expanding the assignment protocol used by the system, the number of control lines for a 10,000-element array could be reduced from 10,000 to only 30.

In demonstrating the functionality of the HDAADS and the results of larger aperture array simulations in chapters 1 – 4, it has been shown that phase quantization shows potential as a viable option for being able to successfully drive large numbers of closely spaced transducer elements.

7.2 Recommendations for Future Work

7.2.1 The Current Model

While this study has offered solutions to some of the major impediments to moving to larger scale $<\lambda/2$ arrays, there is considerable work that could be done to further improve system performance and fabrication. As shown in Chapter 6, there is a tremendous amount of the power that is lost in driving the mini-co-axial cables that connect the input phase selection PCB to the 128-element array. This results from the fact that the wires are highly capacitive, at about 30pF/ft. As such, the phase shift of -88^{o} severely limits the amount of power that actually reaches the elements. In addition, there is the capacitance of the HDAADS phase selection board, which is significant at 350 pF/channel, resulting from the capacitance of the AD452 switches (1 x 140pF "on" capacitance + 3 x 37pF "off" capacitance = 350pF total capacitance for the quad package). Figure 7.1 shows a circuit which models the behavior of the cable assembly, board, and transducer.

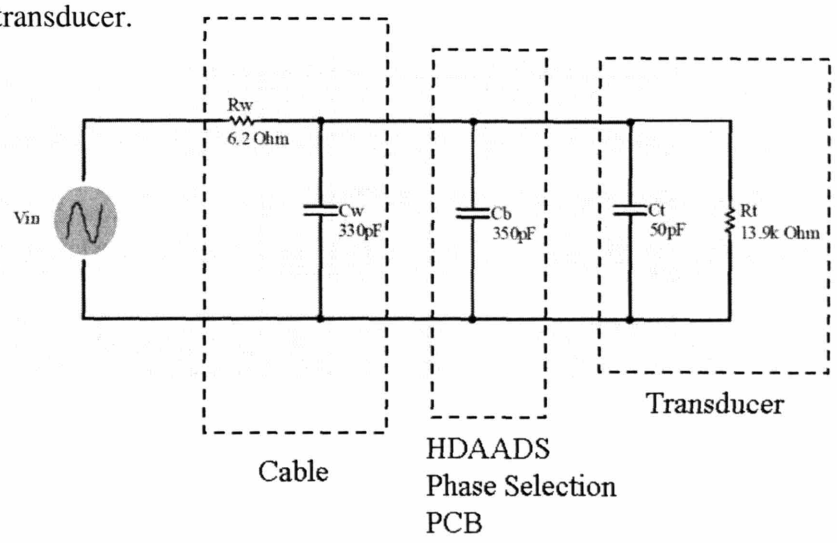

Figure 7.1 A schematic of a circuit that models the behavior of the cable, HDAADS phase selection PCB, and flex circuit assembly

As can be seen from the schematic, much of the current from the signal source goes to charging the 330pF capacitor from the cable and 350pF capacitor from the board, thus greatly reducing the power dissipated in the load. Calculations at 1.1MHz with an input voltage of 48Vpp reveal that approximately 53mW is delivered by the source, with 20.7mW being dissipated at the load. If this circuit were scaled to 40 channels, which is a number that one of the amplifiers in the HDAADS might see, the supply power becomes 2.1W and load dissipation is 0.83W. If one were then to add a modest biasing current of 100mA for the opamp (used by the PA19, not modeled in the simulation) for +25V and –25V rails, the total power out of the supply becomes 2.1W + 50V x 100mA = 7.1W of which 0.83W goes to the load, giving and over all efficiency of 11.7%. The main contributors to the inefficiency of the system are the opamp biasing power and the cable and board capacitances. There are two ways that one might go about increasing the efficiency 1) find another way to drive the capacitance of the cable and board and 2) remove the cable and board capacitance altogether.

7.2.2 An Alternate Amplifier

We first consider an alternate way of managing the co-axial wire contribution. Figure 7.2 shows a resonant circuit.

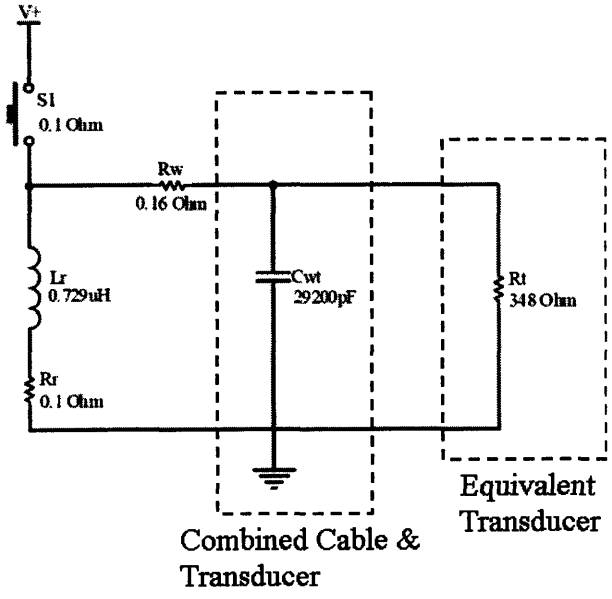

Figure 7.2 A schematic for a circuit used to counter the capacitance introduced by the co-axial cable and HDAADS phase selection board. Note, that the board, cable and transducer capacitances for 40 channels have been combined into one value, 29200pF, which is quite large

The circuit functions as the switch S1 closes briefly, connecting the end of the tank inductor Lr and Cwt (which represents the total capacitive contribution from the transducer, board, and cables) capacitor to V+. This causes the capacitor to charge towards V+. As the capacitor voltage peaks, it begins to discharge through the inductor. The inductor current eventually discharges the capacitor through the small cable resistance, and pulls the capacitor voltage negative towards V-. As the capacitor voltage nears V-, the inductor current reverses and begins to charge the negative voltage, which has formed on the capacitors. This continues until the capacitor voltages nears V+ (it does not reach it because some power has been dissipated in the small cable and transducer resistances, which have been ignored until now to simplify explanation). At this point, the switch is closes again, temporarily tying the capacitors to V+ and providing the current necessary to charge nearer to V+ and begin the cycle again.

This process continues, generating a close approximation of a sine wave at the frequency of the opening and closing of the switch (which could be set to 1.1 MHz). The amplitude of the signal is determined by the Q of the system, which is maximized by setting $(LC)^{-1/2} = 2\pi f = 2\pi 1.1\text{MHz}$. Because the capacitance varies as a function of the number of channels assigned to a given phase, a method is needed to keep the tank capacitor value constant. This could be done by assuming that each amplifier sees 40 channels (the maximum value observed from a survey focal locations) and thus 40 x (350pF + 330pF +50pF) = 29.2nF. Whenever a given amplifier has less than 40 channels the deficit can be made up by connecting it to bank of "dummy" capacitors, with each capacitor having a value of 730pF, which is roughly equivalent to 1 channel (the number of channels assigned to each amplifier (phase) is already currently calculated by the phase assignment software).

It should be noted that because the only power delivered by the supply is given when the switch is closed, this method does not require biasing, and results in a higher efficiency. Simulations show that for V+ = 25V with a duty cycle of 14.5% at 1.1MHz, Lt = 0.729uH, the power from the supply is 2W and the power to the load is 0.83W

yielding an efficiency of 41.5%. Thus the system is nearly 4 times as efficient as the current system. It should be noted that, in this configuration, the cable and inductor resistances dissipate a large amount of power because of the large currents that are passed between the inductor and capacitor. As such, the efficiency of this circuit would degrade very quickly if lossy elements were to be used.

7.2.3 A Single Chip Implementation

While it would be possible to offset the effects of the cable, a more effective method would involve eliminating the cable altogether. Before addressing this issue it is necessary to examine a related problem, which concerns using a flex circuit to connect to the array. While the flex circuit offers a simple and efficient solution to connecting to a linear array of arbitrarily large size, it is constrained in its use for connecting to 2 dimensional arrays. This limitation results from the fact that design requires that an insulation-free area with strips of exposed copper be left to allow soldering. For a 2D arrangement, this method would prove quite difficult to use, especially for elements that are sub millimeter in size.

Overcoming these two obstacles will require adjustments to how the signals are physically transmitted to the board. On possible way to accomplish this would be to move the phase selection circuitry to a location directly on the back of the array. The HDAADS was designed and constructed using discrete components, which while simple and inexpensive, is a very space inefficient method for laying out a circuit. Since most of the components on the board are switches and simple digital components, much of the design could be reduced to a single chip, which could then be plugged into a mating connection on a custom-designed transducer array. One example of this approach is the use of ball grid arrays in integrated circuit (IC) applications. These particular chips have a larger two-dimensional pattern of input/output pins, as opposed to only the two rows of pins found in surface mount and through-hole kinds of IC's. This configuration removes the need for co-axial cables, thus greatly increasing the electrical efficiency of the system. This arrangement also addresses the issue of how to connect to a device with a 2D element arrangement.

Figure 7.3 shows a circuit which models the behavior of the transducer with the cables and board removed. Inspection shows that the power delivered by the supply is now 20.7 mW with all of it being dissipated in the load. For 40 channels this would equal 0.83W. Adding a biasing current of 100mA for an op amp running off of +25V and –25V rails gives a total power consumption of 50V x 100mA + 0.83mW = 14.2%. To further increase the performance of the arrangement, a resonant circuit configuration could be added, as described previously in this chapter.

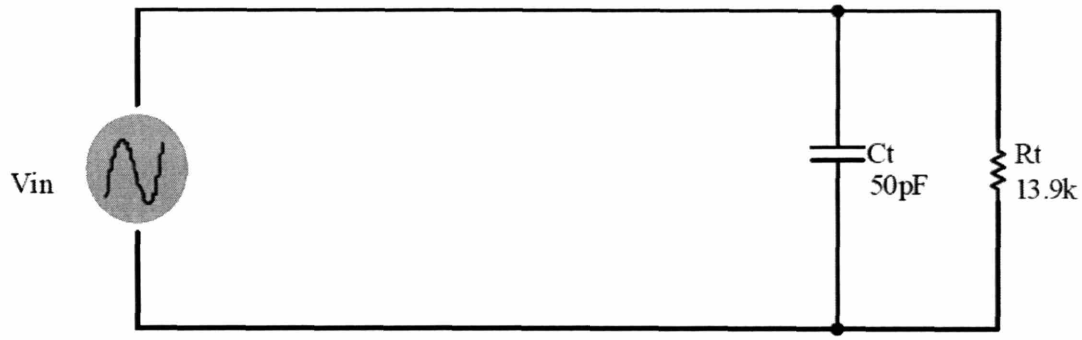

Figure 7.3 A schematic of a circuit that models the behavior of one channel of the transducer assembly with the cable removed

As such, moving towards a single chip implementation with a resonant amplifier driver would be a logical next step for implementation of the quantized phase concept.

8 References

1. Adams, J. B., Moore, R. G., Anderson, J. H., Strandberg, J. D., Marshall, F. F., & Davoussi, L. R. 1996, "High-intensity focused ultrasound ablation of rabbit kidney tumors", *Journal of Endourology*, vol. 10, no. 1, pp. 71-75.

2. Algan, O., Fosmire, H., Hynynen, K., Dalkin, B., Cui, H., Drach, G., Stea, B., & Cassady, J. R. 2000, "External beam radiotherapy and hyperthermia in the treatment of patients with locally advanced prostate carcinoma", *Cancer*, vol. 89, no. 2, pp. 399-403.

3. Amichetti, M., Valdagni, R., Graiff, C., & Valentini, A. 1991, "Local-regional recurrences of breast cancer: treatment with radiation therapy and local microwave hyperthermia", *Am.J.Clin.Oncol.*, vol. 14, no. 1, pp. 60-65.

4. Apfel, R. E. 1982, "Acoustic cavitation: a possible consequence of biomedical uses of ultrasound", *Br.J.Cancer Suppl.*, vol. 45, no. 5, pp. 140-146.

5. Arefiev, A., Prat, F., Chapelon, J. Y., Tavakkoli, J., & Cathignol, D. 1998, "Ultrasound-induced tissue ablation: studies on isolated, perfused porcine liver", *Ultrasound in Medicine and Biology*, vol. 24, no. 7, pp. 1033-1043.

6. Arustamov, D. L., Mukhtarov, S. T., & Arustamov, L. D. 2000, "[Transvesical radiofrequency needle ablation on prostatic benign hyperplasia] Transvezikal'naia radiochastotnaia igol'naia ablatsiia prostaty pri ee dobrokachestvennoi giperplazii", *Urologiia.*, vol. 4, no. 6, pp. 34-37.

7. Bagshaw, M. A., Prionas, S. D., Goffinet, D. R., Cox, R. S., Kapp, D. S., & Freiha, F. 1991, "External beam irradiation combined with the use of 192-iridium implants and radiofrequency-induced hyperthermia in the treatment of prostatic carcinoma", *Prog Clin Biol Res.*, vol. 370, pp. 275-279.

8. Benkeser, P. J., Frizzell, L. A., Ocheltree, K. B., & Cain, C. A. 1987, "A tapered phased array ultrasound transducer for hyperthermia treatment", *IEEE Transactions on Ultrasonics, Ferroelectrics and Frequency Control*, vol. UFFC-34, pp. 446-453.

9. Bihrle, R., Foster, R. S., Sanghvi, N. T., Fry, F. J., & Donohue, J. P. 1994, "High-intensity focused ultrasound in the treatment of prostate tissue", *Supplement to Urology*, vol. 43, no. 2, pp. 21-26.

10. Buchanan, M. T. & Hynynen, K. 1994, "Design and experimental evaluation of an intracavitary ultrasound phased array system for hyperthermia", *IEEE Trans.Biomed.Eng*, vol. 41, no. 12, pp. 1178-1187.

11. Burak, W. E., Jr., Agnese, D. M., Povoski, S. P., Yanssens, T. L., Bloom, K. J., Wakely, P. E., & Spigos, D. G. 2003, "Radiofrequency ablation of invasive breast carcinoma followed by delayed surgical excision", *Cancer*, vol. 98, no. 7, pp. 1369-1376.

12. Cain, C. A. & Umemura, S. A. 1986, "Concentric-ring and sector vortex phased array applicators for ultrasound hyperthermia therapy", *IEEE Transactions on Microwave Theory and Techniques*, vol. MTT-34, pp. 542-551.

13. Chapelon, J. Y., Ribault, M., Vernier, F., Souchon, R., & Gelet, A. 1999, "Treatment of localised prostate cancer with transrectal high intensity focused ultrasound", *Eur.J.Ultrasound.*, vol. 9, no. 1, pp. 31-38.

14. Chen, L., Rivens, I., ter Haar, G. R., Riddler, S., Hill, C. R., & Bensted, J. P. 1993, "Histological changes in rat liver tumours treated with high-intensity focused ultrasound.", *Ultrasound in Medicine and Biology*, vol. 19, pp. 67-74.

15. Chen, L., ter Haar, G., Robertson, D., Bensted, J. P., & Hill, C. R. 1999, "Histological study of normal and tumor-bearing liver treated with focused ultrasound", *Ultrasound.Med.Biol.*, vol. 25, no. 5, pp. 847-856.

16. Chung, A., Hynynen, K., Cline, H. E., Colucci, V., Oshio, K., & Jolesz, F. 1996, "Optimization of spoiled gradient-echo phase imaging for in vivo localization of focused ultrasound beam", *Magnetic Resonance in Medicine*, vol. 36, no. 5, pp. 745-752.

17. Cioni, D., Lencioni, R., Rossi, S., Garbagnati, F., Donati, F., Crocetti, L., & Bartolozzi, C. 2001, "Radiofrequency thermal ablation of hepatocellular carcinoma: using contrast-enhanced harmonic power doppler sonography to assess treatment outcome", *AJR.American Journal of Roentgenology*, vol. 177, no. 4, pp. 783-788.

18. Clarke, R. L. & ter Haar, G. R. 1997, "Temperature rise recorded during lesion formation by high-intensity focused ultrasound", *Ultrasound Med.Biol.*, vol. 23, no. 2, pp. 299-306.

19. Clement, G., Connor, C., & Hynynen, K. "Treatment planning for transskull ultrasound surgery and therapy".

20. Clement, G. T. & Hynynen, K. 2000, "Field characterization of therapeutic ultrasound phased arrays through forward and backward planar projection", *J Acoust.Soc.Am.*, vol. 108, no. 1, pp. 441-446.

21. Cline, H. E., Hynynen, K., Watkins, R. D., Adams, W. J., Schenck, J. F., Ettinger, R. H., Freund, W. R., Vetro, J. P., & Jolesz, F. A. 1995, "Focused US system for MR imaging-guided tumor ablation", *Radiology*, vol. 194, no. 3, pp. 731-737.

22. Coleman, D. J., Lizzi, F. L., Driller, J., Rosado, A. L., Chang, S., Iwamoto, T., & Rosenthal, D. 1985, "Therapeutic ultrasound in the treatment of glaucoma", *Ophthalmology*, vol. 92, pp. 339-346.

23. Damianou, C. A., Hynynen, K., & Xiaobing, F. 1995, "Evaluation of accuracy of a theoretical model for predicting the necrosed tissue volume during focused ultrasound surgery", *IEEE Transactions on Ultrasonics, Ferroelectrics and Frequency Control*, vol. 42, no. 2, pp. 182-187.

24. Daum, D. R. & Hynynen, K. 1999a, "A 256 Element Ultrasonic Phased Array System for Treatment of Large Volumes of Deep Seated Tissue", *IEEE Transactions on Ultrasonics, Ferroelectrics and Frequency Control*, vol. 46, no. 5, pp. 1254-1268.

25. Daum, D. R. & Hynynen, K. 1999b, "Theoretical design of a spherically sectioned phased array for ultrasound surgery of the liver", *Eur.J.Ultrasound.*, vol. 9, no. 1, pp. 61-69.

26. de Jong, N., Souquet, J., Faber, G., & Bom, N. 1985, "Transducers in medical ultrasound: Part Two. Vibration modes, matching layers and grating lobes", *Ultrasonics*, vol. 23, no. 4, pp. 176-182.

27. Delon-Martin, C., Vogt, C., Chigner, E., Guers, C., Chapelon, J. Y., & Cathignol, D. 1995, "Venous thrombosis generation by means of high-intensity focused ultrasound", *Ultrasound in Medicine and Biology*, vol. 21, no. 1, pp. 113-119.

28. Diederich, C. & Hynynen, K. 1989, "Induction of hyperthermia using an intracavitary multielement ultrasonic applicator", *IEEE Transactions of Biomedical Engineering*, vol. 36, pp. 432-438.

29. Diederich, C. J., Nau, W. H., Stauffer, P. R., Burdette, E. C., & Khalil, I. S. "Interstitial ultrasound applicators for localized thermal coagulation of tissue", IEEE, p. 1303.

30. Do-Huu, J. P. & Hartemann, P. 1981, "Annular array transducer for deep acoustic hyperthermia.", *IEEE Ultrasonics Symp.*, vol. 81CH1689-9, pp. 705-710.

31. Duck, F. A. 1990, *Physical Properties of Tissue: A Comprehensive Reference Book* Academic Press, Longdon; San Diego.

32. Duck, F. A. & Starritt, H. C. 1994, "A study of the heating capabilities of diagnostic ultrasound beams", *Ultrasound in Medicine and Biology*, vol. 20, no. 5, pp. 481-492.

33. Eaton, M. D., Melen, R. D., & Meindl, J. D. 1980, "A flexible, real time system for experimentation in phased array ultrasound imaging," in *Acoustic Imaging*, A. F. Metherell, ed., pp. 55-67.

34. Ebbini, E. S., Umemura, S.-I., Ibbini, M., & Cain, C. 1988, "A cylindrical- section ultrasound phased array applicator for hyperthermia cancer therapy", *IEEE Transactions on Ultrasonics, Ferroelectrics and Frequency Control*, vol. 35, pp. 561-572.

35. Ebbini, E. S. & Cain, C. A. 1989, "Multiple-focus ultrasound phased-array pattern synthesis: optimal driving-signal distributions for hyperthermia", *IEEE Transactions on Ultrasonics, Ferroelectrics and Frequency Control*, vol. 36, no. 5, p. 540.

36. Fallone, B. G., Moran, P. R., & Podgorsak, E. B. 1982, "Non-invasive thermometry with clinical X-ray CT scanner", *Med.Phys.*, vol. 9, pp. 715-721.

37. Fan, X. & Hynynen, K. 1995, "Control of the necrosed tissue volume during noninvasive ultrasound surgery using a 16 element phased array", *Med.Phys.*, vol. 22, pp. 297-308.

38. Fjield, T. & Hynynen, K. 1997, "The combined concentric-ring and sector-vortex phased array for MRI guided ultrasound surgery", *IEEE Transactions on Ultrasonics, Ferroelectrics and Frequency Control*, vol. 44, no. 5, pp. 1157-1167.

39. Fjield, T., Silcox, C. E., & Hynynen, K. 1999, "Low-profile lenses for ultrasound surgery", *Physics in Medicine and Biology*, vol. 44, no. 7, pp. 1803-1813.

40. Fjield, T., Sorrentino, V., Cline, H., & Hynynen, K. 1997, "Design and experimental verification of thin acoustic lenses for the coagulation of large tissue volumes", *Physics in Medicine and Biology*, vol. 42, no. 12, pp. 2341-2354.

41. Foster, R. S., Bihrle, R., Sanghvi, N. T., Fry, F. J., & Donohue, J. P. 1993, "High-intensity focused ultrasound in the treatment of prostatic disease", *European Urology*, vol. 23, pp. 29-33.

42. Francis, C. W. & Suchkova, V. N. 2001, "Ultrasound and thrombolysis", *Vasc.Med*, vol. 6, no. 3, pp. 181-187.

43. Fried, N., Roberts, W., Sinelnikov, Y., Wright, E., & Solomon, S. 2002, "Focused ultrasound ablation of the epididymis with use of thermal measurements in a canine model", *Fertil.Steril.*, vol. 78, no. 3, p. 609.

44. Frizzell, L. A., Benkeser, P. J., Ocheltree, K. B., & Cain, C. A. 1985, "Ultrasound phased arrays for hyperthermia treatment.", *IEEE Ultrasonics Symp.*, vol. 2, pp. 931-935.

45. Fry, W. J. 1968, "Intracranial anatomy visualized in vivo by ultrasound", *Investigate Radiology*, vol. 3, no. 4.

46. Gavrilov, L. R., Hand, J. W., Abel, P., & Cain, C. A. A method of reducing grating lobes associated with an ultrasound linear phased array intended for

transrectal thermotherapy. IEEE Trans.Ultrason.Ferroelectr.Freq.Control (USA) 44[5], 1010. 1997.

47. Gelet, A., Chapelon, J. Y., Bouvier, R., Pangaud, C., & Lasne, Y. 1999, "Local control of prostate cancer by transrectal high intensity focused ultrasound therapy: preliminary results", *J.Urol.*, vol. 161, no. 1, pp. 156-162.

48. Gelet, A., Chapelon, J. Y., Bouvier, R., Rouviere, O., Lasne, Y., Lyonnet, D., & Dubernard, J. M. 2000, "Transrectal high-intensity focused ultrasound: minimally invasive therapy of localized prostate cancer", *Journal of Endourology*, vol. 14, no. 6, pp. 519-528.

49. Goffinet, D. R., Prionas, S. D., Kapp, D. S., Samulski, T. V., Fessenden, P., Hahn, G. M., Lohrbach, A. W., Mariscal, J. M., & Bagshaw, M. A. 1990, "Interstitial 192Ir flexible catheter radiofrequency hyperthermia treatments of head and neck and recurrent pelvic carcinomas", *International Journal of Radiation Oncology, Biology, Physics*, vol. 18, no. 1, pp. 199-210.

50. Goss, S. A., Cobb, J. W., & Frizzell, L. A. "Effect of beam width and thermocouple size on the measurement of ultrasonic absorption using the thermoelectric technique.", pp. 206-211.

51. Goss, S. A., Frizzell, L. A., Kouzmanoff, J. T., Barich, J. M., & Yang, J. M. 1999, "Sparse random ultrasound phased array for focal surgery", *IEEE Transactions on Ultrasonics, Ferroelectrics and Frequency Control*, vol. 43, no. 6, pp. 1111-1120.

52. Greenleaf, W. J., Bolander, M. E., Sarkar, G., Goldring, M. B., & Greenleaf, J. F. 1998, "Artificial cavitation nuclei significantly enhance acoustically induced cell transfection", *Ultrasound Med Biol*, vol. 24, no. 587, p. 595.

53. Hacker, A., Kohrmann, K. U., Knoll, T., Langbein, S., Steidler, A., Kraut, O., Marlinghaus, E., Alken, P., & Michel, M. S. 2004, "High-intensity focused ultrasound for ex vivo kidney tissue ablation: influence of generator power and pulse duration", *Journal of Endourology*, vol. 18, no. 9, pp. 917-924.

54. Hazle, J. D., Diederich, C. J., Kangasniemi, M., Price, R. E., Olsson, L. E., & Stafford, R. J. 2002, "MRI-guided thermal therapy of transplanted tumors in the canine prostate using a directional transurethral ultrasound applicator", *J.Magn Reson.Imaging*, vol. 15, no. 4, pp. 409-417.

55. Hill, C. R., Rivens, I., Vaughan, M. G., & ter Haar, G. R. 1994, "Lesion development in focused ultrasound surgery: a general model", *Ultrasound Med.Biol.*, vol. 20, no. 3, pp. 259-269.

56. Hoffman, A. L., Wu, S. S., Obaid, A. K., French, S. W., Lois, J., McMonigle, M., Ramos, H. C., Sher, L. S., & Lopez, R. R. 2002, "Histologic evaluation and

treatment outcome after sequential radiofrequency ablation and hepatic resection for primary and metastatic tumors", *Am.Surg.*, vol. 68, no. 12, pp. 1038-1043.

57. Hutchinson, E. B. & Hynynen, K. 1996, "Intracavitary phased arrays for non-invasive prostate surgery", *IEEE Transactions on Ultrasonics, Ferroelectrics and Frequency Control*, vol. 43, no. 6, pp. 1032-1042.

58. Hutchinson, E. B. & Hynynen, K. 1998, "Intracavitary ultrasound phased arrays for prostate thermal therapies: MRI compatibility and in vivo testing.", *Medical Physics*, vol. 25, no. 12, pp. 2392-2399.

59. Hynynen, K. 1996, "Focused ultrasound surgery guided by MRI", *Science&Medicine*, vol. 3, no. 5, pp. 62-71.

60. Hynynen, K., Chung, A., Fjield, T., Buchanan, M. T., Daum, D., Colucci, V., Lopath, P., & Jolesz, F. 1996a, "Feasibility of using ultrasound phased arrays for MRI monitored noninvasive surgery", *IEEE Transactions on Ultrasonics, Ferroelectrics and Frequency Control*, vol. 43, no. 6, pp. 1043-1053.

61. Hynynen, K., Colucci, V., Chung, A., & Jolesz, F. A. 1996b, "Noninvasive artery occlusion using MRI guided focused ultrasound", *Ultrasound in Medicine and Biology*, vol. 22, no. 8, pp. 1071-1077.

62. Hynynen, K., Darkazanli, A., Unger, E., & Schenck, J. F. 1993, "MRI-guided noninvasive ultrasound surgery", *Med.Phys.*, vol. 20, no. 1, pp. 107-115.

63. Hynynen, K. & Davis, K. L. 1993, "Small cylindrical ultrasound sources for induction of hyperthermia via body cavities or interstitial implants", *International Journal of Hyperthermia*, vol. 9, pp. 263-274.

64. Hynynen, K., Dennie, J., Zimmer, J. E., Simmons, W. N., He, D. S., Marcus, F. I., & Aguirre, M. L. 1997, "Cylindrical ultrasound transducers for cardiac catheter ablation", *IEEE Transactions of Biomedical Engineering*, vol. 44, no. 2, pp. 144-151.

65. Hynynen, K., Freund, W. R., Cline, H. E., Chung, A. H., Watkins, R. D., Vetro, J. P., & Jolesz, F. A. 1996c, "A clinical noninvasive MRI monitored ultrasound surgery method", *RadioGraphics*, vol. 16, no. 1, pp. 185-195.

66. Hynynen, K. & Jolesz, F. A. 1998, "Demonstration of potential noninvasive ultrasound brain therapy through intact skull.", *Ultrasound in Medicine and Biology*, vol. 24, no. 2, pp. 275-283.

67. Hynynen, K. & Lulu, B. A. 1990, "Hyperthermia in cancer treatment", *Investigate Radiology*, vol. 25, no. 7, pp. 824-834.

68. Hynynen, K. & McDannold, N. 2004, "MRI guided and monitored focused ultrasound thermal ablation methods: a review of progress", *International Journal of Hyperthermia*, vol. 20, no. 7, pp. 725-737.

69. Hynynen, K., McDannold, N., Vykhodtseva, N., & Jolesz, F. A. 2001a, "Noninvasive MR imaging-guided focal opening of the blood-brain barrier in rabbits", *Radiology*, vol. 220, no. 3, pp. 640-646.

70. Hynynen, K., McDannold, N. J., & Jolesz, F. A. "The feasibility of MRI control of ultrasound surgery of large tumors.", p. -1943.

71. Hynynen, K., Pomeroy, O., Smith, D. N., Huber, P. E., McDannold, N. J., Kettenbach, J., Baum, J., Singer, S., & Jolesz, F. A. 2001b, "MR imaging-guided focused ultrasound surgery of fibroadenomas in the breast: a feasibility study", *Radiology 2001.Apr.;219.(1.):176.-85.*, vol. 219, no. 1, pp. 176-185.

72. Ibbini, M., Ebbini, E. S., & Cain, C. A. "Ultrasound phased arrays for hyperthermia: new techniques based on the field conjugation method", pp. 863-866.

73. Ishihara, Y., Calderon, A., Watanabe, H., Mori, K., Okamoto, K., Suzuki, T., Sato, K., Kuroda, K., Nakagawa, N., & Tsutsumi, S. 1992, "A precise and fast temperature mapping using water proton chemical shift", *Proc.SMRM* p. 4803.

74. Jenne, J. W., Bahner, M., Spoo, J., Huber, P., Rastert, R., Simiantonakis, I., Lorenz, W. J., & Debus, J. 1997, "CT on-line monitoring of HIFU therapy", *IEEE Ultrasonics Symp.*, vol. 2, pp. 1377-1380.

75. Jolesz, F. A., Hynynen, K., McDannold, N., Freundlich, D., & Kopelman, D. 2004, "Noninvasive thermal ablation of hepatocellular carcinoma by using magnetic resonance imaging-guided focused ultrasound", *Gastroenterology*, vol. 127, no. 5 Suppl 1, p. S242-S247.

76. Karrer, H. E., Dias, J. F., Larson, J. D., & Pering, R. D. "A phased array acoustic imaging system for medical use", pp. 757-762.

77. Karrer, H. E., Dias, J. F., Larson, J. D., & Pering, R. D. "A phased array acoustic imaging system for medical use", pp. 757-762.

78. Kim, H. J., Greenleaf, J. F., Kinnick, R. R., Bronk, J. T., & Bolander, M. E. 1996, "Ultrasound-mediated transfection of mammalian cells.", *Human Gene Therapy*, vol. 7, pp. 1339-1346.

79. Koehrman, K. U., Michel, M., Fruhauf, J., Volz, J., Back, W., & et.al. 2000, "High intensity focused ultrasound for non-invasive tissue ablation in the kidney, prostate and uterus", *Journal of Urology*, vol. 163, p. 698A.

80. Lafon, C., Chapelon, J. Y., Prat, F., Gorry, F., Margonari, J., Theillere, Y., & Cathignol, D. 1998, "Design and preliminary results of an ultrasound applicator for interstitial thermal coagulation", *Ultrasound.Med.Biol.*, vol. 24, no. 1, pp. 113-122.

81. Lele, P. P. & Parker, K. J. 1982, "Temperature distributions in tissues during local hyperthermia by stationary or steered beams of unfocused or focused ultrasound", *Br.J.Cancer Suppl*, vol. 45, no. 5, pp. 108-121.

82. Lizzi, F. L. & Ostromogilsky, M. 1987, "Analytical modelling of ultrasonically induced tissue heating", *Ultrasound in Medicine and Biology*, vol. 13, no. 10, pp. 607-618.

83. Madersbacher, S., Kratzik, C., Szabo, N., Susani, M., Vingers, L., & Marberger, M. 1993, "Tissue ablation in bening prostatic hyperplasia with high intensity focused ultrasound", *European Urology*, vol. 23, pp. 39-43.

84. Madersbacher, S., Pedevilla, M., Vingers, L., Susani, M., & Marberger, M. 1995, "Effect of high-intensity focused ultrasound on human prostate cancer in vivo.", *Cancer Research*, vol. 55, pp. 3346-3351.

85. Madio, D. P., van Gelderen, P., DesPres, D., Olson, A. W., De Zwart, J. A., Fawcett, T. W., Holbrook, N. J., Mandel, M., & Moonen, C. T. 1998, "On the feasibility of MRI-guided focused ultrasound for local induction of gene expression", *J.Magn.Reson.Imaging*, vol. 8, no. 1, pp. 101-104.

86. Maslak, S. H. 1975, *An Electronically Steered Ultrasonic Transducer,* PhD Dissertation, Massachusetts Institute of Technology.

87. McDannold, Hynynen, K., Wolf, D., Wolf, G., & Jolesz, F. 1998, "MRI evaluation of thermal ablation of tumors with focused ultrasound", *J.Magn.Reson.Imaging*, vol. 8, no. 1, pp. 91-100.

88. McGough, R. J., Wang, H., Ebbini, E. S., & Cain, C. A. 1994, "Mode scanning: heating pattern synthesis with ultrasound phased arrays", *International Journal of Hyperthermia*, vol. 10, no. 3, pp. 433-442.

89. Melliza, D. M. & Woodall, M. 2000, "Radiofrequency ablation of liver tumors: the complementary roles of the clinic and research nurse", *Gastroenterol.Nurs.*, vol. 23, no. 5, pp. 210-214.

90. Miller, D. L., Bao, S., Gies, R. A., & Thrall, B. D. 1999, "Ultrasonic enhancement of gene transfection in murine melanoma tumors", *Ultrasound in Medicine and Biology*, vol. 25, no. 9, pp. 1425-1430.

91. Miller, D. L., Kripfgans, O. D., Fowlkes, J. B., & Carson, P. L. 2000, "Cavitation nucleation agents for nonthermal ultrasound therapy", *Journal of Acoustic Society of America*, vol. 107, no. 6, pp. 3480-3486.

92. Mulligan, T. H., Lynch, D., Mulvin, J. M., Greene, J. M., Smith, J. M., & Fitzpatrick, J. M. 1998, "High intensity focused ultrasound in the treatment of benign prostatic hyperplasia", *Brit.J.Urol.*, vol. 79, pp. 177-180.

93. Nakahara, W. & Kabayashi, R. 1934, "Biological effects of ultrasound: mechanisms and clinical application", *Japanese Journal of Experimental Medicine*, vol. 12, p. 137.

94. Nakamura, K., Baba, S., Saito, S., Tachibana, M., & Murai, M. 1997, "High-intensity focused ultrasound energy for benign prostatic hyperplasia: clinical response at 6 months to treatment using Sonablate 200(tm)", *Journal of Endourology*, vol. 11, no. 3, pp. 197-201.

95. Phipps, J. H., Lewis, B. V., Roberts, T., Prior, M. V., Hand, J. W., Elder, M., & Field, S. B. 1990, "Treatment of functional menorrhagia by radiofrequency-induced thermal endometrial ablation", *Lancet*, vol. 335, no. 8686, pp. 374-376.

96. Porter, T. R., LeVeen, R. F., Fox, R., Kricsfeld, A., & Xie, F. 1996, "Thrombolytic enhancement with perfluorocarbon exposed sonicated dextrose albumin microbubbles.", *Am.Heart J.*, vol. 132, pp. 964-968.

97. Prat, F., Centarti, M., Sibille, A., Fadil, A., Henry, L., Chapelon, J. Y., & Cathignol, D. 1995, "Extracorporeal high-intensity focused ultrasound for VX2 liver tumors in the rabbit", *Hepatology*, vol. 21, no. 3, pp. 832-836.

98. Prat, F., Chapelon, J. Y., Abou El Fadil, F., Sibille, A., Theilliere, Y., Ponchon, T., & Cathignol, D. 1994, "Focused liver ablation by cavitation in the rabbit: a potential new method of extracorporeal treatment.", *Gut.*, vol. 35, no. 3, pp. 395-400.

99. Prior, M. V., Phipps, J. H., Roberts, T., Lewis, B. V., Hand, J. W., & Field, S. B. 1991, "Treatment of menorrhagia by radiofrequency heating", *International Journal of Hyperthermia*, vol. 7, no. 2, pp. 213-220.

100. Rivens, I. H., Rowland, I. J., Denbow, M., Fisk, N. M., ter Haar, G. R., & Leach, M. O. 1999, "Vascular occlusion using focused ultrasound surgery for use in fetal medicine", *Eur.J Ultrasound.*, vol. 9, no. 1, pp. 89-97.

101. Rowland, I. J., Rivens, I., Chen, L., Lebozer, C. H., Collins, D. J., ter Haar, G. R., & Leach, M. O. 1997, "MRI study of hepatic tumours following high intensity focused ultrasound surgery", *British Journal of Radiology*, vol. 70, pp. 144-153.

102. Saleh, K. Y. & Smith, N. B. 2005, "A 63 element 1.75 dimensional ultrasound phased array for the treatment of benign prostatic hyperplasia", *Biomed.Eng Online.*, vol. 4, no. 1, p. 39.

103. Sanghvi, N. T., Foster, R. S., Bihrle, R., Casey, R., Uchida, T., Phillips, M. H., Syrus, J., Zaitsev, A. V., Marich, K. W., & Fry, F. J. 1999, "Noninvasive surgery

of prostate tissue by high intensity focused ultrasound: an updated report", *Eur.J.Ultrasound.*, vol. 9, no. 1, pp. 19-29.

104. Sanghvi, N. T., Fry, F. J., Bihrle, R., Foster, R. S., Phillips, M. H., Syrus, J., Zaitsev, A. V., & Hennige, C. W. 1996, "Noninvasive surgery of prostate tissue by high-intensity focused ultrasound.", *IEEE Transactions on Ultrasonics, Ferroelectrics and Frequency Control*, vol. 43, no. 6, pp. 1099-1110.

105. Sato, M., Watanabe, Y., Kashu, Y., Nakata, T., Hamada, Y., & Kawachi, K. 1998, "Sequential percutaneous microwave coagulation therapy for liver tumor", *Am.J.Surg.*, vol. 175, no. 4, pp. 322-324.

106. Sheljaskov, T., Lerch, R., Fuchs, A., & Schatzle, U. A phased array antenna for simultaneous thermotherapy and sonography. 1997 IEEE Ultrasonics Symposium Proceedings.An International Symposium (Cat.No.97CH36118.) , 1701. 1997.

107. Sherar, M. D., Gertner, M. R., Yue, C. K., O'Malley, M. E., Toi, A., Gladman, A. S., Davidson, S. R., & Trachtenberg, J. 2001, "Interstitial microwave thermal therapy for prostate cancer: method of treatment and results of a phase I/II trial", *Journal of Urology*, vol. 166, no. 5, pp. 1707-1714.

108. Sibille, A., Prat, F., Chapelon, J. Y., Fadil, A., Henry, L., Theillere, Y., Ponchon, T., & Cathignol, D. 1993, "Characterization of extracorporeal ablation of normal and tumor-bearing liver tissue by high intensity focused ultrasound", *Ultrasound in Medicine and Biology*, vol. 19, no. 9, pp. 803-813.

109. Sokka, S. D. 2003, *Cavitation Methods in Therapeutic Ultrasound: Techniques, Mechanisms, and System Design,* PhD Dissertation, Massachusetts Institute of Technology.

110. Sokka, S. D. & Hynynen, K. H. 2000, "The feasibility of MRI-guided whole prostate ablation with a linear aperiodic intracavitary ultrasound phased array [In Process Citation]", *Phys Med Biol 2000.Nov.;45.(11.):3373.-83.*, vol. 45, no. 11, pp. 3373-3383.

111. Stepanow, B., Huber, P., Brix, G., Debus, J., Bader, R., van Kaick, G., & Lorenz, W. J. 1995, "Fast MRI temperature monitoring: Application in focused ultrasound therapy of malignant tissue in vivo.", *Proc.SMR 3rd Meeting, ISSN 1065-9889* p. 1172.

112. Sun, J. & Hynynen, K. 1998, "Focusing of therapeutic ultrasound through a human skull: a numerical study", *Journal of Acoustic Society of America*, vol. 104, no. 3 Pt 1, pp. 1705-1715.

113. Szent-Gorgyi, A. 1933, "Chemical and biological effects of ultrasonic radiation", *Nature*, vol. 131, p. 278.

114. ter Haar, G. R., Rivens, I., Chen, L., & Riddler, S. 1991, "High intensity focused ultrasound for the treatment of rat tumors", *Physics in Medicine and Biology*, vol. 36, pp. 1495-1501.

115. ter Haar, G. R., Rivens, I., Moskovic, E., Huddart, R., & Visioli, A. G. 1998, "Phase 1 clinical trials of the use of focused ultrasound surgery for the treatment of soft tissue tumours", *SPIE Photonics West 1998.*

116. Unger, E. C., McCreery, T. P., & Sweitzer, R. H. 1997, "Ultrasound enhances gene expression of liposomal transfection", *Investigate Radiology*, vol. 32, no. 12, pp. 723-727.

117. Unger, E. C., McCreery, T. P., Sweitzer, R. H., Caldwell, V. E., & Wu, Y. 1998, "Acoustically active lipospheres containing paclitaxel: a new therapeutic ultrasound contrast agent", *Investigate Radiology*, vol. 33, no. 12, pp. 886-892.

118. Vaezy, S., Fujimoto, V. Y., Walker, C., Martin, R. W., Chi, E. Y., & Crum, L. A. 2000, "Treatment of uterine fibroid tumors in a nude mouse model using high-intensity focused ultrasound", *Am.J.Obstet.Gynecol.*, vol. 183, no. 1, pp. 6-11.

119. Vallancien, G., Harouni, M., Guillonneau, B., Veillon, B., & Bougaran, J. 1996, "Ablation of superficial bladder tumors with focused extracorporeal pyrotherapy", *Urology*, vol. 47, no. 2, pp. 204-207.

120. Vallancien, G., Harouni, M., Veillon, B., Mombet, A., Prapotnich, D., Bisset, J. M., & Bougaran, J. 1992, "Focused extracorporeal pyrotherapy: Feasibility study in man", *Journal of Endourology*, vol. 6, pp. 173-180.

121. Viguier, J. L., Dessouki, T., Castelo, A., Martin, X., Marechal, J. M., Gelet, A., & Dubernard, J. M. 1993, "Benign prostatic hypertrophy treatment by transurethral radiofrequency hyperthermia with Thermex II", *European Urology*, vol. 23, no. 2, pp. 318-321.

122. Vykhodtseva, N. I., Hynynen, K., & Damianou, C. 1994, "The effect of pulse duration and peak intensity during focused ultrasound surgery: A theoretical and experimental study in rabbit brain in vivo", *Ultrasound in Medicine and Biology*, vol. 20, pp. 987-1000.

123. Watanabe, Y., Sato, M., Abe, Y., Horiuchi, S., Kito, K., Kimura, K., & Kimura, S. 1995, "Laparoscopic microwave coagulo-necrotic therapy for hepatocellular carcinoma: a feasible study of an alternative option for poor-risk patients", *J.Laparoendosc.Surg.*, vol. 5, no. 3, pp. 169-175.

124. Watkin, N. A., Morris, S. B., Rivens I H, Woodhouse, C. R., & ter Haar, G. R. 1996, "A feasibility study for the non-invasive treatment of superficial bladder tumours with focused ultrasound", *Brit.J.Urol.*, vol. 78, no. 5, pp. 715-721.

125. Wood, R. W. & Loomis, A. L. 1927, "The physical and biological effects of high frequency sound waves of greater intensity", *The London, Edinburgh, and Dublin Philosophical Magazine and Journal of Science*, vol. 4, pp. 417-436.

126. Yang, R., Reilly, C. R., Rescorla, F. J., Sanghvi, N. T., Fry, F. J., Franklin, T. D., & Grosfeld, J. L. 1992, "Effects of high-intensity focused ultrasound in the treatment of experimental neuroblastoma", *J Pediatr Surg*, vol. 27, pp. 246-251.

127. Yang, R., Reilly, C. R., Rescorla, F. J., Faught, P. R., Sanghvi, N. T., Fry, F. J., Franklin, T. D., Lumeng, L., & Grosfeld, J. L. 1991, "High-intensity focused ultrasound in the treatment of experimnetal liver cancer.", *Arch.Surg.*, vol. 126, pp. 1002-1010.

128. Yang, R., Sanghvi, N. T., Rescorla, F. J., Kopecky, K. K., & Grosfeld, J. L. 1993, "Liver cancer ablation with extracorporeal high-intensity focused ultrasound", *European Urology*, vol. 23 (Suppl. 1), pp. 15-22.

129. Zimmer, J. E., Hynynen, K., He, D. S., & Marcus, F. I. 1995, "The feasibility of using ultrasound for cardiac ablation", *IEEE Transactions of Biomedical Engineering*, vol. 42, no. 9, pp. 891-897.